Interferometric Precision Measurement with Macroscopic Silicon Optomechanics

Thesis by
Aaron Gregory Markowitz

In Partial Fulfillment of the Requirements for the
Degree of
Ph.D. in Physics

CALIFORNIA INSTITUTE OF TECHNOLOGY
Pasadena, California

2024
Defended December 8, 2023

Aaron Gregory Markowitz
ORCID: [0000-0003-0223-2342]

ACKNOWLEDGEMENTS

In light of the ongoing automation of information processing, I am all the more grateful to those who taught me how to temporarily care for our collective knowledge, and perhaps contribute to our ability to reason and create.

I thank my family for nurturing my curiosity. Thanks to my mom, Tracy Rhinehart; my dad, Randy Markowitz; my sister, Leah Markowitz; my stepparents Jill Markowitz and Bill Valentino; my aunts and uncles Scott Bruder, Lisa Bruder, Sheryl Markowitz, Bob Labes, Cindy Lanterman, Frank Lanterman, Ron Laino, Rich Rhinehart, Stephanie Rhinehart; my grandparents, Audrey Rhinehart, Richard Rhinehart, Martin Markowitz, and Norma Markowitz; and my cousins Jordan Cohen, Arielle Cohen, Hannah Leflein, Emma Bruder, Seth Laino, Eva Rothermel, Jared Laino, Anna Duda, Sarah Rhinehart, and Emma Rhinehart.

I am grateful to Prof. Horst von Recum for letting me do chemistry in his lab, where I learned the value of performing the right experiment. I also thank the many grad students and postdocs who took a teenager under their wings during those summers, including Steven Vesole, Jeffrey Halperin, Julius Korley, and Edgardo River-Delgado.

Prof. John Kovac introduced me to physics experiments, including some techniques like lock-in amplification that would shape my aesthetic preferences. In the CMB lab, Kirit Karkare, Chin Lin Wong, and Robert Kimberk taught me how to enjoy making measurements.

Prof. Vasant Natarajan taught me how light can be simultaneously a sturdy tool and a delicate timepiece. I fondly recall conversations spanning physics and philosophy with him and Apurba Paul, Dipankar Kaundilya, Lal Muanzuala, Pushpander Kumar Singh, and Ketan Rathod, among others.

Prof. John Doyle's encyclopedic knowledge of the dirty details behind experiments, from gaskets to transistors, inspired me to build my own apparatuses especially when I want to understand them well. Thanks especially to Elizabeth Petrik West for mentoring me during my research.

I suspect my figures do not meet Prof. Wesley Smith's standards, but the reader can share my gratitude to him for much of any clarity they offer. Thanks to Isobel Ojalvo, Laura Dodd, and Tyler Ruggles for teaching me some particle physics and how to use a computer.

Prof. Gary Feldman showed me how to make statistically rigorous statements, perhaps more than anything the art that defines science. Thanks to Gareth Kafka for connecting the decisions just before grad school to those at the end.

For the last several years, I had the privilege of Prof. Rana Adhikari trying to teach me everything: the importance of Q and control systems and noise budgets; how to work fast and when to work slow; who to trust with your experiment; that everything is quantum; how to lock the cavity. Thank you for your insight, humor, and guidance.

I cannot say enough about the extraordinary scientists I've collaborated with during grad school. Thanks to Brittany Kamai for friendship, mentoring on mentorship, and many writing sessions in coffee shops and in nature; to Chris Wipf for sounding nearly every project I undertook and reviving my much abused cymac; to Koji Arai for telling me how he aligns the OMC, among other lessons; to Gabriele Vajente for helping me adapt his experiment and analyses to a cryostat, and for his careful measurements; to Eric Gustafson, who taught me how a laser works; to Johannes Eiccholz for thorough problem solving in the lab, especially Wednesday evenings; to Andrew Wade for learning Finesse with me; to Yuntao Bai for reminding us about Mach-Zehnder interferometers; to Aidan Brooks for many a coffee, donut, and chat; to Jamie Rollins for Debian tips; to Mayank Chaturdevi for vibing in the lab with me perfectly, and at a critical moment; to Steve Vass for the regular snow reports; to Jancarlo Sanchez for keeping the table floating; and to Francisco (Paco) Salces-Carcoba for entertaining the fringe ideas.

So much of the functioning of a lab survives by transfer between peers. Thanks to Sarah Gossan for inviting me to her third space during my first year; to Zach Korth for showing me how to use the moderinger, probably the first control loop I tried to understand as such; to Evan Hall for answering the questions that taught me how LIGO works, and for careful estimates; to Kevin Kuns for answering the questions that taught me how optomechanics works, and for endless open source support; to Gautam Venugopalan for showing me around the 40m; to Craig Cahillane for his excellent Fabry-Perot cavity widget on github; to Ching Pin for hacking together several of our best cryo Q measurements; to Shruti Maliakal, who shared in designing and building a beautiful experiment; to Anchal Gupta for setting our deadline and being a true friend; to Ian MacMillan for letting me distract him from the opposite cubicle; to Radhika Bhatt for sharing the drive to APS and asking good questions; and to Xiaoyue Ni for showing me the KNI and helping me take some incredible

photos.

I am grateful to Prof. Yanbei Chen for his cheerful disposition and serious consideration of even my naive ideas. My interest in ponderomotive interferometry was sparked by a workshop attended by Yanbei, Tom Corbitt, Nancy Aggarwal, Haixing Miao, Belinda Pang, and Denis Martynov, and I am grateful for their invaluable lessons during that short week. I also am grateful to James Gardner for giving me a Hamiltonian and for developing our practice of Social Interactions; to Su Direcki for illuminating conversation on entanglement; to Xiang Li for helping me sketch useful features of interferometers; and Bassam Helou for many illuminating conversations and holding the rope.

Thanks to Adrienne Meier for countless conversations. Thanks to Larry Wallace, Mike Pedraza, and Michael Park for years of tech support and, along with Di-No Repairs, for setting up a loaner laptop when mine died a month before my defense.

I'm grateful to have lived in community with many roommates and close friends over the years, many of whom were like siblings. Thanks to Brianna Beswick, Li Kewei, Kyle Franseen, Joey Slipka, Ryan Chow, Steve Barroquiero, Nini Ren, Andrew Sun, Grace Kim, Samantha Heinle, Sarah Sohn, Cyndia Yu, Ross Rheingans-Yoo, Lucian Wang, Jude Russo, Mark Arildsen, Karina Perez, Josh Douglas, Vinicius Ferreira, Giuliana Viglione, Sho Harvey, and all of E41.

Finally, I must thank my comrades. Together, we advanced the organizational capacity of Pasadena's working class by enacting, through direct democracy, a state-leading municipal charter amendment including rent control, just cause eviction requirements, tenants' right to organize, and a permanent tenant-majority administrative board. We also made a home. Thanks to Arian Jadbabaie, Brigitte Rooney, Nathan Sagman, Ashay Patel, Jane Panangaden, Jae Fromm, Dustin Lagoy, Charles Xu, Shima Taj Bakhsh, Tarquin, John Brown, Sandwich, Artemis, Pinky, Mordechai, and Sassafras. Thanks especially to my incredibly patient partner Bobbi Ennis.

ABSTRACT

Optomechanical sensors provide our most sensitive measurements of spacetime, including observations of gravitational waves by laser interferometric detectors. However, even state of the art detectors like the Advanced Laser Interferometric Gravitational-Wave Observatory (LIGO) are still tens of orders of magnitude away from the measurement limits imposed by Heisenberg uncertainty. This thesis maps out the contours of mechanical and optical losses limiting next generation gravitational wave interferometers, and describes several experiments and analyses to improve those limitations. We review the theory of optomechanical force sensing to understand the influence of optical radiation pressure on the dynamics of mechanical oscillators. We analyze several modified Mach-Zehnder interferometers and show how radiation pressure can be a resource for quantum measurement, including by establishing a surprising optical spring effect in a cavity held on-resonance. The most developed proposal is for a phase-sensitive optomechanical amplifier to avoid the photodetection losses that may limit next-generation gravitational wave interferometers utilizing cryogenic silicon mirrors and $\approx$ 2000 nm infrared lasers. The amplifier calls for high quality mechanical oscillators made of single crystal silicon, which we fabricate. We describe our efforts to develop a testbed for cryogenic mechanical loss measurements of silicon oscillators and thin film coatings. And, we show how Bayesian inference can be used to improve our understanding of the physical mechanisms limiting a system's mechanical loss. Finally, we describe the optical, mechanical, and electronic design of a prototype phase sensitive optomechanical amplifier. The prototype is useful for testing the control system required to implement the full amplifier, and we characterize the current control scheme and the scheme for near-term upgrades. Our latest measurements show a clear path to steadily improving the amplifier's noise figure with well understood technology.

Updates to this work will be publicly available at LIGO document number P2300422 and at https://git.ligo.org/aaron.markowitz/writing along with source code and more.

PUBLISHED CONTENT AND CONTRIBUTIONS

[1]R. X. Adhikari et al., "A cryogenic silicon interferometer for gravitational-wave detection", Classical and Quantum Gravity **37**, 165003 (2020) 10.1088/1361-6382/ab9143, https://dx.doi.org/10.1088/1361-6382/ab9143,
AM developed the heat budget for the test masses, modeled the radiative cooldown process, and contributed to cryogenic design.

[2]Y. Bai et al., "Phase-sensitive optomechanical amplifier for quantum noise reduction in laser interferometers", Physical Review A **102**, 023507 (2020) 10.1103/PhysRevA.102.023507, https://link.aps.org/doi/10.1103/PhysRevA.102.023507,
AM contributed to conceptual development and made numerical models to validate our analytic results.

[3]M. Constancio Jr. et al., "Silicon emissivity as a function of temperature", International Journal of Heat and Mass Transfer **157**, 119863 (2020) 10.1016/j.ijheatmasstransfer.2020.119863, https://www.sciencedirect.com/science/article/pii/S0017931019361289,
AM performed the LIGO test masses cooldown calculations, participated in discussions during experimental design, and checked the experimental data analysis.

[4]L. G. Prokhorov et al., "Measurement of mechanical losses in the carbon nanotube black coating of silicon wafers", Classical and Quantum Gravity **37**, 015004 (2019) 10.1088/1361-6382/ab5357, https://dx.doi.org/10.1088/1361-6382/ab5357,
AM performed finite element analysis and contributed to discussion of how to deal with uncertainty in coating Young's modulus.

TABLE OF CONTENTS

LIST OF ILLUSTRATIONS

LIST OF TABLES

Chapter 1

INTRODUCTION

1.1 What We Measure

Measurement is the process by which physicists test the ability of a physical model to predict the behavior of the universe, or at least the system or laboratory under study. We typically want to reduce our uncertainty about a model parameter or reject a hypothesis using as few resources (time, energy, money) as possible.

Optomechanical measurement uses photons to measure the distance between atoms, and sometimes the rate of change of that distance. Optomechanics advances our understanding of physics across disparate length scales.

At large scales, the direct detection of gravitational waves [1] confirmed one of the major experimental predictions of Einstein's General Theory of Relativity [2]. The next generation of gravitational wave (GW) detectors [3] aims to deepen our understanding of GW signals from compact binary systems, as well as expand our access to the remaining GW spectrum at low and high frequency [4] [5].

At small scales, measurements to date imply that all physical systems behave quantum mechanically [6] [7]. One burning question of modern physics is how the apparently locally real behavior of gravitationally dominated systems arises in a fundamentally quantum universe. Increasingly, increasingly macroscopic optomechanical experiments aim to probe the boundary between our quantum and classical descriptions [8] [9].

1.2 Limits to Measurement

Q and Quantum

Braginsky *et al.* describe why linear oscillators with small dissipation make excellent force sensors [10] [11]. They consider an oscillator with mass M, frequency ω, and quality factor Q. Treated classically, the noise limiting the measurement of oscillator amplitude due to a force acting at ω for duration $\hat{\tau}$ is a thermally induced amplitude change that decreases with oscillator quality factor Q.

$$\Delta x_T \approx \sqrt{\frac{kT\hat{\tau}}{M\omega Q}} \tag{1.1}$$

With sufficiently high Q, the thermal noise of an oscillator in a coherent state may be reduced below the size of the oscillator's wavepacket [12].

Gravitational Wave Interferometers

The quantum limits of measurements made with oscillators in coherent states are now being reached and exceeded by gravitational wave interferometers [13]. For traditional interferometry, our null measurement is of a particular photon vacuum state, and we devise our system such that classical information can be continuously imparted on the null state. We can improve our measurements by choosing a more optimal null state, and by protecting the null state from optical and mechanical losses along the entire measurement chain. The possibility of reducing quantum noise by an appropriate choice of observables or even with quantum error correction [14] demonstrates that gravitational wave interferometers are still fundamentally limited by Q rather than quantum mechanics.

To reduce the noise in gravitational wave detectors [15], it is beneficial to have many photons all in the same state, as in a high power laser stabilized against some conveniently chosen quantum state; and to measure the average position of many atoms that are not moving much, as in heavy mirrors of high quality. The inverse relationship between quantum noise spectral density S_{PP} and measurement sensitivity S_{FQL} is capture in the so-called fundamental or energetic quantum limit, also known as the quantum Cramer-Rao bound, which can be formulated for laser interferometric GW detectors as [16]

$$S^{h}_{\mathrm{FQL}}(\Omega) = \frac{\hbar^2 c^2}{S_{PP}(\Omega) L^2} = \frac{4\hbar^2}{S_{\mathcal{E}\mathcal{E}}(\Omega)}. \tag{1.2}$$

Stated simply, precise measurements of spacetime require tight control of a system in the face of large energy fluctuations $S_{\mathcal{E}\mathcal{E}}$. A more thorough exploration of measurement precision limits in the language of control theory is provided in [17]. Braginsky, Mitrofanov, and Panov [10] formulated this limit as a maximum observable quality factor due to the effect of the measurement process.

1.3 Contributions

This work is divided into three parts covering the theory of optomechanical interferometry in Part I; experimental and analytical techniques in silicon optomechanics in Part II; and an early stage tabletop interferometry experiment, motivated and enabled by the previous parts, in Part III. The appendices discuss some measure-

ment techniques and topics of interest that were only briefly explored, but may be of use to someone beginning a deeper study. I apologize for the many pedagogical deficiencies, and encourage the reader attempting to apply or replicate this work to request clarification if required.

Chapter 2, on ponderomotive interferometry, is largely a review. If I have a novel contribution, it is the explicit expression for the input-output relation of a mechanically responsive beamsplitter pumped by counterpropagating lasers incident on the same side of the optic (which surely others have derived but not seen fit to publish, to my knowledge).

The work in Chapter 3 is a summary of our group's proposal for a new quantum measurement widget, the phase-sensitive optomechanical amplifier (PSOMA) [18]. I contributed to conceptual development and performed numerical simulations and optimization in Optickle and Finesse to validate our analytic results.

I developed a strong interest in generalizing PSOMA, and describe the outcome in Chapter 4. I propose and simulate signal- and power-recycled Mach-Zehnder interferometers operated in transmission and/or reflection, as an internal quantum filter-squeezer for Michelson-based gravitational wave interferometers, or as independent resonant strain sensors. To my knowledge this is the first discussion in the literature of dual recycled Mach-Zehnder interferometers and the utility of the interferometer's microscopic position *within* the otherwise fixed recycling cavities. I have not exhaustively explored this device, but attempt to connect it to existing work in quantum coherent interferometry and optomechanical trapping and cooling such that natural extensions become apparent. I am grateful to many colleagues for letting me distract them with this idea and helping me understand the system, including Shruti Maliakal, Kevin Kuns, Xiang Li, James Gardner, Chris Wipf, Yanbei Chen, and Rana Adhikari.

The central technologies enabling quantum coherent laser interferometry in the lab are high stability light and high quality mechanics, and as much of it as desired. The experimenter should clamp down their mechanics before turning on the laser, so Chapter 5 describes my experimental work fabricating cm- and gram-scale Si mechanical oscillators for use as optomechanics. I implemented but did not invent the fabrication techniques therein. I also carried out some small experiments, including with Disha Kapasi on surface roughness following KOH etching, to advance our group's understanding and application.

I used my Si mechanical oscillators in the cryogenic thin film mechanical loss testbed described in Chapter 6. I was the primary student who, along with postdoc Brittany Kamai, designed, operated, and analyzed the testbed and our results. We applied the prior art of gentle nodal suspension to a liquid nitrogen cryostat, demonstrating experimental limitations of some cryogenic design choices for this mechanical isolation technique. I also used Nic Smith's clever method for constant-amplitude quality factor measurement [19] to explore a new technique for non-contact temperature sensing and control of a mechanical oscillator.

Our cryogenic mechanical loss testbed inspired Anna Roche, Rana Adhikari, and me to develop a novel analysis for material parameter estimation we call loss tomography, described in Chapter 7. Loss tomography contributes to the field of high Q mechanical loss measurement and material development by eliminating systematic errors associated with sequential mechanical Q measurement before and after test film deposition. I made the FEA models used for the analysis, and developed the loss budget with Brittany Kamai. I independently completed the quick-and-dirty demonstration at the end of the chapter.

In the future, we anticipate utilizing Si mechanical oscillators in our tabletop PSOMA demonstration. Chapter 8 covers the detailed design of the early stage experiment, and our targeted late-stage performance. Shruti Maliakal, Rana Adhikari, and Chris Wipf contributed to all aspects of the design. I commissioned a new vacuum system, which I designed with Stephen Appert. I used Shruti's Finesse-based mode matching optimization code to choose an appropriate cavity geometry for the optics on hand. I constructed and characterized the fiber and free-space optical layout, with sanity-preserving assistance at various times from Shruti Maliakal, Mayank Chaturvedi, Yuta Michimura, Francisco (Paco) Salces Carcoba, Chris Whittle, Jeff Wack, and Jancarlo Sanchez.

Mayank Chaturvedi, Shruti Maliakal, Chris Wipf, Rana Adhikari, and I developed the control system characterized in Chapter 9, which has some novelty even if mostly due to the inherent specificity of control systems. Our signal injection strategy is reminiscent though not identical to the coherent locking technique used in GW and related interferometers to implement frequency-dependent optical squeezing. We also develop a new application of multiple phase-locked loops to measure the full 2-quadrature transfer function of a Pound-Drever-Hall locked cavity. I briefly discuss my proposal for using a Mach-Zehnder interferometer to reduce pump phase noise coupling in this scheme.

Finally, Chapter 10 presents a characterization and noise budget of the PSOMA demonstration in its current form. Shruti Maliakal and I developed the noise budget. I contributed the most sensitive measurement to date of the low frequency phase noise of TeraXion's PureSpectrum laser module. Mayank Chaturvedi, Chris Whittle, and Jeff Wack were invaluable collaborators on several of the transfer function measurements presented in this chapter.

Part I

Ponderomotive Interferometry

Some new ways to use radiation pressure

Chapter 2

OPTOMECHANICAL SENSING

The purpose of this chapter is to define the mathematical framework employed throughout the rest of the work. For the most part, we follow the approach of [20]. Other good reviews of cavity optomechanics include [21].

2.1 Optical Sensing

The basic componenents of optomechanical systems are lasers, beam blocks or photodetectors, free space propagation, and beamsplitters. Nonlinear media with complicated dispersion relations can be used to produce various types of correlators, but we will mostly not consider those in this work.

Lasers, Vacuum, and Strain

The operator of the quantized electric field is [9]

$$\hat{E} = u(x,y,z)\int_0^{+\infty}\frac{d\omega}{2\pi}\sqrt{\frac{2\pi\hbar\omega}{\mathcal{A}c}}[\hat{a}_\omega e^{ikz-i\omega t}+\hat{a}_\omega^\dagger e^{i\omega t-ikz}]. \tag{2.1}$$

We typically work within the two-photon formalism of Caves and Schumaker [22] [23], which in the frame rotating at ω_0 (typically some laser's carrier frequency) substitutes pairs of operators that create or annihilate photons at $\omega_0\pm\Omega$ for quadrature operators that describe the amplitude and phase of the carrier field at frequency Ω.

$$\hat{a} \equiv \begin{pmatrix}\hat{a}_c\\ \hat{a}_s\end{pmatrix} \tag{2.2}$$

Following the framework of Corbitt, Chen, and Mavalvala [20], an optomechanical system consists of a set of elementary subsystems represented by $N\times N$ matrices $\mathcal{M}_{N,N}$ relating N incident quadrature fields to N outgoing quadrature fields. Each element of $\mathcal{M}_{N,N}$ is itself a 2×2 matrix describing how the two quadrature fields transform between the corresponding nodes in the system. The input nodes $u^{(i)}$ generically consist of contributions from vacuum fluctuations $v^{(i)}$, the laser $I^{(i)}$, and spacetime strain modulation $H^{(i)}h$.

$$\hat{u}^{(i)} = \hat{v}^{(i)} + \hat{I}^{(i)} + \hat{H}^{(i)} h \tag{2.3}$$

A beam block or photodiode is an element whose input-output relation has only the vacuum term, with no laser or strain coupled in. Classical (unsqueezed) vacuum sources have uncorrelated white noise with unit amplitude spectral density and zero mean in both directions, while squeezed or other nonclassical vacuum states conserve total noise power but can otherwise distribute the noise arbitrarily between the two quadratures.

A laser may couple in a bright field at $\Omega = 0$ Hz, sideband fields at $\Omega \neq 0$, and classical noises associated with the laser, in addition to a possibly squeezed vacuum field. A carrier field with intensity I_j and phase θ_j is represented by

$$\hat{D}_j \equiv \sqrt{2I_j} \begin{pmatrix} \cos\theta_j \\ \sin\theta_j \end{pmatrix}. \tag{2.4}$$

The contribution of spacetime strain is typically small enough to ignore except between nodes separated by a large propagation length containing a high power carrier field. Classical gravitational radiation's modification to a locally Minkovski metric $\eta_{\mu\nu}$, first described in a gauge-invariant form by Pirani [24], can be expressed in the transverse-traceless gauge as

$$\begin{aligned} g_{\mu\nu} &= \eta_{\mu\nu} + h_{\mu\nu} \\ h_{\mu\nu} &= \cos(\Omega t - kz) \begin{pmatrix} 0 & 0 & 0 & 0 \\ 0 & h_+ & h_\times & 0 \\ 0 & h_\times & h_+ & 0 \\ 0 & 0 & 0 & 0 \end{pmatrix} \end{aligned} \tag{2.5}$$

where h_+ and $h_\times$ are field amplitudes of the two radiation polarizations traveling at frequency Ω along $\hat{z}$. Eq 2.5 can be rotated to find the strain due to gravitational radiation in an arbitrary direction with wavevector $k(k_x\hat{x} + k_y\hat{y} + k_z\hat{z})$, which following [25] modifies the total phase $\Phi(t_0)$ accumulated by light traveling length L along $\hat{x}$ to

$$\Phi^x(t_0) = \frac{\omega}{c} \int_0^L \sqrt{1 + h_{xx} \cos(\Omega t_0 + k(1 - k_x)x)}\, dx. \tag{2.6}$$

We can see that both the strain amplitude and effective wave vector along the propagation length depend on the orientation of the GW to the light. We can get an intuitive expression relevant to the optomechanical sensor by assuming an infinitesimal propagation length dL such that the strain is uniform across the propagation length, and call h the Fourier transform of the GW amplitude projected along h_{xx}. If the propagation length contains a carrier field $\hat{D}$ at ω, the strain contribution to 2.3 is given by [20]

$$\hat{H} \equiv \sqrt{\frac{\omega}{4c^2\hbar}}\hat{D}^* dL. \tag{2.7}$$

The character * refers to quadrature rotation by $\pi/2$, for example

$$\begin{pmatrix} v_1 \\ v_2 \end{pmatrix}^* = \begin{pmatrix} v_2 \\ -v_1 \end{pmatrix}. \tag{2.8}$$

In the expression for strain coupling, * indicates the pump laser acquires phase fluctuations proportional to its field amplitude.

Free Space Propagation

Perhaps the most remarkable and useful behavior of photons is that their phase evolution keeps track of their proper distance travelled. The matrix for the free space propagator is [20]

$$M_{\text{prop}} \equiv e^{i\phi}\begin{pmatrix} 0 & R_\Theta \\ R_\Theta & 0 \end{pmatrix} \tag{2.9}$$

where M_{prop} relates $\begin{pmatrix} \hat{a}_1 \\ \hat{a}_2 \end{pmatrix}$ to $\begin{pmatrix} \hat{b}_1 \\ \hat{b}_2 \end{pmatrix}$ as described in 2.1 and

$$\Theta \equiv \frac{\omega_0 L}{c}, \phi \equiv \frac{\Omega L}{c}, R_\Theta \equiv \begin{pmatrix} \cos\Theta & -\sin\Theta \\ \sin\Theta & \cos\Theta \end{pmatrix}. \tag{2.10}$$

Beamsplitters

Beamsplitters are the basic units that perform linear operations on propagating electric fields. Beamsplitters have four input and four output ports, which we label in 2.1. Neglecting briefly the dynamics of the beamsplitter itself, a beamsplitter with reflectivity ρ, transmissivity τ, and optical loss $\eta^2 \equiv 1 - \rho^2 - \tau^2$ transforms input fields as Eq 2.11.

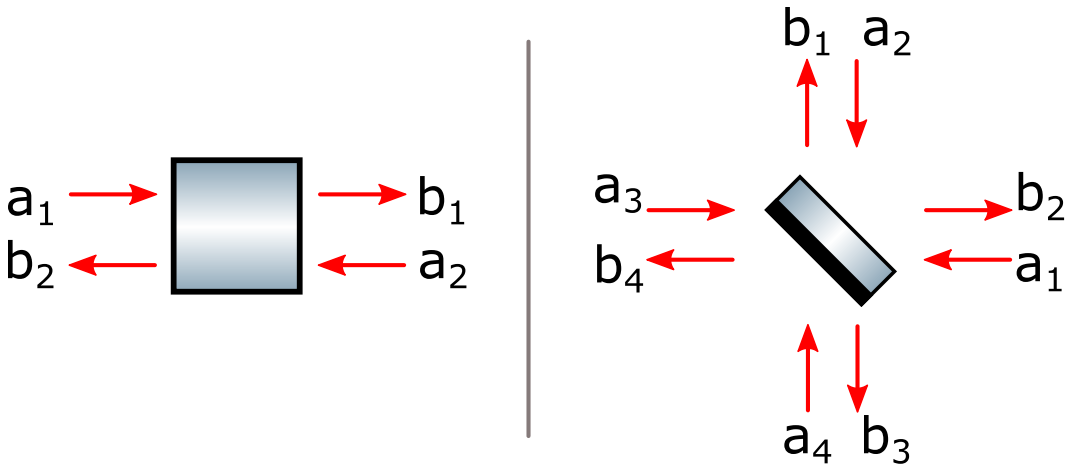

Figure 2.1: Port labelling for basic optomechanical elements. Right: Beamsplitter labelled with four input and four output ports. Left: Port labels for free space propagation.

$$\begin{pmatrix} \hat{b}_1 \\ \hat{b}_2 \\ \hat{b}_3 \\ \hat{b}_4 \end{pmatrix} = M_{\mathrm{BS}} \begin{pmatrix} \hat{a}_1 \\ \hat{a}_2 \\ \hat{a}_3 \\ \hat{a}_4 \end{pmatrix} - \eta \begin{pmatrix} \hat{v}^{(1)} \\ \hat{v}^{(2)} \\ \hat{v}^{(3)} \\ \hat{v}^{(4)} \end{pmatrix} \tag{2.11}$$

We can adapt the expression of [20] to write

$$M_{\mathrm{BS}} \equiv \begin{pmatrix} -\rho & 0 & 0 & \tau \\ 0 & -\rho & \tau & 0 \\ 0 & \tau & \rho & 0 \\ \tau & 0 & 0 & \rho \end{pmatrix}. \tag{2.12}$$

"Mirrors" are simply beamsplitters operated at normal incidence, such that we can identify $\hat{a}_1 \leftrightarrow \hat{a}_2$, $\hat{b}_1 \leftrightarrow \hat{b}_2$, $\hat{a}_3 \leftrightarrow \hat{a}_4$, $\hat{b}_3 \leftrightarrow \hat{b}_4$.

Cavities

Cavities are a collection of $N \geq 2$ beamsplitters (or other 4-port optical elements) arranged such that for some choice of labels,

- on one side of beamsplitter 1, at least one of the incident beams arrives from beamsplitter N and is reflected to beamsplitter 2,
- for $n > 1$, at least one beam incident on beamsplitter n comes from beamsplitter $n-1$.

Optical cavities are used in many sensing problems, including gyroscopes [26] and gravitational wave detection.

The cavity's free spectral range (FSR) is the separation (in frequency units) of the cavity resonances. For a cavity in free space, it is set by the round trip cavity length alone:

$$\Delta\nu_{FSR} = \frac{c}{L_{\text{roundtrip}}}. \tag{2.13}$$

Radiation Pressure

In the two-quadrature picture, the momentum flow carried by an optical field with power I_j at node j is

$$\dot{P}_j(\Omega) = \sqrt{\frac{\hbar\omega}{c}}\hat{D}_j^T\hat{j}(\Omega) \tag{2.14}$$

where $\hat{j}(\Omega)$ is the sideband component at Ω.

Here again we have relabelled expressions in [20], which can be used to derive the input-output relation for the beamsplitter of mass M with radiation pressure and optical losses.

$$\begin{aligned}
&[\mathbb{I} + \frac{\Pi}{2}\begin{pmatrix} D^*_{\hat{a}_1} \\ D^*_{\hat{a}_2} \\ D^*_{\hat{a}_3} \\ D^*_{\hat{a}_4} \end{pmatrix}\begin{pmatrix} D^T_{\hat{b}_1} & D^T_{\hat{b}_2} & -D^T_{\hat{b}_3} & -D^T_{\hat{b}_4} \end{pmatrix}]\begin{pmatrix} \hat{b}_1 \\ \hat{b}_2 \\ \hat{b}_3 \\ \hat{b}_4 \end{pmatrix} \\
&= [M_{\text{BS}} - \frac{\Pi}{2}\begin{pmatrix} D^*_{\hat{a}_1} \\ D^*_{\hat{a}_2} \\ D^*_{\hat{a}_3} \\ D^*_{\hat{a}_4} \end{pmatrix}\begin{pmatrix} D^T_{\hat{a}_1} & D^T_{\hat{a}_2} & -D^T_{\hat{a}_3} - D^T_{\hat{a}_4} \end{pmatrix}]\begin{pmatrix} \hat{a}_1 \\ \hat{a}_2 \\ \hat{a}_3 \\ \hat{a}_4 \end{pmatrix} - \eta\begin{pmatrix} \hat{v}^{(1)} \\ \hat{v}^{(2)} \\ \hat{v}^{(3)} \\ \hat{v}^{(4)} \end{pmatrix}
\end{aligned} \tag{2.15}$$

Roughly, the new terms account for additional phase accumulated by the incident fields due to the effect of radiation pressure of the incident and outgoing fields on the mirror position.

A beamsplitter operated at angle of incidence α with mechanical responsivity $\chi(\Omega)$ has

$$\Pi \equiv \frac{2\rho\omega}{c^2}\cos^2(\alpha)\chi(\Omega) \tag{2.16}$$

which for a beamsplitter that can be treated as a free mass M becomes

$$\Pi = \frac{2\rho\omega}{M\Omega^2 c^2}\cos^2(\alpha). \tag{2.17}$$

2.2 Optomechanical Systems with Radiation Pressure

The ponderomotive (radiation pressure) force leads to parametric instability in optomechanical systems [27], but also is a useful resource for sensing.

Optomechanical Cooling

Using optical fields to cool mechanical oscillators can significantly enhance the sensitivity of mechanical sensors, since the effective Q of optomechanical systems dominated by optical forces can be significantly enhanced relative to the Q of the bare mechanical oscillator.

Recent advances in quantum optics have enabled quantum-enhanced cooling of mechanical systems [28] [29] or cooling to the mechanical oscillator's ground state [30]. Even the remaining displacement noise of an optomechanically cooled oscillator can be suppressed with appropriate sensing [31].

2.3 Gravitational Wave Interferometers

Gravitational wave interferometers are sensitive force and displacement senesors used to detect gravitational waves and place limits on fundamental physics [32]. Interferometric gravitational wave observatories (GWIFO) like LIGO [33] are thoroughly discussed in the classic book by Saulson [34] and in [35] [36] [37] [38]. TGWIFO consist of freely falling test masses (TMs) of mass m, mechanically isolated by pendula such that Earth's (mostly dissipation-free) gravitational potential provides their dominant restoring force. Two pairs of TMs in LIGO-like GWIFOs form two orthogonally oriented Fabry-Perot (FP) cavities, which sense the phase accumulated by light propagating in each FP cavity. The relative phase noise of each FP is separated from common-mode laser noise by combining the FP outputs on a beamsplitter, forming a Fabry-Perot Michelson Interferometer (FPMI). And, normal-incidence recycling mirrors on each input port of the FPMI set the impedance matching condition of light entering or leaving the dual-recycled FPMI (DRFPMI).

Mechanics

When considering quantum measurement with a GWIFO, we must treat both the free test masses and laser field quantum mechanically. The relative position $\hat{x}$ and momentum $\hat{p}$ operators of the TMs obey equations of motion [9]:

$$\begin{aligned} \dot{\hat{x}}(t) &= \frac{\hat{p}}{m} \\ \dot{\hat{p}} &= \frac{\hat{I}}{c} + mL\ddot{h}(t). \end{aligned} \tag{2.18}$$

Some noises

The limiting noises of the current generation of GW interferometers are discussed in [39]. The most fundamental limiting noises are quantum noise due to quantization of the sensing light field (introduced as $\hat{v}$ in Eq 2.3), and thermal noise due to Brownian motion of various parts of the mechanical system (coatings, suspension, test mass substrates) [40].

Thermal noise can be attributed to loss in the mechanical susceptibility of the test mass to forces applied by the laser [41] [42].

The first complete treatment of quantum noise in second generation GW interferometers are the classic works by Buonnano and Chen [43] [44]. An excellent review on the topic is [45].

Chapter 3

PHASE-SENSITIVE OPTOMECHANICAL AMPLIFIER

Many figures and derivations in this chapter can be found in our proposal for a phase-sensitive optomechanical amplifier (PSOMA) to realize single quadrature optical preamplification in an entirely optomechanical system [18]. The proposed PSOMA can achieve sufficiently low noise, high gain, and high isolation to benefit next generation GW IFOs limited by optical readout losses.

3.1 Phase-Sensitive Amplification

The nonlinearity of optomechanical radiation pressure interactions can be utilized in many photonic signal processing applications [46].

The fundamental noises for optomechanical sensors like gravitational wave interferometers can be thermal and quantization noises of the mechanical or optical degrees of freedom [40]. One challenge for next generation gravitational wave interferometers will be quantum noise due to the low quantum efficiency of existing photodetection technologies at wavelengths beyond 1064 nm [47]. Photodetection optical losses are generally important for optical sensors utilizing highly squeezed optical states.

Caves [48] and more recently Knyazev *et al.* [49] [50] proposed overcoming photodetection losses by pre-amplifying the signal-carrying optical quadrature, such that unsqueezed vacuum fields introduced by downstream optical losses do not limit the sensor's input-referred noise performance. The general principles of quantum noise in linear amplifiers are described in [51].

3.2 Traveling Wave Cavity

PSOMA (the "Amplifier" in Figure 3.1) uses a traveling wave cavity to enhance the radiation pressure coupling between a pumping laser and a mechanical oscillator. The circulating power (and optomechanical gain) in the cavity is enhanced by the cavity finesse, with a tradeoff in the amplifier's bandwidth due to a finite cavity pole. Because the radiation pressure force falls off like $1/f^2$, ponderomotive amplification is most effective at low frequencies and we can choose an appropriate cavity finesse and length to optimize for high optomechanical gain over the measurement band.

We choose a traveling wave cavity, rather than a Fabry-Perot cavity, to ensure that the reverse propagating vacuum field from the photodetection port is not amplified on its way to the low noise measurement device. Only the optical field copropagating and in-phase with the pump drives the mechanical oscillator with nonnegligible coupling.

3.3 Mach-Zehnder Interferometery

With only a single traveling wave cavity, PSOMA's input referred noise can be limited by relative intensity noise (RIN) of the pump laser. Even if pump RIN is prestabilized to the quantum shot noise level, this noise would limit the utility of PSOMA for sub-SQL measurement devices. To mitigate the contribution from pump RIN, PSOMA uses an interferometric technique analogous to the long-tailed pair in electronic differential amplifiers [52].

The pump and probe (signal-carrying) beams enter PSOMA at the input beamsplitter of a Mach-Zehnder interferometer (MZI). Each arm of the MZI contains a nominally identical traveling wave cavity, and the cavity reflections are recombined at the MZI's output beamsplitter. Due to the π phase shift experienced on reflection from one side of the input beamsplitter, one cavity is driven by the sum of pump and probe fields, while the other is driven by the difference of pump and probe fields. With an appropriate choice of MZI detuning, the output BS of the MZI can separate the symmetric and antisymmetric contributions such that one MZI output port contains only the pump and amplified pump noise, while the other MZI output port contains only the probe and amplified probe signals.

In this way, the MZI is the 2-port version of the Michelson interferometer (MI). The ideal MI operated on the dark fringe perfectly reflects all fields incident on its antisymmetric (dark) port. The ideal MZI operated on the dark fringe perfectly transmits all fields incident on its antisymmetric ports.

With identical traveling wave cavities in each arm of the MZI, pump RIN is rejected out the common mode port of PSOMA. On the other hand, the optical field entering the probe port is differentially amplified by the cavities and exits out the differential (antisymmetric, probe, dark) port of PSOMA. This allows the SNR of signals much smaller than pump RIN to be preserved, up to limits imposed by the contrast defect of the MZI or gain imbalance of the arm cavities.

Mach-Zehnder interferometers are further described in [53] and elsewhere.

Input-Output Relations

The derivation of the input-output relations of PSOMA is in [18].

Let R_A, T_A denote the power reflectivity and transmissivity, respectively, of the M1L and M1R mirrors, and L_A denotes the round-trip length of each ring. In the limit of a high finesse cavity with low frequency signals compared to the cavity length, $\Omega L_A/c << 1$ and $T_A << 1$, giving

$$\begin{pmatrix} b_{out,1} \\ b_{out,2} \end{pmatrix} = e^{2i\eta} \begin{pmatrix} 1 & 0 \\ -\mathcal{K}_A & 1 \end{pmatrix} \begin{pmatrix} b_{in,1} \\ b_{in,2} \end{pmatrix} + \sqrt{\frac{32\omega_0 P_{\text{circ}}}{\hbar c^2}} \frac{1}{T_A} \begin{pmatrix} 0 \\ 1 \end{pmatrix} \xi \tag{3.1}$$

where

$$\begin{aligned} \mathcal{K}_A &= \frac{4}{T_A[1 + (\Omega/\gamma_A)^2]} \kappa_A \\ \kappa_A &= -\frac{18\omega_0 P_{\text{circ}}}{c^2} \chi_A \\ \eta &= \arctan(\Omega/\gamma_A) \\ \gamma_A &= \frac{cT_A}{2L_A} \end{aligned} \tag{3.2}$$

with γ_A the cavity pole frequency, P_{circ} the power circulating in each ring, χ_A the mechanical susceptibility of the movable mirrors, and c the speed of light. Noise may couple in to PSOMA through ξ, the motion of mirrors in the ring cavity not due to quantum radiation-pressure noise (for example seismic or thermal noise).

3.4 For LIGO Voyager

Sensitivity Improvement

In [18], we proposed using PSOMA to preamplify optical signals exiting a next-generation GW IFO before they encounter optically lossy elements like photodiodes. The proposed configuration is in Fig. 3.1.

The amplifier has a modest benefit in the observatory's most sensitive band between 40-300 Hz under assumptions consistent with current optics technology. However, the improvement is more significant for configurations using higher levels of squeezing. More than 15 dB of injected squeezing does not improve sensitivity under the assumption of high photodetection losses without preamplification, and some kind of low-loss preamplification like PSOMA becomes necessary to take advantage of

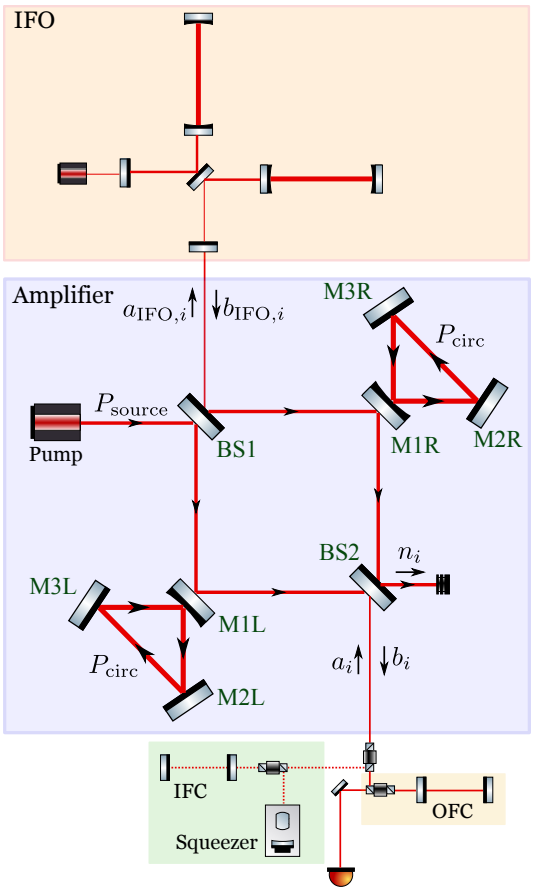

Figure 3.1: Optical configuration of PSOMA as applied to a LIGO-like gravitational wave interferometer.

higher levels of squeezing. We show the noise improvement for the most likely and optimistic parameter choices in Figures 3.3 and 3.4. The expected noise budget for the pragmatic configuration is in 3.2.

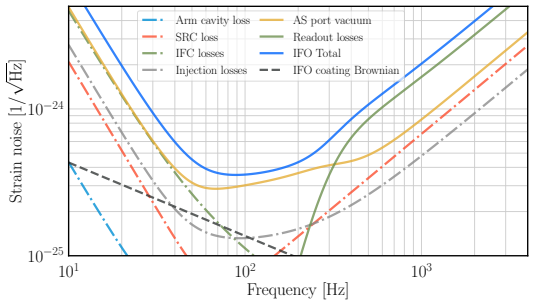

Figure 3.2: Noise budget for PSOMA applied to LIGO Voyager under a pragmatic choice of parameters and technical noises.

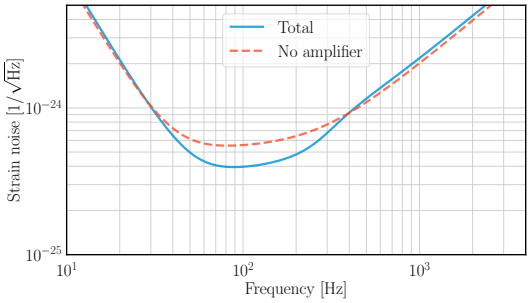

Figure 3.3: Strain noise referred sensitivity improvement for PSOMA applied to LIGO Voyager under a pragmatic choice of parameters and technical noises, including 15 dB of frequency dependent squeezing and 30 g amplifier mirrors.

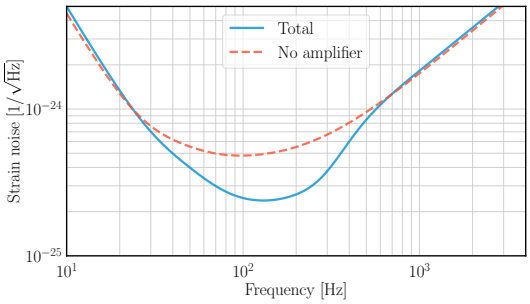

Figure 3.4: Strain noise referred sensitivity improvement for PSOMA applied to LIGO Voyager under an optimistic choice of parameters and technical noises, including 20 dB of frequency dependent squeezing and 10 g amplifier mirrors.

Amplifier Gain

The ponderomotive force, and therefore also PSOMA's gain, falls off like $1/f^2$. However, because the optimal homodyne readout quadrature varies with frequency, we do not always sense the maximally amplified quadrature. Therefore, the effective signal amplification also varies with frequency, as shown in Fig. 3.5.

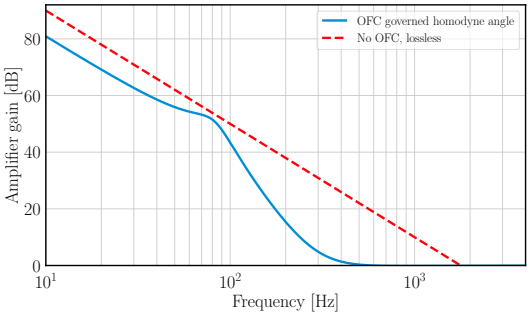

Figure 3.5: Amplifier gain with and without output filter cavity implementing frequency-dependent homodyne detection.

Chapter 4

QUANTUM COHERENT INTERFEROMETRY

Careful and fully phase-sensitive design can improve the performance of optomechanical sensors. This chapter explores how the additional interferometric degrees of freedom afforded by Mach-Zehnder interferometers can be used to benefit gravitational wave detection. We apply some ideas from advanced GWIFO design to generalize the device from Chapter 3, and explore some new ways the generalized traveling-wave optomechanical amplifiers can be used for quantum coherent interferometric sensing.

Advanced interferometers and optomechanical configurations for optimal quantum noise performance are discussed in [54] [55] [56] [57] [58]. PT symmetric interferometers are discussed in a series of papers including [59] [60].

Using quantum mechanical systems for measurement is intimitely related to the field of quantum computing and quantum information processing [14] [61] [62] [63] [64] [65] [66] [67] [68] [69] [70], where linear Gaussian optics are powerful tools for Gaussian quantum information processing [71].

4.1 Power- and Arm-Recycled Mach-Zehnder Interferometers (PARMZI)

Power recycling is well understood for Michelson interferometers, where for example GWIFOs introduce a normal-incidence mirror to the Michelson's bright port to enhance the buildup of optical power in the interferometer. In the Mach-Zehnder interferometer (MZI), power recycling requires normal incidence mirrors on each of the two "bright" ports of the MZI. As in Michelson interferometers, power recycling leads to resonant gain of the pump laser field, since we have essentially placed the MZI inside a resonant Fabry-Perot cavity (PRC). However, we have also introduced an additional degree of freedom characterizing the microscopic position of the MZI inside the PRC. From the perspective of the MZI input BS, the pump phase exiting the MZI can be chosen independent of the pump phase entering the MZI while holding the PRC on resonance.

The configuration for PARMZI is close to that in Figure 4.2, but without the normal-incidence signal (differential) port mirrors.

Input-Output Relations for the Light Mirror

The input-output relations of PARMZI are similar to PSOMA for the forward-propagating signal field, but modifying $P_{\mathrm{circ}} \rightarrow g_P P_{\mathrm{circ}}$ to account for optical gain g_P in the PRC. However, the reverse propagating pump allows reverse propagating probe fields to drive the cantilever, and all cantilever motion will generate sidebands on the reverse propagating pump field.

First, consider the input-output relations of just the movable mirrors, which are beamsplitters with near-zero transmissivity $\tau \rightarrow 0$ and mass m. Adapting Eq. 2.15 and Fig. 2.1, we can reduce to two pumping fields with power I_1, I_2 and phases θ_1, θ_2 incident at a_1 and a_2, respectively. It will turn out that even when solvable there is no clean analytic expression for the general input-output relations, so for clarity we will ignore optical loss and set $\rho = 0$. In some of the numerical analysis presented later, optical losses and finite mirror transmissivity will be included to demonstrate their limited effect on the conceptual results.

$$\begin{aligned}
&[\mathbb{I} - \frac{\Pi}{2}\begin{pmatrix} D^*_{\hat{a}_1} \\ D^*_{\hat{a}_2} \end{pmatrix}\begin{pmatrix} D^T_{\hat{a}_1} & D^T_{\hat{a}_2} \end{pmatrix}]\begin{pmatrix} \hat{b}_1 \\ \hat{b}_2 \end{pmatrix} \\
&= -[\mathbb{I} + \frac{\Pi}{2}\begin{pmatrix} D^*_{\hat{a}_1} \\ D^*_{\hat{a}_2} \end{pmatrix}\begin{pmatrix} D^T_{\hat{a}_1} & D^T_{\hat{a}_2} \end{pmatrix}]\begin{pmatrix} \hat{a}_1 \\ \hat{a}_2 \end{pmatrix}
\end{aligned} \tag{4.1}$$

To solve for the output fields, we need to invert the matrix on the left-hand side (LHS).

$$\Xi \equiv \mathbb{I} - \frac{\Pi}{2}\begin{pmatrix} D^*_{\hat{a}_1} \\ D^*_{\hat{a}_2} \end{pmatrix}\begin{pmatrix} D^T_{\hat{a}_1} & D^T_{\hat{a}_2} \end{pmatrix} \tag{4.2}$$

Ξ has four eigenvectors with eigenvalue 1. Note that unlike the case well studied in interferometric speedmeters which pump the beamsplitter from both sides of the HR surface [20], no additional optomechanical resonance arises in our case. One set of eigenvectors is

$$\{\xi_i\} = \{\begin{pmatrix} D^*_{\hat{a}_1} \\ 0 \end{pmatrix}, \begin{pmatrix} 0 \\ D^*_{\hat{a}_2} \end{pmatrix}, \begin{pmatrix} D_{\hat{a}_2} \\ -D_{\hat{a}_1} \end{pmatrix}\begin{pmatrix} D_{\hat{a}_1} \\ -D_{\hat{a}_2} \end{pmatrix}\}. \tag{4.3}$$

One can find

$$\Xi^{-1} = \mathbb{I} + \frac{\Pi}{2}\begin{pmatrix} D^*_{\hat{a}_1} \\ D^*_{\hat{a}_2} \end{pmatrix}\begin{pmatrix} D^T_{\hat{a}_1} & D^T_{\hat{a}_2} \end{pmatrix}. \tag{4.4}$$

Conveniently, this leads to a simple expression for the input-output relations for the cantilever mirror

$$\begin{aligned} \begin{pmatrix} \hat{b}_1 \\ \hat{b}_2 \end{pmatrix} &= -(\Xi^{-1})^2 \begin{pmatrix} \hat{a}_1 \\ \hat{a}_2 \end{pmatrix} \\ &= -(\mathbb{I} + \Pi \begin{pmatrix} M_{11} & M_{21} \\ M_{12} & M_{22} \end{pmatrix}) \begin{pmatrix} \hat{a}_1 \\ \hat{a}_2 \end{pmatrix}. \end{aligned} \tag{4.5}$$

The matrices M_{ij} indicate the ponderomotive part of the transfer matrix from $\hat{a}_i$ to $\hat{b}_j$.

$$M_{ij} \equiv 2\sqrt{I_i I_j}\begin{pmatrix} \cos\theta_i \sin\theta_j & \sin\theta_i \sin\theta_j \\ -\cos\theta_i \cos\theta_j & -\sin\theta_i \cos\theta_j \end{pmatrix} \tag{4.6}$$

Input-Output Relations for the Full System

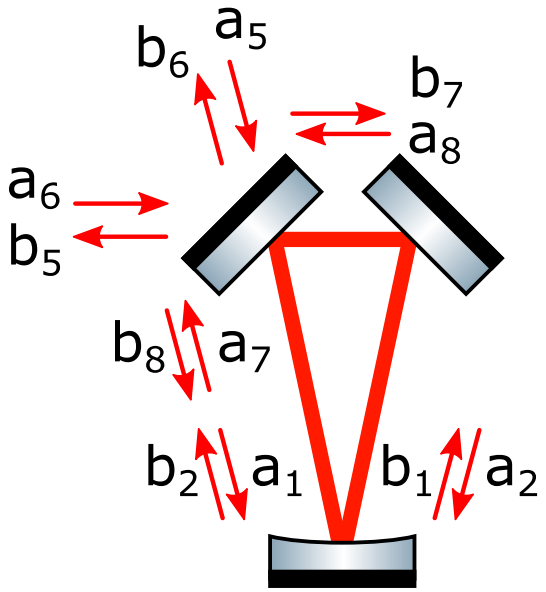

Figure 4.1: Triangular cavity labelled with input and output ports propagating in both directions.

The input-output relations for lossless ring cavity assuming the additional two mirrors are fixed (or very massive) can now be expressed based on 4.1 and 4.5 as

$$\begin{pmatrix}\hat{b}_1\\ \hat{b}_2\\ \hat{b}_5\\ \hat{b}_6\\ \hat{b}_7\\ \hat{b}_8\\ \hat{a}_1\\ \hat{a}_2\\ \hat{a}_7\\ \hat{a}_8\end{pmatrix} = \begin{pmatrix} -\mathbb{I}-\Pi M_{11} & -\Pi M_{21} & 0 & 0 & 0 & 0 & 0 & 0 & 0 & 0\\ -\Pi M_{12} & -\mathbb{I}-\Pi M_{22} & 0 & 0 & 0 & 0 & 0 & 0 & 0 & 0\\ 0 & 0 & \rho & 0 & 0 & \tau & 0 & 0 & 0 & 0\\ 0 & 0 & 0 & \rho & \tau & 0 & 0 & 0 & 0 & 0\\ 0 & 0 & 0 & \tau & -\rho & 0 & 0 & 0 & 0 & 0\\ 0 & 0 & \tau & 0 & 0 & -\rho & 0 & 0 & 0 & 0\\ 0 & 0 & 0 & 0 & 0 & 0 & 0 & 0 & 0 & e^{i\Omega l_1/c}\\ 0 & 0 & 0 & 0 & 0 & 0 & 0 & 0 & e^{i\Omega l_2/c} & 0\\ 0 & 0 & 0 & 0 & 0 & 0 & 0 & e^{i\Omega l_1/c} & 0 & 0\\ 0 & 0 & 0 & 0 & 0 & 0 & e^{i\Omega l_2/c} & 0 & 0 & 0\end{pmatrix} \begin{pmatrix}\hat{a}_1\\ \hat{a}_2\\ \hat{a}_5\\ \hat{a}_6\\ \hat{a}_7\\ \hat{a}_8\\ \hat{b}_1\\ \hat{b}_2\\ \hat{b}_7\\ \hat{b}_8\end{pmatrix}. \tag{4.7}$$

We can directly invert the above adjacency matrix, or reduce it to

$$\begin{aligned}\begin{pmatrix}\hat{b}_5\\ \hat{b}_6\end{pmatrix} &= \begin{pmatrix}\rho & 0\\ 0 & \rho\end{pmatrix}\begin{pmatrix}\hat{a}_5\\ \hat{a}_6\end{pmatrix} + \begin{pmatrix}0 & \tau\\ \tau & 0\end{pmatrix}\begin{pmatrix}0 & e^{i\Omega l_1/c}\\ e^{i\Omega l_2/c} & 0\end{pmatrix}[-\mathbb{I}-\Pi M]\begin{pmatrix}0 & e^{i\Omega l_1/c}\\ e^{i\Omega l_2/c} & 0\end{pmatrix}\\ &\quad * [\begin{pmatrix}0 & \tau\\ \tau & 0\end{pmatrix}\begin{pmatrix}\hat{a}_5\\ \hat{a}_6\end{pmatrix} + \begin{pmatrix}-\rho & 0\\ 0 & -\rho\end{pmatrix}\begin{pmatrix}\hat{a}_7\\ \hat{a}_8\end{pmatrix}].\end{aligned} \tag{4.8}$$

Using the relations at the the input beamsplitter and simplifying, we can recast this as

$$[\mathbb{I}-\rho e^{i\Omega L/c}(\mathbb{I}+\Pi M)]\begin{pmatrix}\hat{b}_5\\ \hat{b}_6\end{pmatrix} = [\rho\mathbb{I}-\tau^2 e^{i\Omega L/c}(\mathbb{I}+\Pi M)-\rho^2 e^{i\Omega L/c}(\mathbb{I}+\Pi M)]\begin{pmatrix}\hat{a}_5\\ \hat{a}_6\end{pmatrix}. \tag{4.9}$$

In the lossless case, we can express the input-output relations explicitly as

$$\begin{pmatrix}\hat{b}_5\\ \hat{b}_6\end{pmatrix} = \Upsilon\begin{pmatrix}\hat{a}_5\\ \hat{a}_6\end{pmatrix} \tag{4.10}$$

$$\begin{aligned}\Upsilon &\equiv -e^{i2\eta}\begin{pmatrix}\mathbb{I}+\mathcal{K}_{11} & \mathcal{K}_{21}\\ \mathcal{K}_{12} & \mathbb{I}+\mathcal{K}_{22}\end{pmatrix}\\ e^{i2\eta} &\equiv \frac{e^{i\Omega L/c}-\rho}{1-\rho e^{i\Omega L/c}}\\ \mathcal{K}_{ij} &\equiv \frac{\tau^2}{1-2\rho\cos(\frac{\Omega L}{c})+\rho^2}\Pi M_{ij}.\end{aligned} \tag{4.11}$$

As usual, the Mach-Zehnder lets us treat the differential arm mode coupled to the signal ("dark") ports separately from the common arm mode coupled to the pumped ("bright") ports, and the expression in 4.11 holds for the differential and common modes separately.

The expressions above will be modified slightly if we allow the other two cavity mirrors to be ponderomotively active (relaxing the assumption of large mass compared to the third mirror). We will explore this to some extent in numerical simulations, but will not derive the explicit expressions.

4.2 Signal-, Power-, and Arm-Recycled Mach-Zehnder Interferometers

To complete the analogy of a Mach-Zehnder interferometer to a dual-recycled Fabry-Perot Michelson interferometer, we can add normal incidence mirrors to both signal ports of PARMZI (as in Fig. 4.2). As was the case for power recycling, the signal recycling cavity has an additional degree of freedom relative to DRFPMI. In addition to overall signal cavity length detuning, which takes the interferometer from signal recycling to resonant sideband extraction, the relative phase of forward- and reverse-propagating signal fields is tunable.

One choice of Mach-Zehnder and recycling cavity tunings establishes a system completely analogous to the Sagnac speedmeter with ring cavities considered by Chen [72]. However, we will discover that the extra degrees of freedom can lead to an optical spring in the resonant differential arm cavity.

Tuned to its dark fringe, the Mach-Zehnder interferometer lets us treat separately the signal recycling cavity coupled to differential arm motion and the power recycling cavity coupled to common arm motion. The simplified common and differential mode systems are represented in Fig. 4.2.

In a procedure nearly identical to section 4.1, the input-output relations for SPARMZI tuned to the MZI dark fringe can be written as

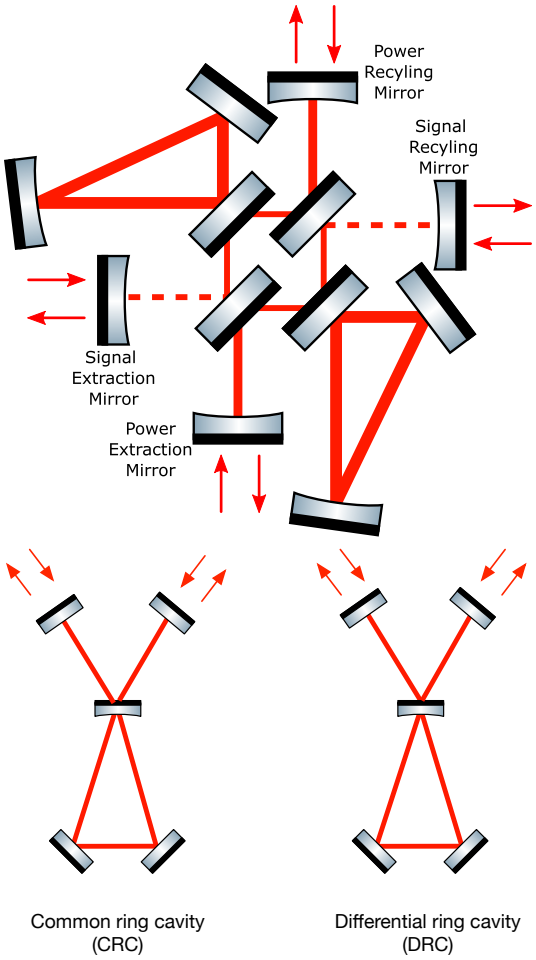

Figure 4.2: Recycled Mach-Zehnder layout. Top to bottom: SPARMZI layout, showing MZI tuning for distinct signal- and power- recycling (or extraction) cavities; decomposition into differential and common mode recycled ring cavities of SPARMZI. SM1 is the "signal extraction mirror" with amplitude reflectivity and transmissivity ρ_1, τ_1; SM2 is the "signal recycling mirror" with amplitude reflectivity and transmissivity ρ_2, τ_2; ITM is the "intermediate test mass" with amplitude refectivity and transmissivity ρ, τ; ETM is the "end test mass" with mass m.

$$
\begin{aligned}
[\mathbb{I} + \tau_e \tau_r e^{i\Omega L_{\mathrm{SRC}}/c} \Upsilon \begin{pmatrix} 0 & \rho_e \\ \rho_r & 0 \end{pmatrix}] \begin{pmatrix} b_{fwd} \\ b_{rev} \end{pmatrix} = \\
[\begin{pmatrix} 0 & \rho_2 \\ \rho_1 & 0 \end{pmatrix} + \tau_1 \tau_2 e^{i\Omega L_{\mathrm{SRC}}/c} \Upsilon + e^{i\Omega L_{\mathrm{SRC}}/c} \begin{pmatrix} \rho_2^2 & 0 \\ 0 & \rho_1^2 \end{pmatrix} \Upsilon] \begin{pmatrix} a_{fwd} \\ a_{rev} \end{pmatrix}.
\end{aligned}
\tag{4.12}
$$

The LHS of Eq 4.12 has two unique eigenvalues, each with twofold degeneracy. Using the expressions from Eq 4.11 and 4.6, these eigenvalues are

$$\lambda_{\pm} = 1 \pm i\Pi \frac{\tau^2 \sqrt{I_1 I_2 \rho_1 \rho_2 \sin 2\theta_1 \sin 2\theta_2}}{(\rho e^{iL\Omega/c} - 1)^2} e^{i\Omega(L+L_{\mathrm{SRC}})/c}. \tag{4.13}$$

Eq 4.13 points to the existence of several optomechanical resonances. One is an optical spring associated with detuning the main arm cavities, represented by L. Even with the arm cavities on resonance, another optical spring arises from detuning the signal recycling cavity with L_{SRC}. Yet even when L_{SRC} does not produce a resonance (for example, $e^{i\Omega(L+L_{\mathrm{SRC}})/c} = i$), the phases θ_1, θ_2 can establish an optomechanical resonance. The resonance set by θ_1, θ_2 is due to relative phase accumulation of the pump and signal fields on multiple passes of the mechanically susceptible optic (in this case, clockwise and counter-clockwise trips around the ring cavities). While finalizing this manuscript, the author learned that Khalili has independently derived and generalized the mechanism of the double-pass optical spring, and studied a system equivalent to Eq. 4.12 with $T_{\mathrm{SEM}} = 1$ and $R_{\mathrm{SRM}} = 0$, in [73].

Though it is straightforward to write down the adjacency matrix for SPARMZI when the MZI is tuned to a dark fringe, the most general closed-form input-output relations are complicated. We explore this configuration numerically below.

4.3 Quantum Coherent GW Interferometers

Nonlinearity can be used to exceed the standard quantum limit for linear measurement of classical signals [74] [75].

Phase sensitive filtering and amplification, which treats both optical quadratures equally, can be useful for compensating the phase delay of resonant sensors without increasing sensitivity to intra-sensor optical losses [76] [77] [78]. A specific case of interferometers with phase-insensitive filtering has received significant attention for loss tolerant quantum noise cancellation by operating at an exceptional point or with a PT-symmetric Hamiltonian [79] [80] [81] [82]. EPR entangled intererometers are discussed in [83].

Non-reciprocal quantum sensing relies on an asymmetry between signal- and noise-coupling or forward- and reverse- propagation through the device to escape the typical tradeoff between signal gain and sensor isolation [84] [85] [86] [87] [88] [89]. $SU(1,1)$ interferometry is discussed in [90] [91].

Phase-Sensitive Quantum Filters

In Fig. 4.3, we adapt the control system schematic from [92] for the case of a phase sensitive filter (PSF). We can optimize Y to maximize the signal to noise ratio of $\hat{a}_{\text{out}}$ for sensing h subject to noise $\hat{n}_q$ entering only at the detector port. As long as the PSF obeys unitarity (as does PARMZI above), we do not need to add additional quantum noise at the amplifier as in the case of generic linear amplifiers.

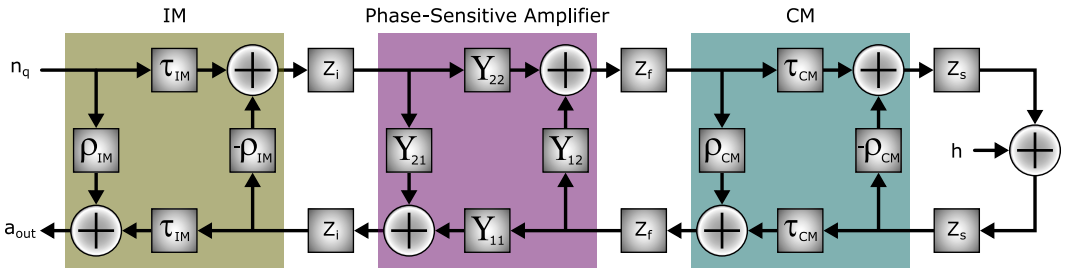

Figure 4.3: Control system diagram of homodyne phase sensitive linear amplifier, in our example PARMZI, in the filter cavity typical of gravitational wave interferometers. Inspiration drawn from the figure in [92].

To solve for the contribution at $\hat{a}_{\text{out}}$ due to fields entering at $\hat{n}_{\text{q}}$ and $\hat{h}$, one can write down the adjacency matrix A for the MIMO system and invert $1 - A$ to find the closed-loop transfer functions.

Unitarity imposes conditions on the matrices Y in Fig. 4.3, which collectively have 4 degrees of freedom (two amplitudes and two phases) at each frequency. These are sufficient to maximize signal coupling while minimizing noise coupling to the output. The phase-sensitive amplifier behaves nonreciprocally to create the following coupling (with some abritrary choice of quadratures for concreteness)

- Noise entering at $\hat{q}_{\text{cos}}$ is resonantly transmitted and amplified to $\hat{h}_{\text{cos}}$
- Noise entering at $\hat{q}_{\text{sin}}$ is resonantly transmitted and de-amplified to $\hat{h}_{\text{sin}}$
- Noise entering at $\hat{h}_{\text{cos}}$ is resonantly transmitted and de-amplified to $\hat{a}_{\text{out,sin}}$
- Signal entering at $\hat{h}_{\text{sin}}$ is resonantly transmitted and amplified to $\hat{a}_{\text{out,sin}}$.

One can already see that the effect of optical losses and amplifier noises will become relevant due to the round-trip deamplification-amplification for noise entering at the readout port. The quantity and distribution of optical losses and displacement noises throughout the various subsystems will determine an optimal amplifier gain and level

of squeezing injected at the dark port. However, as long as the system properties determine an optimal amplifier gain $|G_{\rm fwd}(\Omega)||G_{\rm rev}| > 1$, the input-referred noise due to dark port vacuum fields is roughly $|G_{\rm fwd}||G_{\rm rev}|$ lower than for the IFO with phase-insensitive filtering described in [92].

Another way of viewing the behavior of the filter cavity is as a circulator-squeezer. The phase-sensitive amplifier antisqueezes (amplifies) the signal-carrying quadrature on the way from the sensing cavity to the device output. And it instead squeezes (de-amplifies) the vacuum field quadrature that must inevitably reach the signal input due to the photodetection process. The filter cavity around the phase-sensitive amplifier acts to set the impedance matching condition such that any reflected field must pass through the amplifier in both directions before reaching the photodetection port.

In Figures 4.4 and 4.5, we compare the performance of one phase-sensitive filter to the cases considered in [92]. "Resonant Sideband Extraction" (RSE) refers to the cavity formed by IM and CM being $\pi/2$ off-resonance with no filtering ($Y_{ij} = 1$), such that signal sidebands are resonantly transmitted through the input-filter cavity. "Signal Recycling" (SR) refers to the cavity formed by IM and CM being on-resonance with no filtering ($Y_{ij} = 1$), enhancing signal buildup at DC. The Optimal Phase-Insensitive Filter is described in [92] as RSE with a unity gain phase-insensitive filter defined by

$$\begin{aligned} Y_{11}^{\rm PIF} &= Y_{22}^{\rm PIF} = \sqrt{\frac{i\Omega + \gamma_s}{i\Omega - \gamma_s}} \\ Y_{12}^{\rm PIF} &= Y_{21}^{\rm PIF} = 0 \\ \gamma_s &\equiv \frac{c\tau_{CM}^2}{4L_s}. \end{aligned} \tag{4.14}$$

The "Phase-Sensitive Filter+Amplifier" starts with the same overall phase as the Phase-Insensitive Filter case, but allows Y_{ij} to take a form inspired by M_{ij} in Eq 4.6. Eq 4.15 implements the same form of phase-sensitive filtering as PARMZI, but with the optimal phase-insensitive phase replacing the phase (and frequency-dependence) imposed by the PARMZI ring cavity and mechanical susceptibility.

$$M_{ij}^{\mathrm{PSF}} = 2G_iG_j \begin{pmatrix} \cos\theta_i \sin\theta_j & \sin\theta_i \sin\theta_j \\ -\cos\theta_i \cos\theta_j & -\sin\theta_i \cos\theta_j \end{pmatrix}$$
$$Y_{ij}^{PSF} = (\delta_{ij}\mathbb{I} + M_{ij})\sqrt{\frac{i\Omega + \gamma_s}{i\Omega - \gamma_s}} \tag{4.15}$$

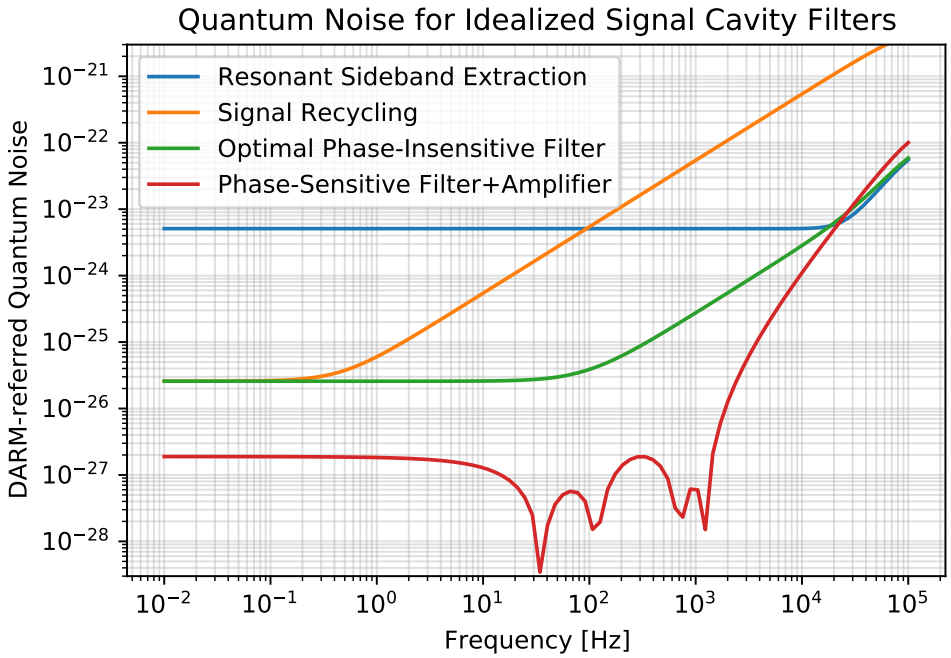

Figure 4.4: Input-referred quantum noise for lossless resonant sensors as in Fig. 4.3 with various filters inside signal cavity.

Figs. 4.4 and 4.5 show that the phase-sensitive filter suppresses input-referred quantum noise, but at the expense of some signal gain. Furthermore, the noise suppression is affected by the fine tuning of the input and filter cavities, as suggested by the resonances visible in the input-referred quantum noise between 10 Hz and 1 kHz, and the noise is actually amplified at high frequency. This should not be a fundamental limitation of internal phase sensitive filtering, but a more general expression for Y_{ij}^{PSF} and further optimization is required to realize the full benefits and identify the true limitations. In particular, one may expect that the optimal overall phase for PSF is not the same as that for PIF.

There are some benefits to placing the PSA inside the filter cavity, rather than using the combination of a directional amplifier like PSOMA, a circulator, and frequency-dependent squeezed light injection. First, the benefits of phase-sensitive

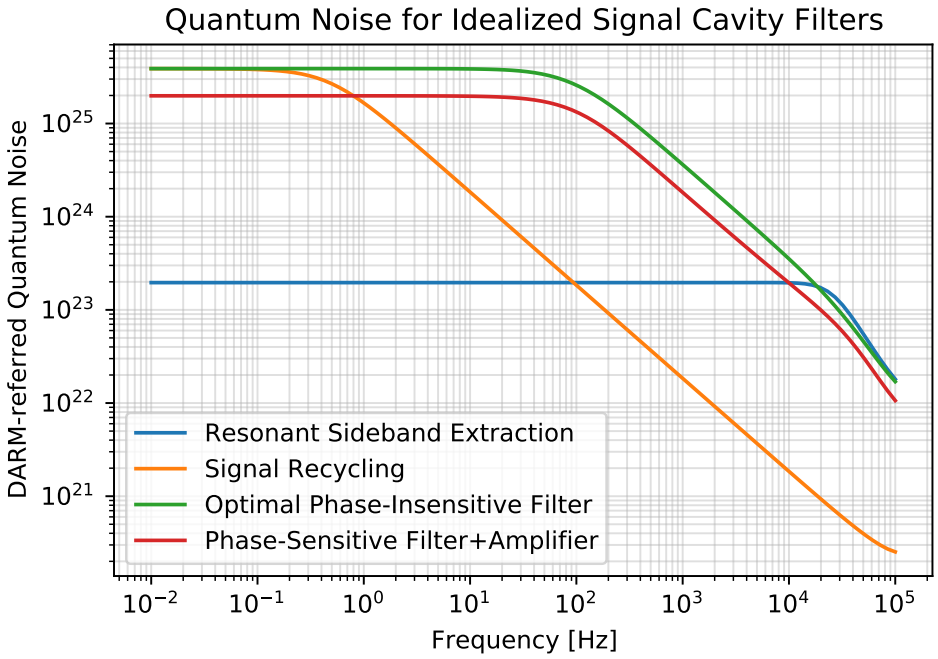

Figure 4.5: Signal gain for lossless resonant sensors as in Fig. 4.3 with various filters inside signal cavity.

preamplification for downstream optical loss immunity are moved closer to the signal port. Further, because signals encounter the amplifier from one direction only (h), but amplifier noises are coherently injected towards both the IM and CM, it would be interesting to search for amplifier noise free configurations. For example, if the PSA is a ponderomotive amplifier like PARMZI, one may want to choose for displacement noises at PARMZI cavity mirrors to appear in the quadrature orthogonal to signals injected with h.

PARMZI in the Signal Recycling Cavity

If we replace the generic phase-sensitive filter in section 4.3 above with the input-output relations of PARMZI, we can understand one specific instance of phase-sensitive filtering applied to GWIFO. In Figs. 4.6 and 4.7, we considered a lossless dual recycled Fabry-Perot Michelson Interferometer (DRFPMI) and numerically minimized differential arm length strain (DARM)-referred quantum noise over SEC detuning, forward- and reverse- PARMZI pump power and phase, and foward- and reverse- PARMZI signal phase.

Fig. 4.6 shows the quantum noise ASDs for DRFPMI with Voyager-like parameters tuned for resonant sideband extraction, along with the curves for infinite-mass

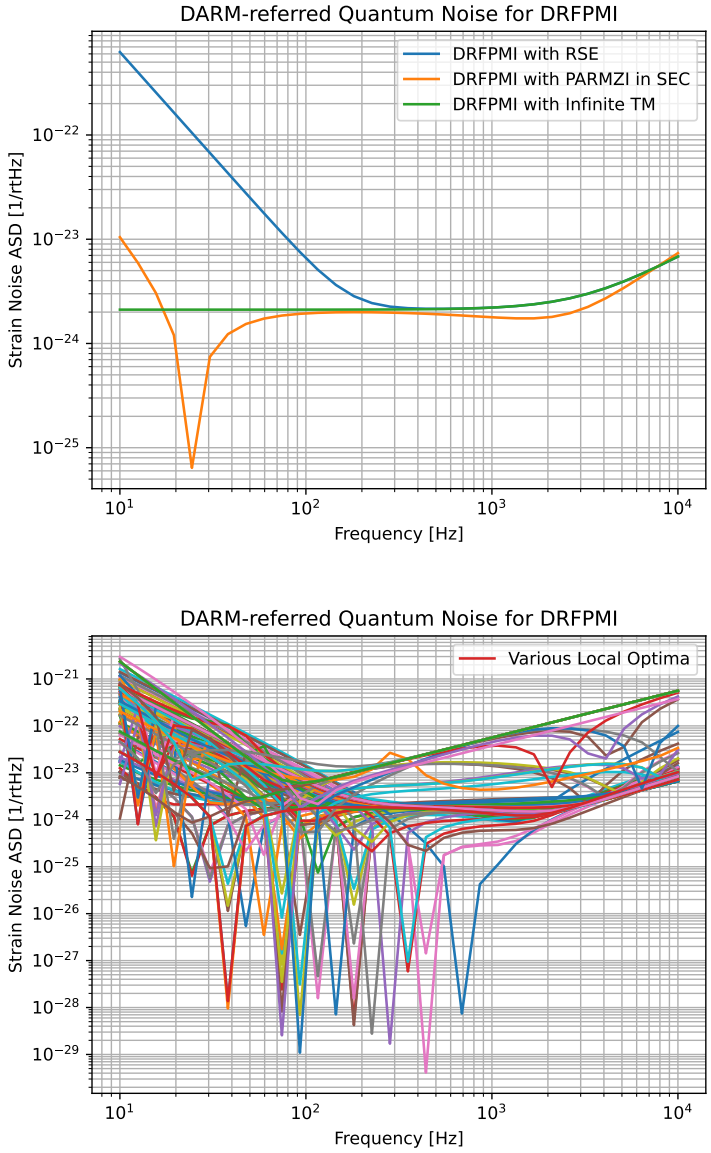

Figure 4.6: Strain sensitivity for PARMZI inside the SEC. Top to bottom: Input-referred strain sensitivity for Voyager-like GWIFO with addition of optimal PARMZI inside the signal extraction cavity; many local optima for PARMZI inside SEC parameter choices.

Fabry-Perot test masses (TMs) and for PARMZI optimized for 200 kg TMs and no displacement noises or optical loss. The quantum noise curve with PARMZI in the SEC has a modest improvement from 1-6 kHz due to compensating the DARM cavity pole over these frequencies. Below 300 Hz, PARMZI implements backaction evasion essentially analogous to variational readout [56], but with some resonant gain due to an optical spring formed by the ring cavity mirrors and the counterpropagating PARMZI pumps. With no displacement noise, the optimal spring resonance

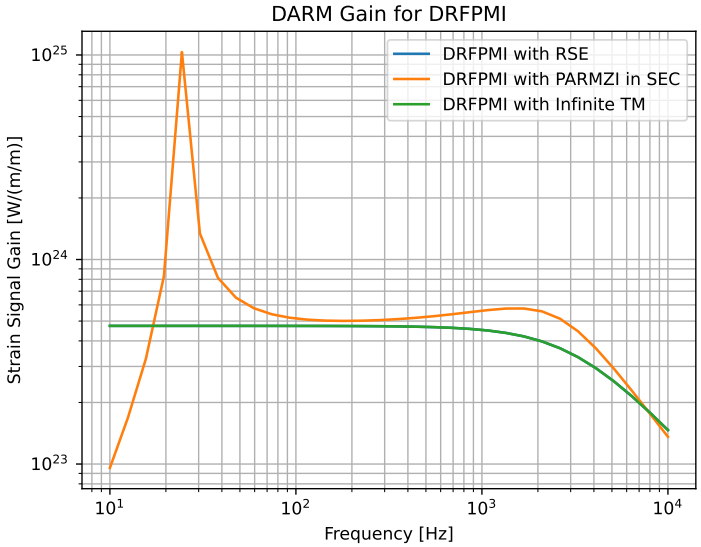

Figure 4.7: Differential strain signal gain for Voyager-like GWIFO with addition of PARMZI inside the signal extraction cavity.

is at several 10s Hz, but considering Brownian noise in DARM and suspension thermal noise of PARMZI would likely push the optimal resonance to higher frequency as in the second plot of 4.6. We expect the quantum noise improvement to be resilient against intracavity optical losses because the improvement is due to gain enhancement rather than noise suppression, but this should be shown explicitly.

4.4 Dual Recycled Mach-Zehnder Interferometers for Gravitational Waves

As discussed above, SPARMZI is one type of phase-sensitive amplifier for optical fields. SPARMZI has several unique features relative to similar, previously explored filtering and amplification schemes.

The ponderomotive interaction is a third order nonlinearity, similar to materials with χ^3 optical nonlinearities (Kerr media). [93] explores some of the tradeoffs for χ^2 and χ^3 optical nonlinearities. However, purely optical nonlinearities build up gain along a propagation length of many laser wavelengths, and therefore do not amplify on both transmission and reflection as in PARMZI or SPARMZI. The benefit of optomechanical over all-optical amplifiers is lower optical loss, with a tradeoff in displacement noise at the ponderomotively active mirror and less gain at high frequency.

SPARMZI as Resonant Strain Sensor

This subsection uses a Finesse3 model to investigate SPARMZI with Voyager-like parameters. We consider ring cavities with 4 km arm lengths (8 km cavity round trip) and 200 kg test masses. To comply with the anticipated thermal budget of the cryogenically cooled TMs, the laser power is 1.5 MW circulating in each direction of each ring cavity such that the total laser power incident on each mirror is 3 MW. The model includes optical loss, but no displacement noise. Note that one could minimize optical loss per unit arm strain by using bowtie cavities in place of ring cavities in each arm, but this does not affect the major features. For simplicity, one power-recycling and one signal-extraction mirror are set to 0 transmissivity, such that two of the four ports of the Mach-Zehnder are closed except for optical loss. Fig. 4.8 shows the DARM-referred quantum noise for SEC and PRC tunings analogous to RSE, for numerically optimized tunings, and for the same numerically optimized tuning but with infinitely massive mirrors.

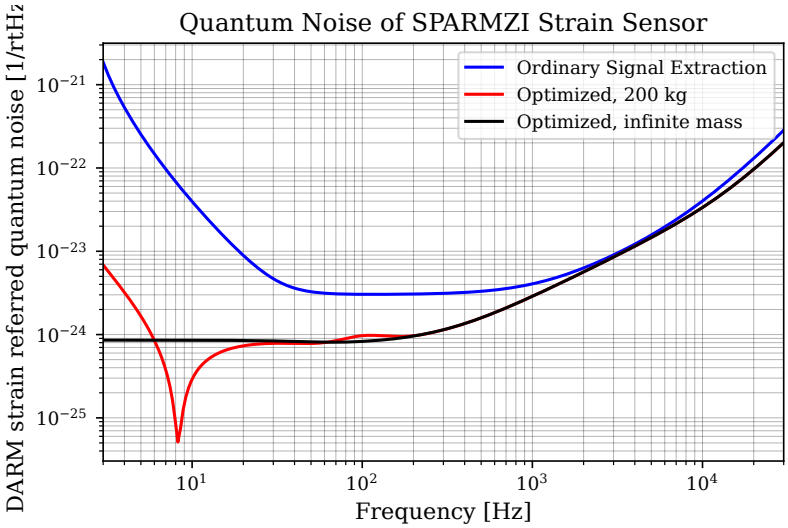

Figure 4.8: DARM-referred strain sensitivity for SPARMZI with Voyager-like parameters.

As shown in Fig. 4.9, the quantum noise improvement afforded by the extra degrees of freedom in SPARMZI relative to RSE is due to signal enhancement, not noise cancellation. The resonance around 8 Hz is due to an optical spring whereby differential strain signals generate phase sidebands in the SEC, which then recombine at input/output beamsplitters in-phase with the pump to ponderomotively drive test-mass position. As in section 4.3, this is a novel mechanism for generating an optical spring, since all pumped cavities are on-resonance.

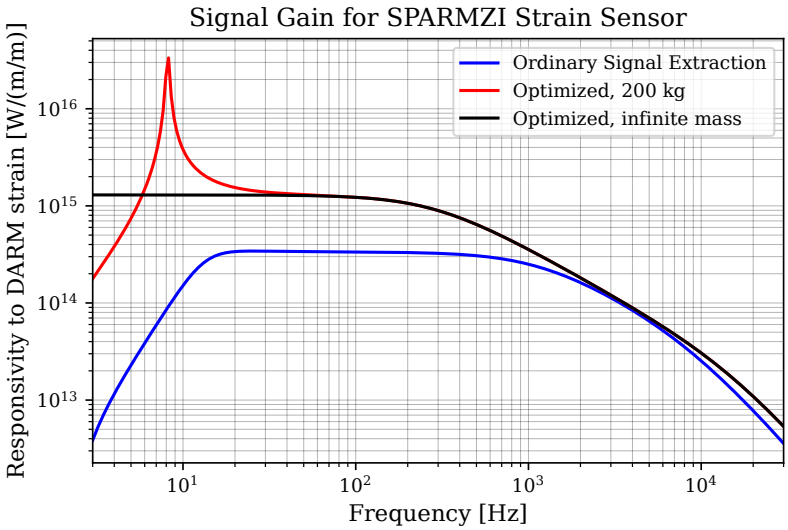

Figure 4.9: Differential strain signal gain for SPARMZI with Voyager-like parameters

Some Other Schemes

SPARMZI is an exciting new building block for optomechanical sensors, which immediately suggests plethora reconfigurations, and a few are drawn in Fig. 4.10.

The obvious drawback of SPARMZI is that half of the strain signal enters the SEC in the "wrong" direction, and must encounter the arm cavities before SEM in the first cavity round trip. If the SRM were instead transmissive, one could consider coherently sensing at both signal-coupled ports.

In analogy with [72], one could also detune the Mach-Zehnder such that the pump encounters three of the four recycling mirrors. This still leaves one interferometric degree of freedom more than the MZI speedmeter in [72].

Some have suggested placing a χ^3 material in the arm cavities of a FPMI, and one could study the MZI in this context.

One could also consider coherently combining the two signal ports before introducing signal recycling mirrors. This leads to a configuration analogous to the L-shaped resonator considered in [94] [95], which exhibits excellent and loss-tolerant high frequency sensitivity due to its common and differential modes having different resonant frequencies.

Those interested in tabletop tests of gravitationally coupled quantum systems may consider configurations with bowtie traveling wave cavities in a folded MZI. This permits the test masses to be brought close together.

Finally, one may consider whether traveling wave cavities with mechanically coupled test masses could be used for displacement noise free interferometry, as in [96] [97].

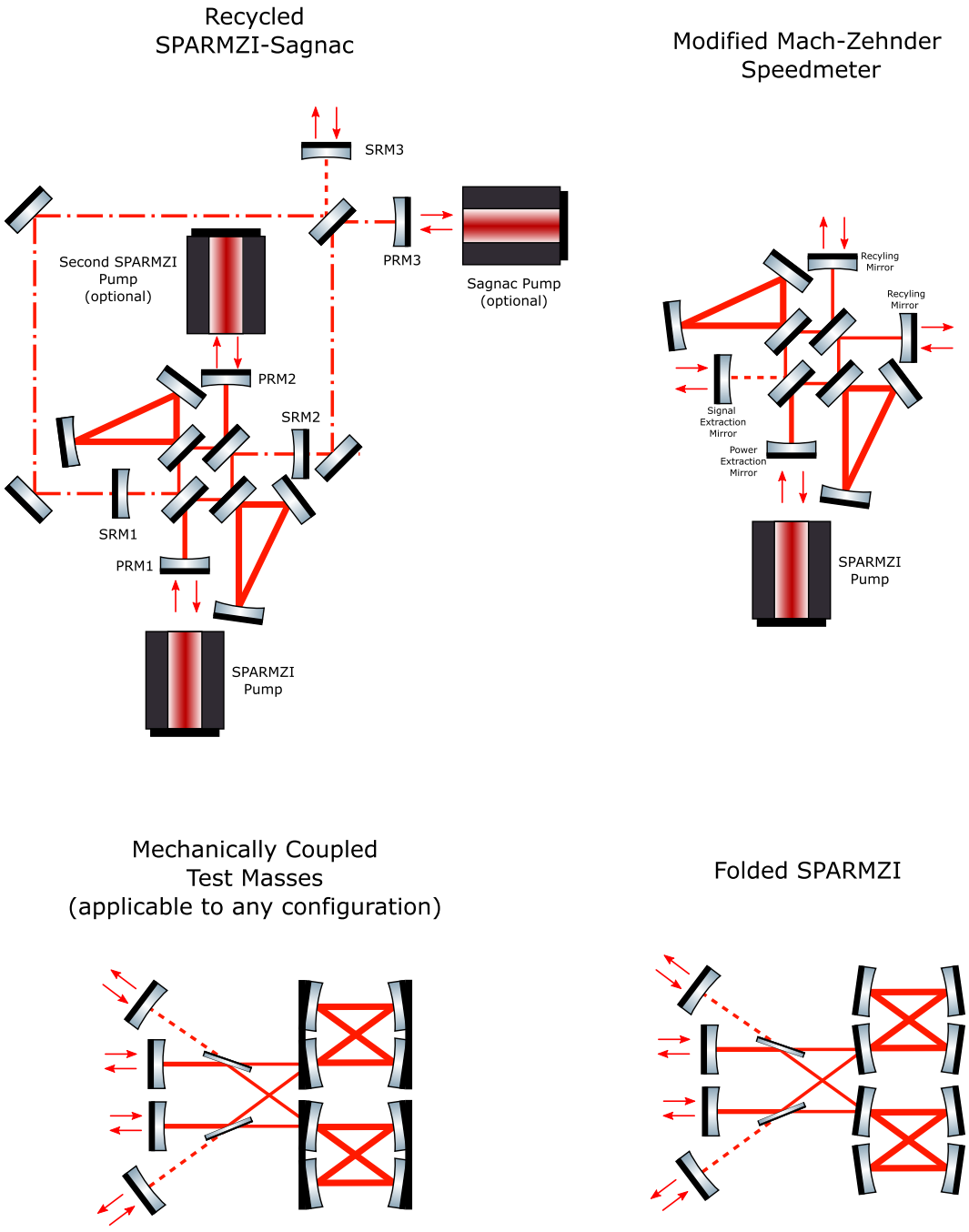

Figure 4.10: Some configurations involving SPARMZI-like interferometers for future study.

Part II

Silicon Mechanics

Fabrication and characterization of gram-scale mirrors

Chapter 5

SILICON FABRICATION

High quality mechanical oscillators are at the heart of the optomechanics experiments described in this work. Silicon is a promising material for mirror substrates due to its extremely low mechanical loss near 123 K and low optical absorption for short infrared light. This chapter introduces the much larger body of literature on silicon fabrication, and describes a few small experiments undertaken to improve our group's application of old techniques.

5.1 Surface Cleaning and Passivation

For the Q measurement apparatus described in Chapter 6, we require 2" or 3" substrate wafers with extremely low mechanical loss. Imperfections in the Si crystal structure due to surface defects can contribute mechanical loss, as can the presence of contaminents on the Si surface. Surface contaminants can also affect the properties of thin films deposited on the Si wafers, which may be relevant for the film's optical or mechanical properties.

RCA Clean

To prepare a silicon wafer for further processing, we first remove any surface contaminants with an "RCA clean," a standard cleaning procedure first developed by Radio Corporation of America [98]. Our procedure is as follows:

1. Bath in solvent to remove oils and organic materials. We use a room temperature bath of acetone for 3 minutes, followed by methanol for 3 minutes. After soaking, rinse the wafer in running DI water for 3 minutes.

2. Bath in a 1:5:1 solution of ammonium hydroxide, water, and hydrogen peroxide at 70 ± 5° C for 15 minutes. The basic solution removes remaining organic residues and oxidizes the silicon surface. After soaking, immerse the solution under DI water for several water changes and remove the wafer from the solution while running water to avoid depositing contaminants on the wafer as it passes through the unbroken water surface. The wafer should be hydrophilic, indicating the presence of a silicon dioxide layer.

3. Bath in a 1:5:1 solution of hydrochloric acid, water, and hydrogen peroxide at 70 ± 5° C for 15 minutes. The acid solution removes metallic contaminants and some ammonium-insoluble hydroxides. Rinse the wafer under running DI water as in the previous step, and again verify that the surface is hydrophilic.

4. Dry the wafer with dry filtered nitrogen gas.

HF Etch

Bare silicon quickly develops a silicon dioxide surface layer by reacting with water in the air or bath. The SiO_2 layer introduces excess mechanical loss.

To remove the oxide passivation layer following RCA clean, we etch the wafer in a dilute solution of buffered hydrofluoric acid (0.75%) for 2 minutes. The HF etch removes the oxide and etches the Si crystal along highly specular surfaces.

Plasma-Enhanced Chemical Vapor Deposition

Immediately after HF etch and before a thermal oxide layer forms on the Si surface, we deposit a passivating layer of silicon nitride using plasma-enhanced chemical vapor deposition (PECVD). The SiNx layer prevents the silicon from reacting with atmospheric water, and has much lower mechanical loss than SiO_2.

5.2 Cantilever Fabrication

Rectangular Cantilevers

The simplest method of reducing Si wafers to pieces with the desired mechanical resonances is by scribing and breaking the ⟨100⟩ wafer along its crystal lattice. We use a Dynatek GST-150 Scriber-Breaker to produce rectanuglar wafers with several mm to several cm lengths with good reproducability.

One drawback of simple rectangular wafers is their high mechanical loss due to significant coupling to the clamp that holds one end of the cantilever. Also, bonding the cantilever directly to an optic will introduce an additional uncoated Si surface that scatters light from the beam transmitted through the optic and cantilever.

The cantilevers utilized in Part III were fabricated by Korth [99] using a process developed by the Chao group at National Tsing Hua University [100]. The process uses optical lithography followed by deep reactive ion etching to form a thick SiNx mask on both sides of the cantilever. The mask selectively protects the silicon during a KOH etch process such that the resulting cantilever is thick at either end

(where the clamp or optic touch the cantilever) but thin in the middle. We also etch a through-hole that sits behind the optic to allow beam clearance.

The resulting cantilevers have mechanical losses around 2.6×10^{-6} at 100 K, consistent with clamping and surface quality-related losses [99]. The thinned central region of the cantilever contains most of the strain-energy associated with low frequency eigenmodes, thus diluting clamping losses.

5.3 Potassium Hydroxide Etch Characterization

Surface roughness can create slip-stick losses at clamping interfaces, as well as increase the area available for relatively lossy in SiNx or thermal oxide surface layers. A wet KOH etch process sets the surface roughness of our Si cantilevers. The literature on Si wet etching suggests higher KOH molarity reduces both surface roughness and etch rate, while elevated bath temperature increases etch rate but reduces surface roughness [101].

We used atomic force microscopy (AFM) to characterize the evolution of surface roughness of B-doped ⟨100⟩ Si samples during a wet etch with 50% w/v (13.4 M) KOH held at 50 C and continually agitated. The duration of KOH etch varied by sample.

Samples were prepared by breaking a 500 μm thick Si wafer into 10 mm × 20 mm rectangles with a Dynatek scriber-breaker. Each sample was RCA cleaned with the recipe in Sec 5.1. Samples were etched for 2 min in 2.5% buffered HF, then rinsed for 2 min in running DI water, immediately prior to KOH etching. Following KOH etching, samples were washed in DI water for another 2 minutes.

We used a Bruker Dimension Icon AFM in PeakForce Tapping mode to measure surface height on a 256×256 nm square grid with 512 points in each direction. We used ScanAsyst to automatically adjust probe feedback gain and setpoint, but we manually set z-range to a relatively low 1.27 μm to improve vertical resolution over our featureless scan regions.

A control sample that was only RCA cleaned had mean roughness $R_a = 0.439$ nm and RMS roughness $R_q = 0.546$ nm, indicating HF etch alone improved surface roughness by 40-60%. Fig. 5.1 shows that mean surface roughness increased then stabilized to 1.6nm for long duration etches. RMS roughness continued increasing even for long duration etches, though this may have been due to pitting visible in the photos of Fig. 5.2 and could be mitigated by increasing KOH bath temperature. The etch rate for the first 60 minutes of etching was 0.42 μm/min, while the average

rate between 60 and 382 minutes of etching was 0.32 μm/min. The decrease in etch rate over time is consistent with the observation of [101] that increasing roughness exposes more slow-etching $\langle 111 \rangle$ planes of the Si crystal.

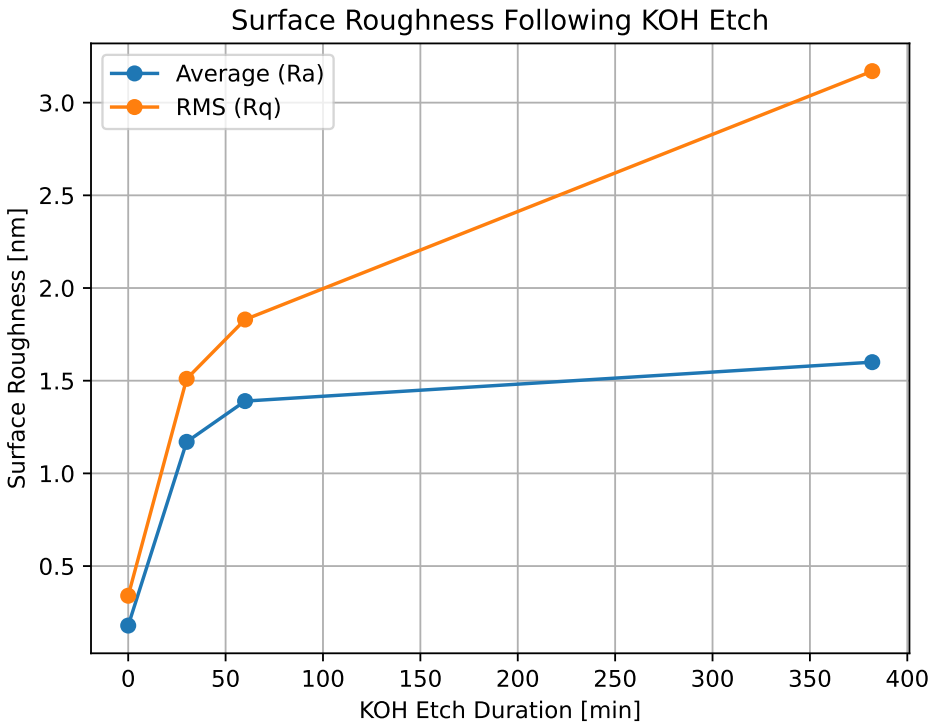

Figure 5.1: Average and RMS surface roughness of Si wafers after KOH wet etch followed by water rinse, measured with AFM. Roughness at 0 min was measured on samples that were not KOH etched.

5.4 Process Refinement

We recommend that future Si cantilever fabrication based on [99] use 50% w/v KOH but return to an 80 C bath temperature. It would be useful to repeat surface roughness measurements following post-etch HF rinse, water wash, and SiNX deposition, to identify to what extent these post-etching processes impact the final surface roughness. Future measurements would also benefit from decreasing AFM scan resolution and increasing scanned area to capture the μm-sized features visible in Fig. 5.2 especially for long-duration etches.

Note that in this study, we decreased the bath temperature relative to that used by [99] in order to slow the etch rate and more precisely control etch depth. The rate implied by measurements in [99] underestimated the rate observed over short-duration etches on thinner ($<$ 300 μm) wafers. To precisely tune the ultimate

thickness (and resonant frequency) of our cantilevers, it would be useful to repeat etch rate measurements over short intervals up to 2 hours.

Alternatively, one could try to avoid entirely the surface roughness associated with KOH etching. Rather than thinning the cantilever midsection, one could instead thicken the clamped region by optically contacting Si rectangles on either side of the cantilever underneath the steel clamp. Further study is needed to determine the clamping and interface losses of optically contacted Si, but we would expect reduced surface losses along the length of the cantilever. Furthermore, alternative anisotropic etching techniques like deep reactive ion etching could be explored for creating vertical etches through the entire Si wafer for laser beam transmission.

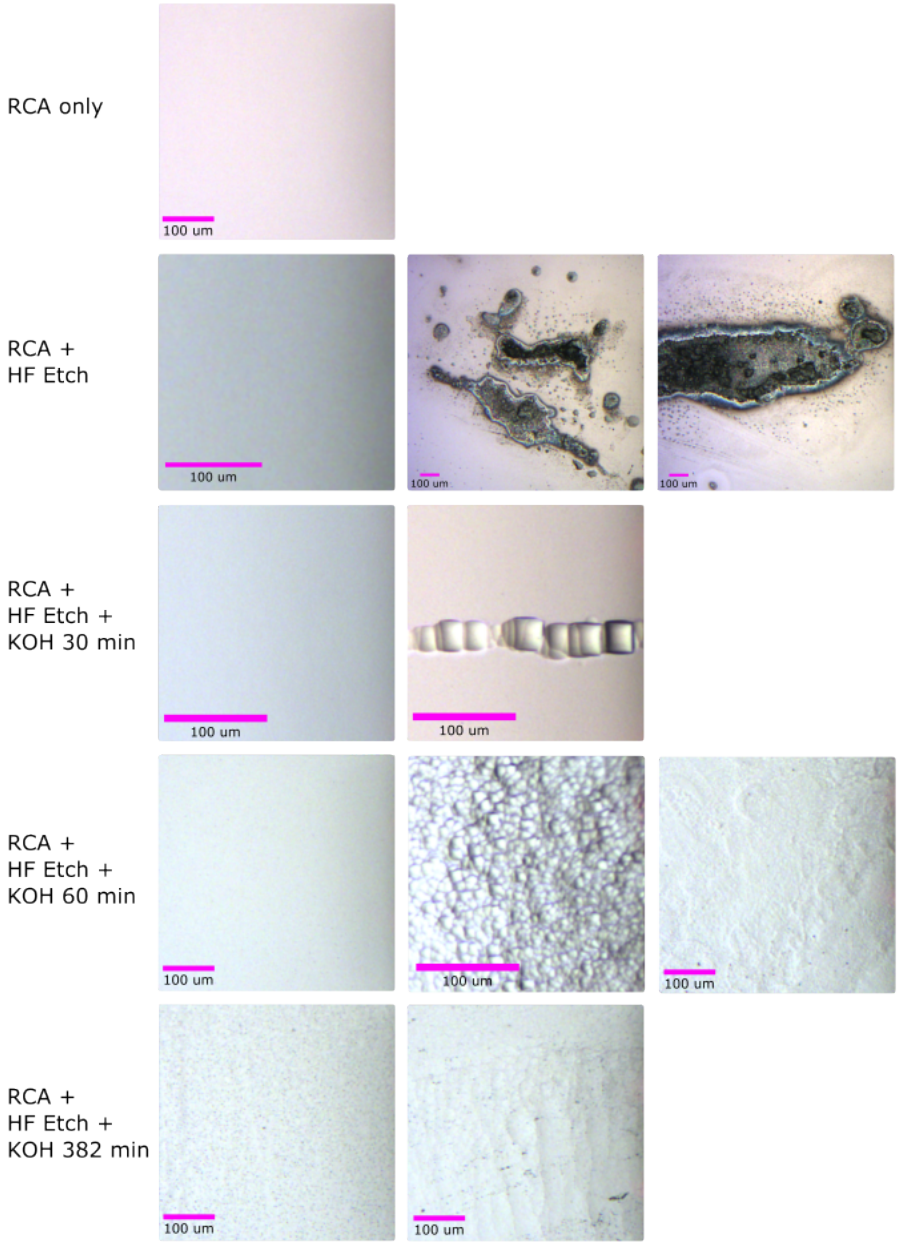

Figure 5.2: The stills captured from the AFM's video microscope are ordered from top to bottom by increasing KOH etch time, starting with RCA-cleaned samples with no HF or KOH etching. The left-most column are taken near the location of the AFM scan quoted in the roughness measurements. The other columns show pitting or contamination elsewhere on the sample.

Chapter 6

CRYO Q EXPERIMENT

Due to the fluctuation dissipation theorem, mechanical loss is a reasonable way of estimating the expected Brownian thermal noise contribution of a particular material or optomechanical element. Brownian thermal noise is one of the limiting noises of many cavity-stabilized frequency measurements [102].

For next generation gravitational wave interferometers, we expect to use cryogenic silicon optomechanics cooled to 123 K to allow for longer carrier wavelength (2 um interferometry) with low absorption, and lower thermal noise due to both reduced thermal bath temperature and coupling of acoustic phonons to that bath [41]. We also need to enhance the natural emissivity of Si [103] [104] to radiatively cool the test masses.

This series of experiments aimed to develop a testbed for measuring the temperature-dependent mechanical loss of thin films such as a-Si (which exhibits incredibly low mechanical loss for reasons discussed in [105]) to explore the parameter space of materials and deposition processes [106] [107] for optical coatings in cryogenic GW observatories. We also want to characterize the thermal noise contribution of high emissivity coatings that could be applied to the barrel of GWIFO test masses to increase their radiative coupling for temperature control.

Many experiments have measured the quality factor of Si, typically by observing ringdowns of mechanical eigenmodes of clamped [108] or nodally suspended [109] [110] wafers or cantilevers. The ringdown measurements are then be used to extract mechanical propertise of thin films deposited on the Si oscillators [111], [112], [113], [114], [115], [116], [117] [118] [119].

Our considerations of mechanical and thermal design are similar to and informed by experiments characterizing other properties of Si bonds such as breaking strength and thermal conductivity [120] [121], [122], [123], [124].

6.1 Target Testbed Quality Factor

Optimal experimental design requires clearly defining the target measurement sensitivity from the outset. As described above, we want to measure the mechanical loss ϕ_{coating} of a thin film deposited on a wafer of single crystalline silicon. We first

develop a detailed physical model of mechanical loss $\phi_{\mathrm{Si}}(\vec{\mu})$ of the silicon wafers in our experiment by measuring the quality factor $\{Q_i\}$ and eigenfrequencies $\{f_i\}$ of several mechanical eigenmodes of the wafer. The Q_i and f_i are together determined by a set of material and experimental parameters $\vec{\mu}$ (in which the parameter i indexing mode number could be included, if desired).

We then measure eigenfrequencies $\{f_j\}$ and quality factors $\{Q_j\}$ under some experimental parameters $\vec{\mu}'$ after depositing a thin coating that modifies the mechanical response of the oscillator. The contribution of the coating and environment to the Q_j is proportional to dilution factors $\{D_j^{\mathrm{coating}}\}$ and $\{D_j^{\mathrm{env}}\}$, representing the fraction of the eigenmode's integrated strain-energy contained in the coating and environment (anything other than the Si and coating), respectively. For any particular eigenmode, the total mechanical loss of the system is due to the weighted sum of the diluted losses in each subsystem:

$$\frac{1}{Q_j(\vec{\mu}')} = (1 - D_j^{\mathrm{coating}} - D_j^{\mathrm{env}})\phi_{\mathrm{Si}}(\vec{\mu}') + D_j^{\mathrm{coating}}\phi_{\mathrm{coating}}(\vec{\mu}') + D_j^{\mathrm{env}}\phi_{\mathrm{env}}(\vec{\mu}'). \quad (6.1)$$

If we control the experimental parameters to remain nearly the same before and after coating deposition, we can estimate that

$$\begin{aligned} \phi_{\mathrm{Si}}(\vec{\mu}') &\approx \phi_{\mathrm{Si}}(\vec{\mu}) + \frac{\partial \phi_{\mathrm{Si}}}{\partial \vec{\mu}}\delta\vec{\mu} \\ \phi_{\mathrm{env}}(\vec{\mu}') &\approx \phi_{\mathrm{env}}(\vec{\mu}) + \frac{\partial \phi_{\mathrm{env}}}{\partial \vec{\mu}}\delta\vec{\mu}. \end{aligned} \quad (6.2)$$

We use a COMSOL finite element analysis to model the expected dilution factors for a given $\vec{\mu}$, which lets us solve for the coating loss in Eq 6.1.

Statistical Analysis

Frequentist statistical analysis is useful for posing questions of the type, "What is the probability $P(\vec{x}|\vec{\mu})$ of some experimental outcome $\vec{x}_0$ given an assumption that the true fiducial model parameters $\vec{\mu}_0$ lie inside the confidence interval $(\vec{\mu}_1, \vec{\mu}_2)$?" Physics defines the map P, while the canonical application of Neyman's method [125] due to Feldman and Cousins ensures a formally optimal choice of bounds $(\vec{\mu}_1, \vec{\mu}_2)$ that neither under- nor over- covers the parameter space given the observed measurement outcomes [126].

The parameters $\vec{\mu}$ include physically interesting but unconstrained quantities, such as ϕ_{coating}. They may also contain a set of nuisance parameters that are less interesting, but nonetheless affect the measurement outcome. Some nuisance parameters are selectable or controllable experimental parameters, such as the system temperature T and wafer geometry characterized by a radius r and thickness t. Some nuisance parameters may be constrained by other experiments but not perfectly known or easily varied, like the Young's modulus Y and coefficient of thermal expansion α of crystalline silicon and our thin film. Heuristically, we aim to design an experiment such that $P(\vec{x}|\vec{\mu})$ is mostly influenced by the parameters we wish to measure (ϕ_{coating}), rather than by our uncertainty about the nuisance parameters. Formally, we can construct $(\vec{\mu}_1, \vec{\mu}_2)$ for many simulated realizations of an experiment drawing from $P(\vec{x}|\vec{\mu})$ under a particular choice of nuisance parameters.

Achievable Constraints

It would be interesting to precisely measure the mechanical loss of the coatings, but we will be satisfied if we can constrain the coating loss to be below a particular value $\phi_{\text{threshold}}$. Fig. 6.1 shows the minimum coating loss that can be distinguished by the background of mechanical loss due to the silicon substrate and measurement apparatus. We can see that for larger dilution factors, we are able to detect smaller coating mechanical losses regardless of a fixed 25% uncertainty in dilution factor. However, note that the shaded regions reflect our uncertainty in the minimum detectable mechanical loss, not our projected uncertainty in our estimated coating mechanical loss.

6.2 Experimental Design

Gentle Nodal Suspension

We updated the Gentle Nodal Suspension (GeNS) system developed by [109] for cryogenic operation with an inverted cold plate. The primary benefit of this suspension system is excellent mechanical isolation from clamping losses that limit other common designs; the downside is inability to control sample temperature with high bandwidth due to weak thermal coupling.

The design used for measurements throughout this chapter is in Fig. 6.2. An updated design compatible with inverted or normal-orientation cold plates is in 6.3.

For the suspension point, we wanted a hard material that ideally is thermally conductive near 123 K. A sharper radius of curvature may slightly increase the surface area in contact with the sample, but also increases the maximum acceptable radial

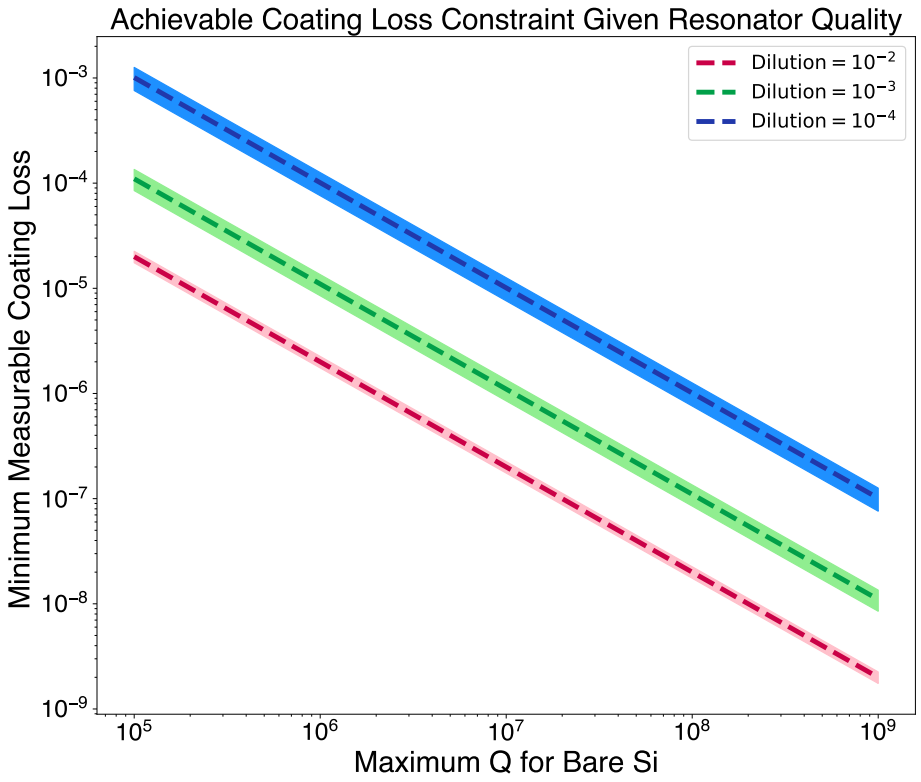

Figure 6.1: A larger dilution factor corresponds to more strain-energy contained in the coating, and improves the ability to distinguish the true coating mechanical loss from 0. The shaded regions correspond to 25% uncertainty in the true dilution factor.

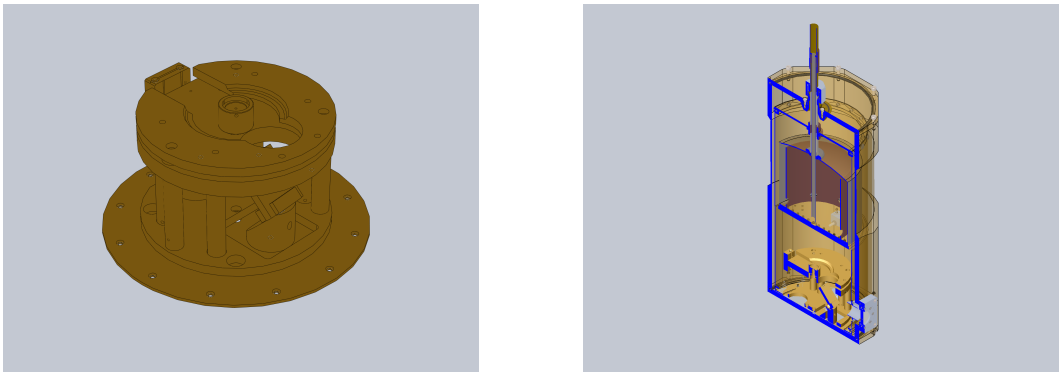

Figure 6.2: Solid model of Gentle Nodal Suspension system. The right view shows the suspension system inside the cryostat as used for the measurements presented in this chapter.

error for placing the disk on the sphere. We chose an uncoated sapphire plano convex lens with 200 mm focal length.

During pumpdown and cooldown, we rest the outer radius of the sample on an

aluminum ring with ramped edges to maintain the sample's position relative to the suspension point. The ring also increases thermal contact of the sample with a cold ($\approx 85K$) surface. After cooldown, the vacuum pump can be turned off to reduce vibrations. Then, we use a manual linear actuator mounted on the bottom of the cryostat to lower the holding ring and place the sample on the suspension point.

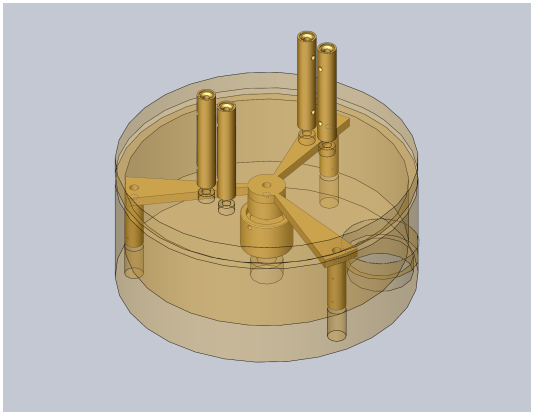

Figure 6.3: Solid model of next generation Gentle Nodal Suspension. Rather than lowering the disk onto a suspension point, the disk is clamped during pumpdown and cooldown then the clamp is released for measurements.

Optical lever sensor

We used a HeNe laser and QPD to measure the motion of silicon wafers with an optical lever. We want the beam spot position on the QPD to be maximally sensitive to angular displacement of the Si wafer, without saturating the range defined by the QPD radius.

We used an analytic ray tracing calculation (ABCD matrices) to optimize the position of a pair of telescoping lenses subject to the constraints on our optics table.

Temperature Sensing and Control

We instrumented the cryostat with Pt RTDs and read them out with 4-lead resistive measurements using a custom current driver and instrumentation amplifier. However, due to low thermal coupling of the sample to its environment, we need to independently estimate the sample temperature.

Maintaining a high Q mechanical system is incompatible with traditional temperature sensing based on strong thermally conductive coupling between a sample and a thermometer like an RTD. There are, however, a variety of remote or noncontact temperature sensing techniques [127] [128] [129] [130].

Silicon has a number of well-characterized temperature-dependent material properties, including dielectric function [131] and Young's modulus [132] [133] [134]. Likewise, some of the thin films under study have temperature dependent properties [135]. Following [136]'s work in crystalline Si, we took advantage of the temperature dependent Young's modulus of silicon to predict the temperature-dependent eigenfrequency of the Si wafer's acoustic modes.

During measurement, we continuously excite at least one eigenmode of the Si sample and track its eigenfrequency. We implemented both a phase-locked loop and zero crossing counter to track the eigenfrequency, but found the latter more robust and less expensive for our realtime model.

The change in Young's modulus causes a fractional change in the wafer's eigenfrequency. The eigenmode and eigenfrequency are set by the wafer geometry, but the change in eigenfrequency is only set by the change in material properties. We can achieve a similar measurement bandwidth for measuring any mode frequency up to the Nyquist frequency of our digital control system. Therefore, higher frequency eigenmodes typically provide better temperature sensitivity. We estimate that the sensitivity of a 30 kHz eigenmode near 123 K is 0.38 Hz/K.

We could reduce the systematic error of eigenfrequency-based temperature estimates by using the temperature dependence of many eigenmodes, and include the effect of the temperature dependence of additional material properties (especially Poisson's ratio). The analysis in Chapter 7 shows one way to implement this in post-processing.

However, even a single eigenfrequency is a sufficient sensor for realtime temperature sensing and control. Our ability to control wafer temperature is limited by actuation, not sensing. We apply heat by flowing current through a nichrome heating wire located above the wafer. However, Si has a low emissivity, so this is not a strong actuator. Modulating HeNe power can also change the ultimate disk temperature, but also creates temperature gradients across the wafer.

Vacuum and Cryogenics

We operated several liquid nitrogen cryostats from IR Labs. For electronic and mechanical design, we consulted the excellent reference by White [137].

Unfortunately, several features of the cryostat proved limiting for GeNS measurements. First, the cryostat's inverted cold plate complicated the process of loading and suspending samples. Without access from above the GeNS apparatus inside the cryostat, we needed to remove the entire apparatus each time we installed a Si

wafer. Rather than fixing the GeNS apparatus relative to the cold plate then closing the cryostat, our mechanical design fixed the sample relative to the cryostat's bottom lid and the entire experimental apparatus, sample, and lid were lifted to close the cryostat. This complicated the process of sample installation and optical lever alignment, and led to undue stress on the electromechanical connections requiring frequent maintenance.

Furthermore, the aluminum thermal shield was not in thermal contact with the liquid nitrogen reservoir by design. Instead, we needed to connect the cold plate to the thermal shield with thermally conductive copper straps. Because they were not part of the initial design, we had trouble fitting enough straps into the limited cryogenic volume to achieve good thermal coupling.

Finally, due to the low emissivity of Si, weak thermal coupling provided by GeNS, and absorptive heat load of the optical lever laser, the GeNS-suspended Si wafer temperature stabilizes well above ($\Delta T \approx 60K$) the temperature of the nodal suspension point.

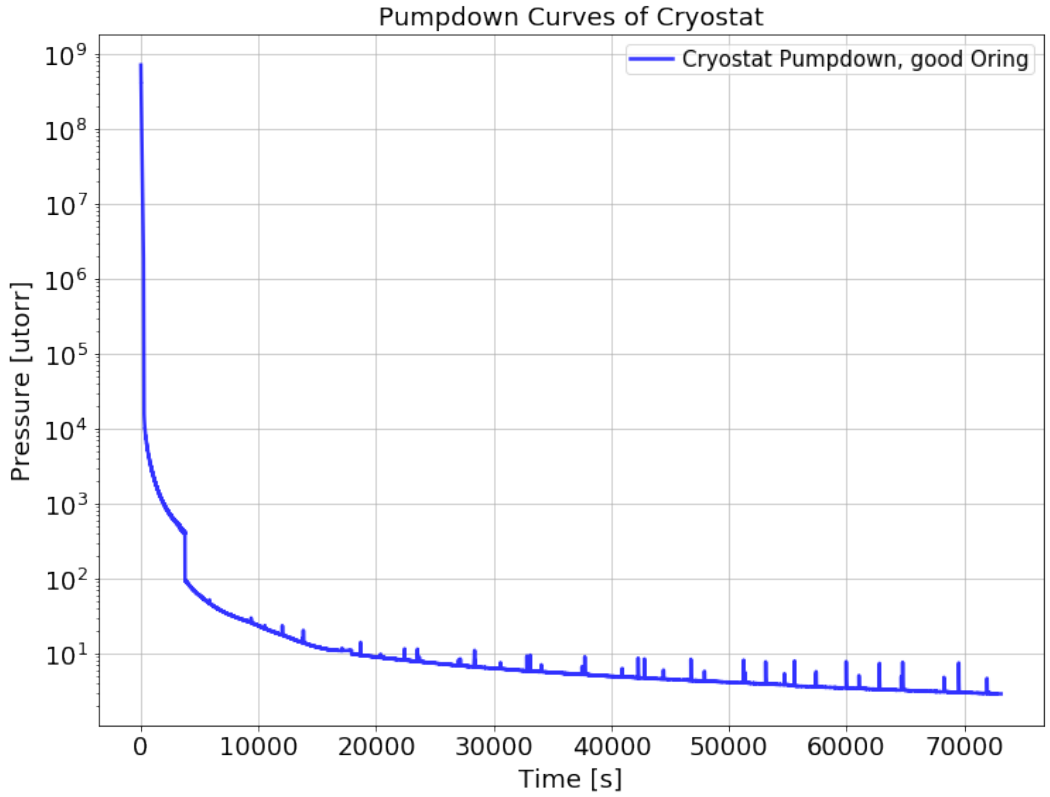

Figure 6.4: Pumpdown curve showing vacuum pressure inside cryostat containing GeNS experiment.

6.3 Measurements

Moderinger

We used a moderinger model ([19]) to make mechanical loss measurements. The measurement consists of exciting a particular eigenmode at a fixed amplitude using an amplitude locked loop. The loop unity gain frequency and excitation amplitude provides an estimate of the instantaneous Q of the excited eigenmode.

In Fig. 6.5, we compare measured quality factors of three eigenmodes of a 2" Si wafer held near 150 K over a couple hours.

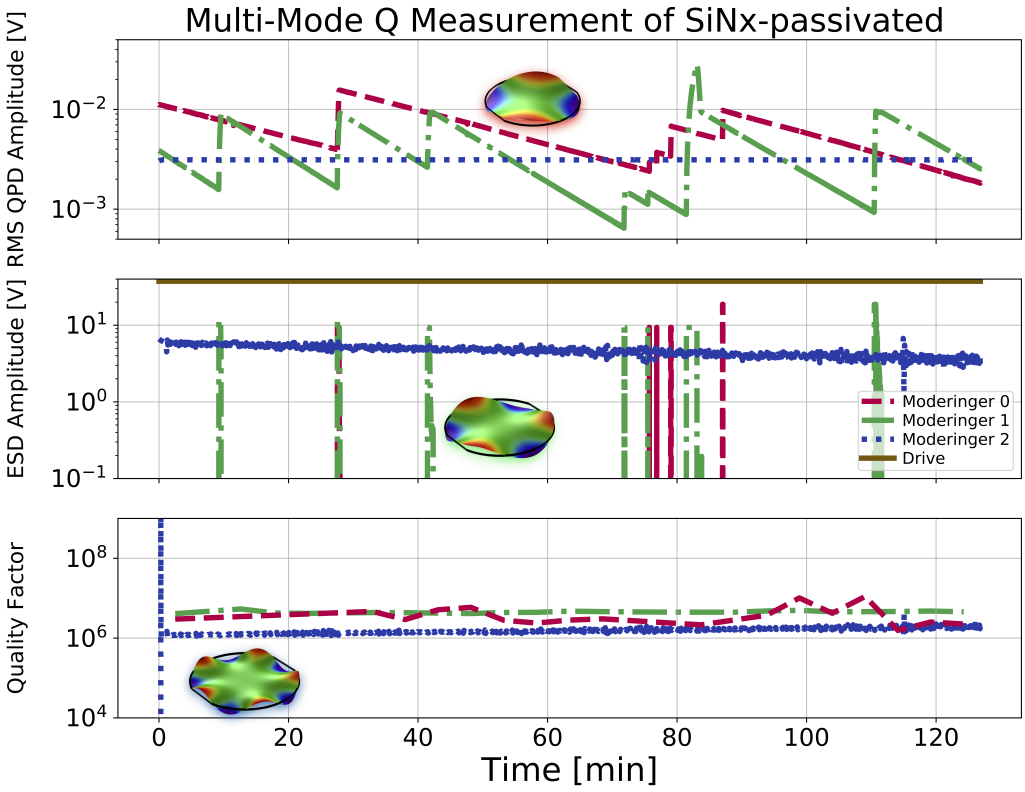

Figure 6.5: Comparison of measurements made with moderinger and traditional ringdown. From top to bottom, we show mode amplitude, mode excitation, and estimated quality factor over time. Eigenmode shapes calculated from COMSOL are displayed next to their respective traces. The quality factor for modes 0 and 1 are estimated with a rolling average of the decay rate, with these modes repeatedly excited for short durations when their amplitudes fell below a fixed value. The quality factor for mode 2 is estimated from the amplitude locked loop drive.

We made several temperature dependent mechanical loss measurements of Si wafers, shown in Fig. 6.6.

We also developed a loss budget analogous to [138], taking into account both temperature [139] and frequency- or geometry- dependent effects. The loss budget

and details on the physical interpretation of quality factor measurements are in Chapter 7. The quality factors in 6.6 are consistent with thermoelastic losses, as expected for measurements well above 123 K. Still, based on typical dilution factors $\approx 10^{-3}$ for thin films deposited on Si wafers, we expect to be able to constrain the mechanical loss of test films to $\approx 3 \times 10^{-6}$.

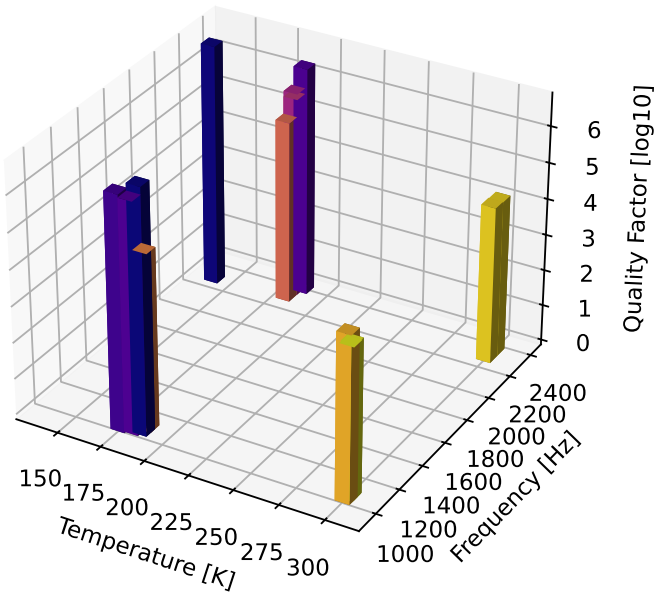

Figure 6.6: Collection of quality factor measurements made on similar 2" Si wafers with SiNx surface passivation.

6.4 Lessons for Future Work

Aside from cryogenic design, the more fundamental challenge in cryogenic mechanical loss measurements with gentle nodal suspension is maintaining a stable temperature throughout a quality factor measurement. As described in Fig. 7.1, the Si substrate experiences a sharp increase in thermoelastic loss away from Si's zero thermal expansion temperature. Measurements of time-varying mechanical loss are systematically biased towards the highest loss experienced in any sub-volume of the oscillator during the measurement time.

To achieve temperature control over the entire Si oscillator, we require tight thermal coupling of the oscillator to an actuator. However, this coupling must reflect low frequency acoustic waves that would spoil mechanical Q. The field of metamaterials

for structural and nanomechanical design offers promising examples for achieving this.

In brief, one could start by considering mechanical oscillators consisting of a cantilever clamped at one end or wafer clamped on the outer edge. Then, introduce exclusions to the substrate material to increase the effective cantilever length or wafer radius and decrease the fundamental eigenfrequency of the suspension. The higher frequency acoustic eigenmodes of the remaining material farthest from the clamp point are thus acoustically isolated from the clamp, but heat can still flow along the suspension. Designing the exclusions that the dominant coupling between exclusion layers is torsional (as in the double paddle oscillator) can provide further isolation.

A more clever approach explored by Abe [140] is to design a cantilever (or wafer) such that acoustic waves encounter several effectively independent mechanical oscillators before reaching an isolated oscillator. Each oscillator introduces a phase shift for acoustic waves near its resonance, so together they can act as a mechanical Bragg grating to enhance isolation in a particular frequency band.

One can also consider changing the geometry of the coating to enhance its coupling (and contribution to mechanical loss) for specific eigenmodes of the substrate. For example, if the coating is only deposited along lines of high stress for a 3rd order butterfly mode of the substrate, it will preferentially introduce loss to the 3rd order butterfly mode and less to other eigenmode. This can improve the ability to distinguish coating from substrate or environmental mechanical loss.

Chapter 7

LOSS TOMOGRAPHY

7.1 Statistical Inference for Mechanical Q Measurements

Purpose

We describe a general procedure to use Q measurements at various eigenfrequencies and temperatures (or arbitrary other experimentally controlled parameters), plus our knowledge of the physics of our system, to estimate key material parameters. For the testbed described in Chapter 6, the parameters of interest may be the mechanical loss, Young's modulus, and Poisson's ratio of a thin film deposited on a Si wafer. One may also be interested in distinguishing bulk and shear mechanical loss contributions [141] [142]. The purpose of this technique is to avoid the assumptions underlying the analysis in Chapter 6 and similar thin film loss measurements, which require the mechanical loss of the substrate to remain unchanged before and after the deposition process. A good review of Bayesian parameter estimation based on experimental results and an approximately linear model can be found in [143], and a more extensive reference including of MCMC methods is in [144].

Metropolis-Hastings Markov chain Monte Carlo

Our experiment measures a set of quality factors and eigenfrequencies for a mechanical system, which for concreteness could be a silicon wafer with thin film coating. As described in Chapter 6, our Q measurements are made at constant mode amplitude using a moderinger technique, and the eigenfrequency can be inferred from zero crossing counting or a phase-locked loop. We can measure the Qs and frequencies of N eigenmodes at a fixed temperature, then vary the system temperature to measure a new set of Qs and frequencies for those eigenmodes. If we measure the Qs at M different temperatures, our measurements are a set of $\{Q_{ij}, f_{ij}\}$ for $i \leq N$ and $j \leq M$. One could easily extend this problem. For example, one could search for amplitude-dependent effects by performing the measurements at various mode amplitudes, and simply include mode amplitude in the list of measurements. In any case, let us collect the experimental measurements in a vector $\vec{y}_0$. The measurement uncertainties are captured in a joint probability distribution $P_{\text{cov}}(\vec{y})$, which for the common case of Gaussian distributed uncertainties can be well represented with the measured covariance matrix $\mathbf{C}_{\vec{y}}$.

We believe that some set of unknown physical parameters determine our measurements $\vec{y}$. These include the Young's modulus and Poisson's ratio of the coating. Extrinsic sources of loss, for example from the surrounding air and clamping point, may be relevant. And if the experiment is well designed, the Qs are largely determined by the (generally anisotropic) mechanical losses in the Si wafer and coating. Collect all of the poorly constrained physical parameters in a vector $\vec{x}$, which has Q elements. Suppose we also have a probability distribution $P_{\text{prior}}(\vec{x})$ which describes our prior knowledge of the possible parameter values.

Finally, we describe below how to develop a physical model to predict mechanical Q measurement outcomes. The model may contain material properties tightly constrained by other experiments, such as the Young's modulus, Poisson's ratio, and coefficient of thermal expansion of crystalline Si. Let us collect the well constrained parameters in a vector $\vec{\mu}$, and keep in mind that if we decide later that we would like to constrain or account for uncertainty of some member of $\vec{\mu}$ we could move it to $\vec{x}$. For now, we simply define our physical model as a map

$$\mathbf{A}_{\vec{\mu}} : \mathbb{R}^{MN} \rightarrow \mathbb{R}^{Q}. \tag{7.1}$$

We want to solve for $\vec{x}$ (with some uncertainties) in the expression

$$\vec{y} = \mathbf{A}_{\vec{\mu}}(\vec{x}). \tag{7.2}$$

Because $\mathbf{A}_{\vec{\mu}}$ is some complicated nonlinear function, we cannot easily invert to solve for $\vec{x}$. However, Eq 7.2 and Bayes' theorem lets us write a convenient expression for the posterior probability distribution of the model parameters based on our measurements:

$$P_{\text{post}}(\vec{x}|\vec{y}) = \frac{P(\mathbb{A}_{\vec{\mu}}(\vec{x})|\vec{x})P_{\text{prior}}(\vec{x})}{P_{\text{cov}}(\mathbb{A}_{\vec{\mu}}(\vec{x}))}. \tag{7.3}$$

Since by construction all of our model uncertainty is captured in the uncertainty in $\vec{x}$, $P(\mathbb{A}_{\vec{\mu}}(\vec{x})|\vec{x}) = 1$. We can therefore use a MCMC algorithm such as Metropolis-Hastings to efficiently sample P_{post} simply by drawing sample values of $\vec{x}$ from ratio of the known distributions P_{prior} and P_{cov}.

7.2 Structural Mechanics Model

We developed a finite element analysis (FEA) model in COMSOL to analyze parameter-dependent mechanical properties of the wafer and coating.

Meshing Analysis

FEA models struggle to accurately represent systems with vastly different length scales along different dimensions, such as a large, wide wafer with several 10s cm diameter and 100s um thick whose mechanical properties depend strongly on a thin film only 10s or 100s nm thick. The model must balance the requirement to capture physics with a mesh that is finer than the smallest dimension against the computational cost of a mesh that spans the largest dimension. One effective strategy is reducing the model to a smaller subdomain that is related to the full domain by some symmetry (for example, meshing only 1/4 of a pie slice of a system with azimuthal symmetry reduces the number of elements by 4). One can also employ adaptive mesh refinement to start with a coarse mesh that is inexpensive to compute, then successively adding elements to create a finer mesh until the simulation results converge to a single value. Adaptive mesh refinement ensures the mesh is only as fine as necessary to achieve reliable results.

Eigenfrequency Analysis

Given the dimensions and material properties of a mechanical system, COMSOL's structural mechanics module can perform an eigenfrequency analysis to compute the mechanical eigenmodes and eigenfrequencies of the system.

Strain-energy density

According to Eq 6.1, the Q of a mechanical eigenmode depends on the sum of mechanical losses in each subdomain of the system, weighted by the fractional strain-energy density contained in that subdomain. COMSOL's eigenfrequency analysis provides a strain-energy density field defined at each mesh element, which we can integrate to obtain the fractional strain energy for each subdomain.

7.3 Loss Budget for a Si Wafer

The parameter estimation problem relies on having an accurate model for the frequency- and temperature-dependent mechanical losses present in the experiment. This section describes the physical mechanisms behind various mechanical losses that may limit Q measurements for the cryogenic Si Qs experiment described in 6.

Thermoelastic

For materials with finite thermal expansion, the strain profile of mechanical eigenmodes creates a spatially varying temperature distribution along which heat can flow. Eigenmode energy lost to such heat flow is called thermoelastic loss.

One reason silicon is an important material for mechanical sensing applications, including next generation gravitational wave interferometers, is that Si has zero thermal expansion at 123 K due to phonon anharmonicity [145].

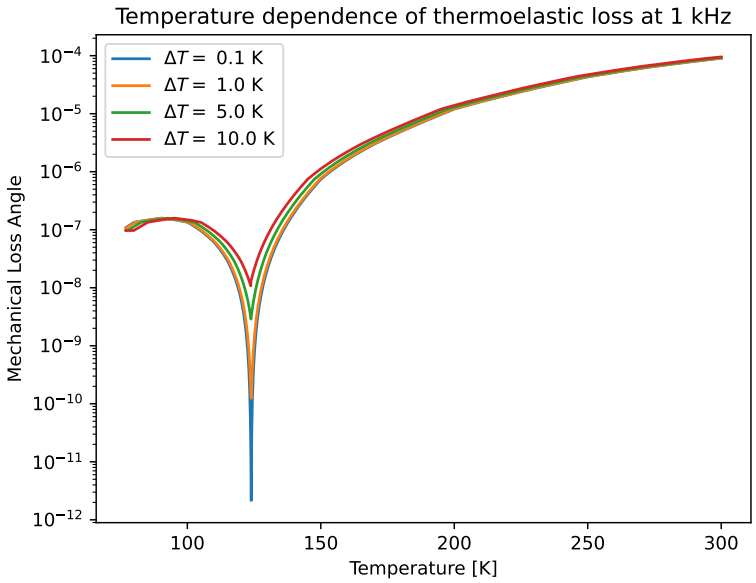

Figure 7.1: Mechanical loss at 1 kHz for a 2" silicon wafer due to thermoelastic damping, limited to the worst mechanical loss within ΔT K of the nominal system temperature. One can see that near 123 K where thermoelastic loss sharply decreases, temperature stability can limit the lowest achievable thermoelastic loss. However, ± 1 K is not a terribly stringent requirement.

Gas Damping

Stochastic collisions between the sample and the surrounding gas molecules can damp mechanical motion. There have been extensive studies on accurately modeling gas damping, but the static model developed in 1966 [146] has been widely applied to experiments with macroscopic oscillators.

Gas damping is typically the negative tradeoff when considering buffer gas-based cooling [147] [148] for sample or test mass thermal control.

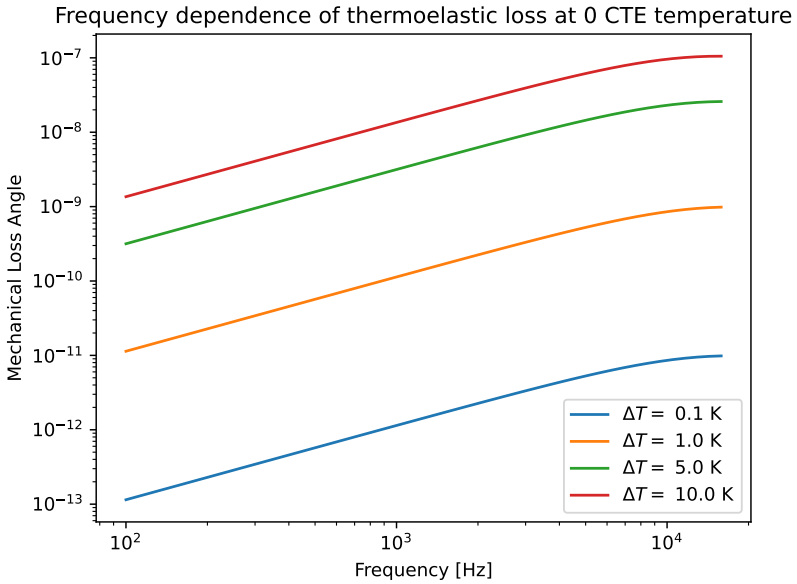

Figure 7.2: Frequency dependence of thermoelastic loss for a 2" silicon wafer with mean temperature near 123 K, at Si's coefficient of thermal expansion zero crossing. Thermoelastic loss is conservatively assumed to equal the maximum mechanical loss within ΔT of the nominal temperature.

$$\phi_{\text{gas}} = \left(\frac{2}{\pi}\right)^{2/3} \frac{1}{\rho h v_m} \sqrt{\frac{M_g}{RT}} P \approx \frac{P}{f\sqrt{T}} \tag{7.4}$$

Squeezed Film Damping

When two solid surfaces are separated by a thin layer of fluid, the fluid molecules can interact multiple times with each surface before fully thermalizing with the ambient fluid. This leads to a geometry-dependent enhancement of the ordinary gas damping effect given by [149]

$$\phi_{\text{squeezed}} = \phi_{\text{gas}} \frac{L}{16\pi d}. \tag{7.5}$$

Slide Film Damping

Another type of gas damping is slide film damping, which occurs between nearby surfaces due to lateral motion (rather than motion that changes the distance between the surfaces, as in squeezed film damping). We do not anticipate a significant contribution from slide film damping in our mechanical Q measurements, but the interested reader can learn more in [150].

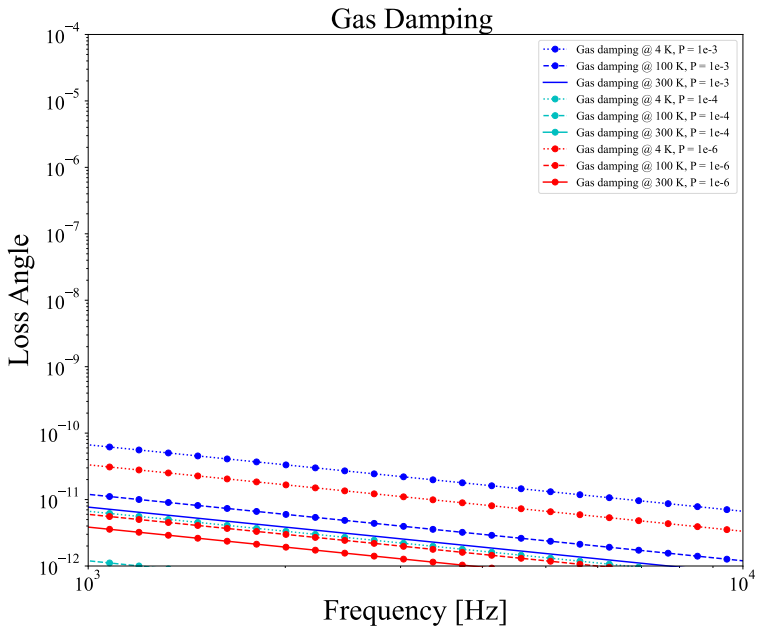

Figure 7.3: Mechanical loss for a 2” silicon resonator due to gas damping, shown at several ambient pressures and temperatures.

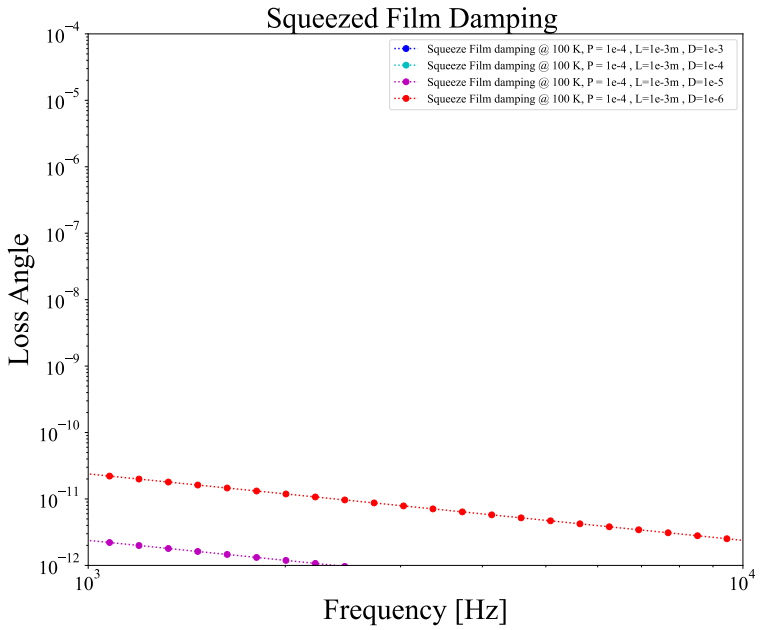

Figure 7.4: Mechanical loss for a 2” silicon resonator due to squeeze film damping, shown at several ambient pressures, temperatures, and overlapping surface area geometries.

Akhiezer Damping

Eigenmodes of a mechanical system are standing waves solutions of collections of phonons that carry the solid's stress energy. Due to the material's stress-strain relationship, the phonon density of states varies as the eigenmode evolves. When the equilibrium density of states varies relative to the instantaneous phonon distribution, phonons participating in the excited mode lose energy through phonon-phonon interactions as they rethermalize. When the mode frequency is comparable to the characteristic rate of thermal diffusion, phonon scatter leads to thermoelastic loss; when the mode frequency is much smaller than the thermal phonon decay rate, the dissipation is called Akhiezer damping; and the Landau-Rumer regime is relevant when the mode frequency is much larger than the thermal phonon decay rate [151].

Until recently, the mode- and direction-dependent picture was approximated with an average Gruneisen parameter γ_{avg}. Akhiezer damping on average leads to an upper limit on Q given by

$$Q \cdot f = \frac{\rho c^4}{2\pi\gamma_{\text{avg}}^2 \kappa T \tau} \tag{7.6}$$

where ρ is the material density, c is the speed of sound in the material, τ is the thermal relaxation time, and κ is the thermal conductivity.

Iyer and Candler [152] show how to compute the cross section for leading order phonon-phonon interactions due to a mode- and direction- dependent Gruneisen parameter $\gamma_{\text{i,j}}$. A more detailed derivation of Akhiezer and other loss mechanisms relevant to nanomechanical systems are in [151] [153].

Cubic crystals like Si can have anharmonicity in i of 39 phonon branches due to strain in j of 6 strain directions. In an orthonormal basis, there are only two independent anharmonicities

$$\vec{\gamma}_i \equiv \begin{pmatrix} \gamma_{i,1} \\ \gamma_{i,1} \\ \gamma_{i,1} \\ \gamma_{i,5} \\ \gamma_{i,5} \\ \gamma_{i,5} \end{pmatrix}. \tag{7.7}$$

The second order stress-strain relation for a cubic crystal can be written with just 3 elasticity coefficients as

$$\vec{\sigma} = \begin{pmatrix} c_{11} & c_{12} & c_{12} & 0 & 0 & 0 \\ c_{12} & c_{11} & c_{12} & 0 & 0 & 0 \\ c_{12} & c_{12} & c_{11} & 0 & 0 & 0 \\ 0 & 0 & 0 & c_{44} & 0 & 0 \\ 0 & 0 & 0 & 0 & c_{44} & 0 \\ 0 & 0 & 0 & 0 & 0 & c_{44} \end{pmatrix} \vec{\epsilon} \equiv C\vec{\epsilon}. \tag{7.8}$$

For a unit volume of the crystal experiencing stress tensor $\vec{\epsilon}$, the effective, cycle-averaged elastic storage modulus is

$$E_{\text{eff}}(\vec{\epsilon}) = \frac{\vec{\epsilon}^{\top}\vec{\epsilon}}{\vec{\epsilon}^{\top}C^{-1}\vec{\epsilon}}. \tag{7.9}$$

The full mode- and direction- dependent mechanical loss is expressed in [152] as:

$$Q = \frac{E_{\text{eff}}}{\Gamma_a^2 C_v T} \frac{1+\Omega^2\tau^2}{\Omega\tau}. \tag{7.10}$$

The strain-energy loss depends on the degree to which the applied strain perturbs the eigenfrequency of each phonon branch [153]

$$\delta\omega_i = -\omega_{i,0}\vec{\gamma}_i\vec{\epsilon}. \tag{7.11}$$

This leads to the anharmonic Gruneisen parameter Γ_a depending on the variance of the strain energy-weighted $\vec{\gamma}_i$.

Mason shows how to calculate Gruneisen parameters $\gamma_{i,1}$ and $\gamma_{i,5}$ for Si using measured third-order strain moduli in [154]. He shows that $\gamma_{i,1}$ varies between -0.83 and 1.43 with an average value of 0.501, while $\gamma_{i,5}$ varies between -0.92 and 0.92 with an average value of 0 (shear modes are isovolumetric). There are only 21 unique values of $\gamma_{i,1}$ and $\gamma_{i,5}$.

Akhiezer damping has been observed in Si [155]. However, Akhiezer damping has not yet been definitively demonstrated near acoustic frequencies ($\approx$ kHz) in Si resonators near 123 K.

It does not appear that anything inherently prevents an appropriate choice of mode shape from sending $Q_{\text{phonon-phonon}} \rightarrow \infty$, such that mechanical loss would be set by fourth order phonon interactions. Of course, the condition would need to hold across the entire volume of the oscillator.

Total Loss Budget

The mechanical loss budget in Fig. 7.5 captures the total loss due to dissipation for a 1 kHz eigenmode of a 2" Si wafer held at 123 K. To fully describe experimental mechanical losses, we would also need to include clamping losses, which depend on the curvature of the mechanical eigenmode near the suspension point [138].

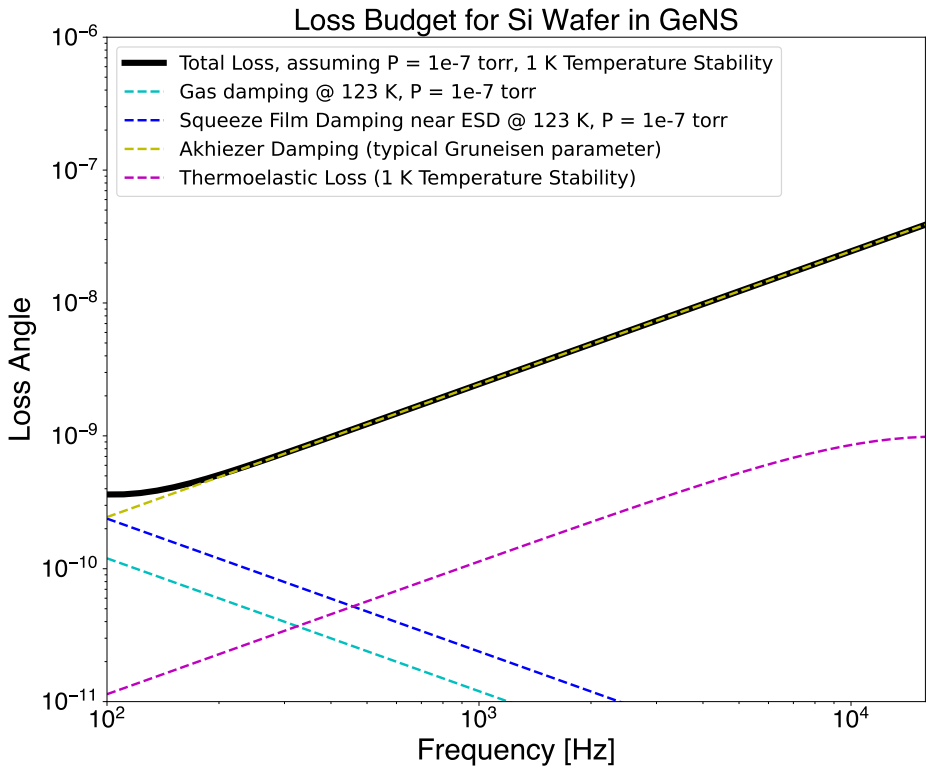

Figure 7.5: Mechanical loss budget for a bare Si wafer with 2" diameter, held at 123 ± 1 K and mechanically isolated from the environment with a gentle nodal suspension.

7.4 Demonstration with Simulated Data

For technical experimental reasons, we do not have sufficient data to perform the tomography analysis in a temperature-dependent Si system as envisioned. Moreover, our COMSOL model is computationally expensive and the limiting step of the

MCMC analysis. Other groups have demonstrated with cryogenic Si Q measurements and fast FEA that neither challenge is a fundamental barrier to performing loss tomography on temperature dependent Si-and-film Q measurements. We hope this demonstration encourages others to perform similar analyses, and proves useful for characterizing material properties of Si and thin films.

Generating data

We will analyze a system with some assumed "true" properties, generate some noisy data based on those nominal properties, and show that we can infer certain material properties when the data follow the model.

We assume the system and material properties in Table 7.1. Uncertainties are for the assumed prior distribution, and are the standard deviation of a Gaussian centered on the nominal value and uncorrelated with the other parameters. Parameters included in the parameter estimation problem were randomly assigned "true" values drawn from a uniform distribution within 10% of one standard deviation of their nominal values. Estimated measurement temperatures were constrained with a uniform prior between $100K$ and $200K$. The only parameter not explicitly assigned a prior distribution was the coating loss angle ϕ_{coat}, which instead had an unbounded log-uniform prior. Material properties were chosen to be similar to a (100) single crystal Si wafer with an amorphous Si coating.

For the true parameter values and each set of values proposed by the MCMC, we use an analytical model [156] and code [157] developed by Vajente to compute to compute the eigenfrequencies of a coated and uncoated disk. We use change in eigenfrequency and total mass with and without coating to estimate the coating dilution factor, as proposed in [158] and proven with some conditions in [156].

$$D_i = 1 - \left(\frac{f_i^{(\text{uncoated})}}{f_i^{(\text{coated})}}\right)^2 \frac{m^{(\text{uncoated})}}{m^{(\text{coated})}} \tag{7.12}$$

We then compute each eigenmode's quality factor as the sum of thermoelastic and Akhiezer contributions in the Si substrate, plus a frequency and temperature independent contribution from ϕ_{coat} in the coating. For a given set of proposed parameter values, we limit ourselves to the first 34 eigenfrequencies below 16 kHz at each of the 7 measurement temperatures.

For the "true" parameter values in Table 7.1, we generate some experimental data by adding noise to the fiducial eigenfrequencies and quality factors. We add a uniformly

Symbol	Description	Nominal Value	True Value	Reference
$R_{s,0}$	Si Radius at T_{ref}	75 mm	–	–
$h_{s,0}$	Substrate Thickness at T_{ref}	500 ± 50 μm	502.5 um	–
$Y_s(T)$	Si Young's modulus	$Y_s(T_{ref})$ = 166 GPa	–	[132] [134]
ν_s	Si Poisson's ratio	0.167	–	–
ρ_s	Si density at T_{ref}	22220 kg/m^3	–	[137]
t_{coat}	Coating Thickness	300 ± 75 nm	299.0 nm	–
Y_{coat}	Coating Young's Modulus	80 ± 20 GPa	81.3 GPa	–
ν_{coat}	Coating Poisson's ratio	0.22 ± 0.055	0.228	–
ρ_{coat}	Coating density	2175 kg/m^3	–	–
$\gamma_{0,s}$	Si Gruneissen parameter	0.4 ± 0.2	0.395	–
ϕ_{coat}	Coating loss angle	–	10^{-4}	–
T_1, T_2, T_3, T_4, T_5, T_6	Measurement temperatures	–	110, 120, 123, 123.9, 125, 130, 150 K	–

Table 7.1: Parameters for loss tomography demonstration. For parameters inferred in the analysis presented in Fig. 7.6, "Nominal Value" refers to the mean of the Gaussian-distributed prior distributions, while "True Value" refers to the underlying parameter value used to generate simulated experimental data.

random offset drawn from $[-1, 1]$ Hz to each eigenfrequency, and multiply each quality factor by a uniformly random factor drawn from [0.99, 1.01].

Finally, we define a likelihood function proportional to the joint probability density for Gaussian uncorrelated errors centered on each of the experimental data points. For eigenfrequencies, we assume a 1 Hz standard deviation, and for quality factors we assume a 1% standard deviation. The objective function for the MCMC is the sum of the log likelihood and log prior.

Results

We performed the MCMC sampling using the python emcee module.

With 10,000 iterations of an ensemble of 512 samplers, the autocorrelation time of the ensemble was only about 10x less than the number of iterations, and not enough to ensure unbiased sampling of the true probability distribution. Nonetheless, the results in Fig. 7.6 suggest the MCMC would be able to constrain $\phi_{coating}$ given enough iterations.

Several interesting features suggest modifications to improve the analysis. The bimodal distribution of T_4, the temperature closest to the zero crossing of Si's

thermal expansion coefficient, suggests thermoelastic loss and not eigenfrequency is constraining the temperature estimates. It would be interesting to perform this analysis to higher eigenfrequencies that would be more sensitive to temperature changes. We could also include a measurement at a known temperature (like room temperature) as a calibration point.

Due to the expensive computation of many eigenfrequencies, the likelihood took seconds to compute. It would be preferable to first perform the expensive computation over a grid or sampling around the expected parameter values, then perform a polynomial fit to create a fast, if approximate, objective function. To improve model fidelity, one could instead compute eigenfrequencies and dilution factors with a numerical finite element analysis and then fit a polynomial model. Unless a finite element model could be developed to run in 10s or 100s ms, it is unlikely to be useful for directly computing eigenfrequencies during the MCMC. One could also search for a sampling algorithm better suited for our problem, which may more efficiently sample the parameter space with shorter autocorrelation.

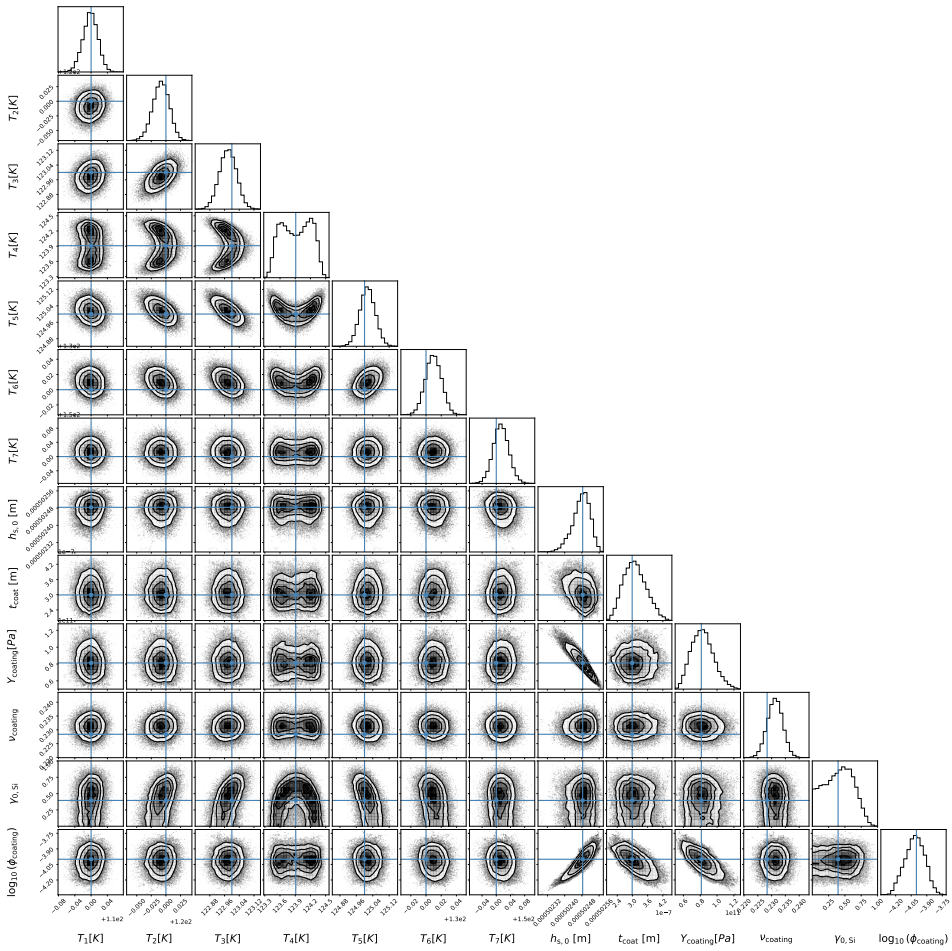

Figure 7.6: Corner plots showing the joint posterior probability distributions of the model parameters.

Part III

A Phase-Sensitive Optomechanical Amplifier

Prototyping a preamplifier for optical readout loss mitigation

Chapter 8

EXPERIMENTAL LAYOUT AND DESIGN

We designed and built an initial demonstration towards the phase-sensitive optomechanical amplifier described in Chapter 3 from the ground up. The purpose is to work through the important challenges that would need to be resolved before applying PSOMA to a Voyager-like interferometer, including controls, cryogenics, optical design, and mechanical design.

8.1 Vacuum System

The core optics of the PSOMA experiment must be under vacuum to avoid acoustic noise coupling from the environment and maintain clean optics of the high finesse cavity. The radius of the chamber was chosen to accommodate a breadboard containing all core optics, and two layers of radiative shielding for cryogenic operation. The height was chosen to allow for potential future installation of seismic isolation systems. The chamber has four DN125CF flanges for optical feedthrough and thermal feedthrough from a cryogenic cooler. There are also four DN35CF flanges for electrical feedthrough and vacuum pumping. A hinged lid allows a single user easy access to the chamber interior without the use of a hoist. With no installed equipment, the vacuum chamber was capable of reaching below 10^{-7} torr.

The vacuum system layout (8.2) is designed such that the chamber can be vented with clean, dry compressed nitrogen gas. Venting with N_2 reduces the amount of water adsorbed onto metal surfaces while vented, which significantly reduces pumpdown time.

8.2 Mechanics

Mirror Mounts

Most of the kinematic mirror mounts are U100 models from Newport optics. To allow alignment and beam clearance of the Mach-Zehnder optics, the input and output beamsplitter and MC1 are in Newport 9774 top-adjusting mounts. All mounts are on 3/4” diameter posts to set a 4” beam height.

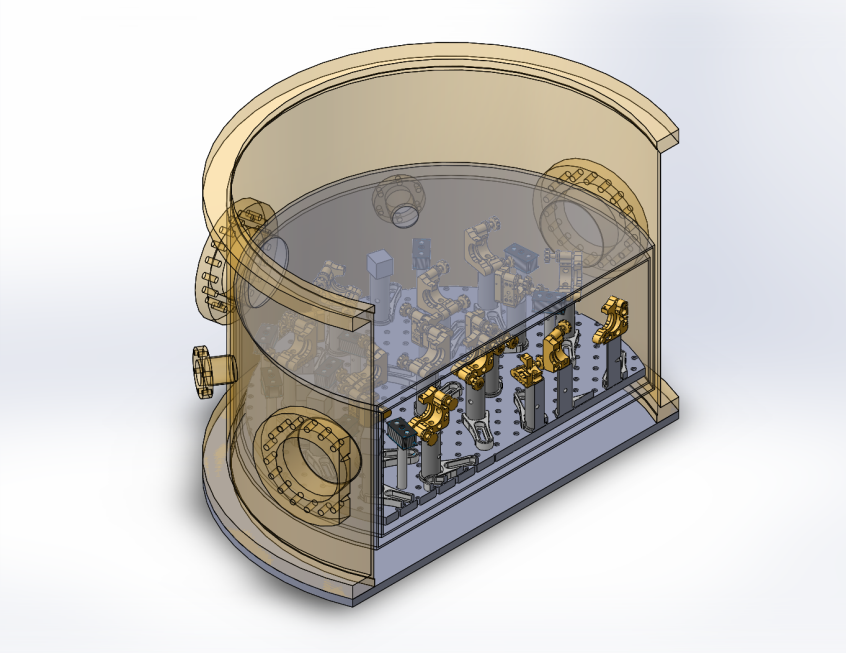

Figure 8.1: PSOMA vacuum chamber showing breadboard and fit-check of optics for DRPSOMA configuration.

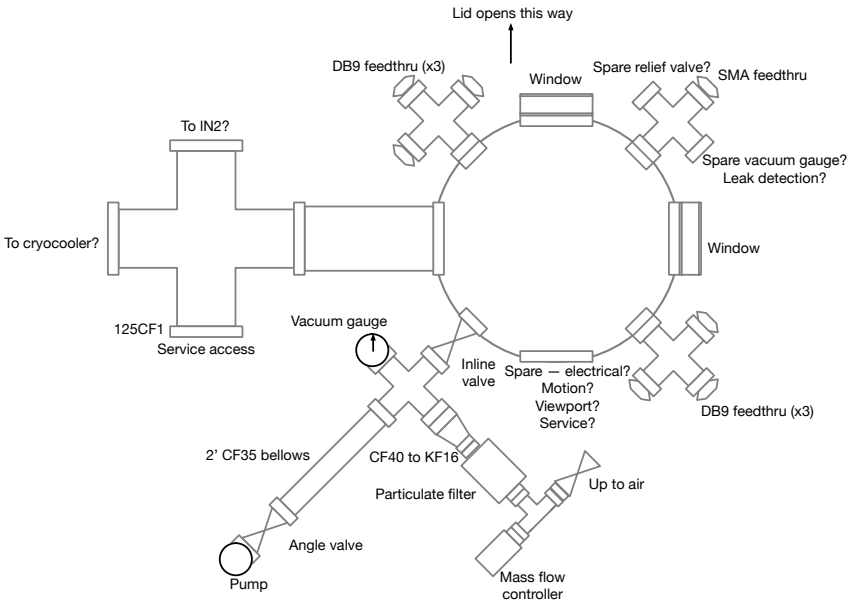

Figure 8.2: Vacuum layout as designed. Not all DB9 electrical feedthroughs are necessary or installed at this stage of experiment. The 4-way cross providing cryocooler access is also not yet installed.

Breadboard

The in-vacuum breadboard is 1/2" thick unadonized aluminum with 1" hole spacing. The breadboard is rigidly clamped to 3/4" diameter posts, and the posts are

fork clamped to the bottom of the vacuum chamber. Future iterations of the experiment can avoid stress-induced misalignment during pumpdown by kinematically mounting the breadboard to the chamber.

8.3 Optics

The latest version of the optical layout for our experiment is in Fig. 8.3

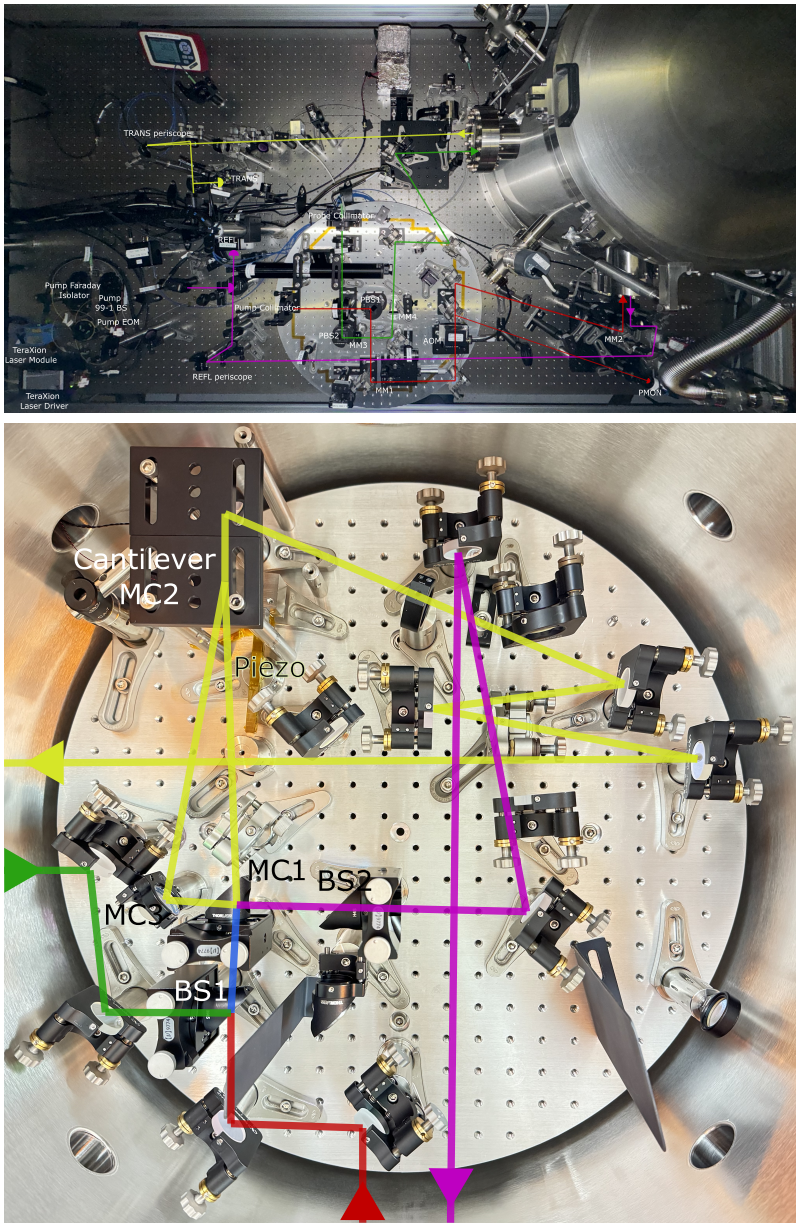

Figure 8.3: Optical layout for single-cavity optomechanical amplifier demonstration. For a more conceptual diagram, see 9.6.

Lasers

The amplifier is pumped by a single laser on-resonance with PSOMA's ring cavities. We also phase-lock an auxiliary probe laser to the pump to characterize the system's transfer functions and understand the challenges of adapting PSOMA to work with an existing optomechanical sensor with its own frequency reference.

For the PSOMA pump, we use a PureSpectrum Narrow Linewidth Laser from TeraXion. This 1550 nm, 80 mW semiconductor laser uses a laser driver module to lock the laser frequency to an integrated fiber Bragg grating, achieving narrower linewidth and single mode operation over its full temperature range. Fast analog modulation is achieved by driving the error point of the module's internal feedback loop.

The probe laser is a planar external cavity laser from Rio Laser. The AR surface of an InP gain chip is coupled to the AR surface of a planar Bragg grating on a silica-on-silicon planar lightwave circuit [159].

Mirrors

Most of the mirrors are off-the-shelf high reflectors or beamsplitters from Thorlabs or Newport. However, the cavity mirrors must be superpolished, wedged optics with low optical loss high-reflecting and anti-reflecting coatings.

Because our amplified signal will be imprinted on the phase of light reflected from the ring cavities and is proportional to circulating optical power, we want the cavity to be overcoupled. To reduce astigmatism in the cavity, we should choose a low angle of incidence for the cavity's curved mirror. And, using a flat mirror as the cavity's input coupler simplifies mode matching in the Mach-Zehnder interferometer.

Based on these constraints, we want to choose MC1 to be the superpolished flat mirror with the highest transmissivity at 45°. For ease of alignment, MC2 should be a curved mirror mounted on the Si cantilever. And MC3 should be the superpolished mirror with the lowest transmissivity near 45°.

We used the apparatus in Fig. 8.4 to measure the transmissivity of several superpolished optics we had on hand. The test laser was passed through three polarizing beamsplitters to reject all p-polarized light. A two-frequency chopping wheel was used to perform separate lock-in measurements of the reference and test beams to reduce photodiode electronics noise.

To reject laser intensity noise, each measurement on the "Transmission" photodiode

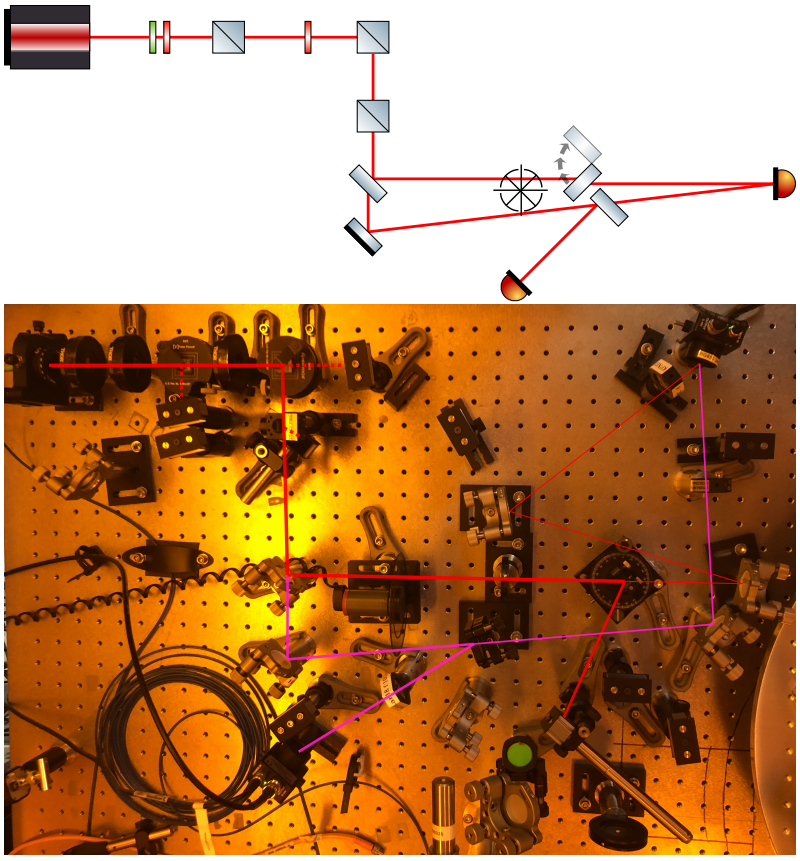

Figure 8.4: Optical layout for mirror transmissivity measurement

was calibrated against a “Reference” photodiode that monitored a fixed fraction of the total laser power and maintained a fixed gain throughout the measurement. Due to the extremely low transmissivity of the optics, the difference in laser power with and without the test optic in the beam path could exceed the dynamic range of the “Transmission” photodiode. Therefore, an additional pickoff beam was aligned onto the “Transmission” photodiode to calibrate the photodiode gain when it was changed.

The test optic was mounted in a flip mount to easily add and remove it from the beam path, as well as a rotating kinematic mount to change the test beam’s angle of incidence on the optic. To ensure the beam was entirely on the photodiode with or without any deflection due to the test optic, we placed a sharp lens just before the transmission photodiode. And, to avoid interference at the transmission PD, either the reference or test beam is blocked during each measurement (and we assume the photodiode gain is constant for a giving gain setting).

Each transmissivity measurement requires, for each of three optical configurations,

simultaneous lock-in measurements of the transmission and reference photodiode signals:

1. Test optic out of path, test beam incident on transmission PD
   ($K_P \equiv P_{\mathrm{TRANS}}(f_{\mathrm{test}})/P_{\mathrm{REF}}(f_{\mathrm{ref}})$)
2. Reference beam incident on transmission PD
   ($K_G \equiv P_{\mathrm{TRANS}}(f_{\mathrm{ref}})/P_{\mathrm{REF}}(f_{\mathrm{ref}})$)
3. Test optic in path, test beam incident on transmission PD
   ($X \equiv P_{\mathrm{TRANS}}(f_{\mathrm{test}})/P_{\mathrm{REF}}(f_{\mathrm{ref}})$).

In practice, configuration (1) is used to calibrate the fraction of laser power incident on the reference PD, and need only be performed once. Configuration (2) is used to calibrate transmission PD gain, and need only be performed once per gain setting. For example, with the test mirror in the beam path the test PD gain may be at G_1, while with the test mirror out of the beam path the test PD gain may be at G_2. Configuration (3) is the actual measurement of transmitted power, and can be repeated at several angles of incidence for each optic.

The mirror transmissivity at a particular angle of incidence is then:

$$T(\theta_{\mathrm{aoi}}) = \frac{X/K_{G_1}}{K_P/K_{G_2}}. \tag{8.1}$$

Fig. 8.5 shows the results for the two mirrors used in our cavity. We also measured 168 ppm transmissivity near 0° on a 1/2" Si mirror with 0.5 m radius of curvature, which we use as MC2.

Future iterations of PSOMA involving two ring cavities on either side of a Mach-Zehnder interferometer will require new custom coating runs to achieve nearly identical parameters for both cavities. The mirror transmissivities, curvatures, and coating design should be optimized to minimize projected amplifier noise at that time.

Fiber Components

The lasers used in PSOMA are fiber-coupled. We also chose to use a fiber-based electro-optic modulators (EOM), which offer a wider modulation bandwidth and lower required operating voltage for a given modulation depth relative to typical free-space EOMs due to the small mode volume inside the nonlinear crystal. The

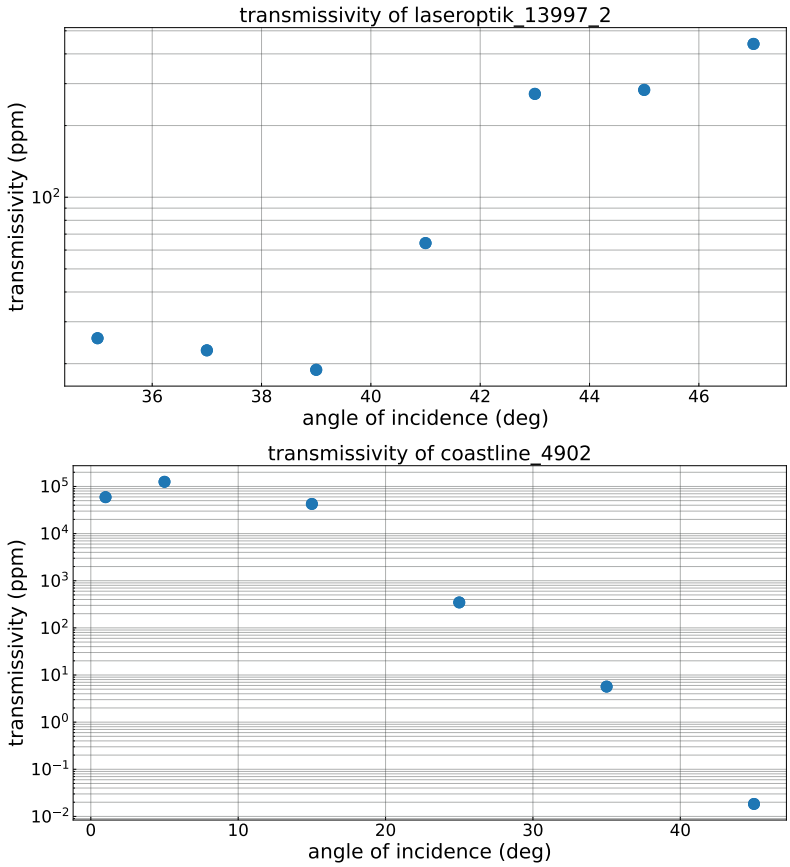

Figure 8.5: Transmissivity of cavity mirrors (top is MC1, bottom MC2) as a function of incident angle. Top is MC1, a mirror from Laseroptik. Bottom is MC2, a mirror from Coastline.

MPX-LN-0.1 EOMs from iXBlue Photonics uses a $LiNbO_3$ waveguide and has a usable bandwidth of 300 MHz with typical V_π at 50 kHz of 3.5 V [160]. We also used fiber-coupled Faraday isolators (IO-G-1550-APC from Thorlabs) and several fiber-coupled beamsplitters (PN1550R1A1, PN1550R2A1 and PN1550R5A2 from Thorlabs).

The ease of alignment and compact size of fiber optic components come with tradeoffs in polarization selectivity, acoustic noise coupling, and optical loss. To mitigate these effects, we secure all optical fibers to the breadboard to stiffen each length of optical fiber and prevent acoustic coupling. We also clean the fiber tips with commercial fiber cleaning tissue and solution to minimize excess optical loss or scatter at fiber interfaces. The measured loss in fiber components from our pump diode to launch is ≈ -3.8dB, close to the sum of nominal losses for the components in series. Using fibers with angled APC connectors reduces backreflection of light at fiber interfaces.

Still, fiber components introduce noise or undesired cross-coupling through several routes:

- Environmental acoustic noise stresses optical fiber, which can directly change the optical propagation length of the fiber and introduce phase noise in the launched laser beam.
- The EOM's waveguide is designed for TE mode propagation. Misalignment of the laser entering the waveguide leads to excess loss for the laser's TM component.
- Acoustic noise-induced stress of the optical fiber also induces polarization noise in the propagating light. This allows acoustic noise to generate polarization noise, which becomes laser amplitude noise when the laser passes through components with polarization-dependent losses including most fiber components and the free-space PBS.
- Due to the birefringence of the EOM's crystal, the drive voltage applied across the crystal generates not only phase modulation but also polarization modulation of the laser. Since the laser typically passes through additional fiber and free space components with polarization dependent losses after the EOM, the laser acquires an amplitude modulation at the drive frequency.

The final effect is especially pernicious when RF control sidebands used for example to stabilize the laser frequency to the optical cavity with Pound-Drever-Hall locking are applied at the fiber EOM. Any AM component of the PDH sidebands generate an offset on the PDH error signal and allows first order coupling of amplitude noise (including due to temperature drift of the EOM itself) into the laser frequency stability [161] [162]. PM-to-AM coupling due to EOM birefringence can be actively nulled by applying a DC offset to the EOM control voltage [163] [164].

8.4 Cavity Geometry

We designed PSOMA with a triangular (three mirror) cavity geometry. Triangular cavities have nondegenerate s- and p-polarized eigenmodes, which reduces resonance of the undesired polarization mode. We also placed the single cavity curved mirror at MC2 to reduce the effect of astigmatism at the 45°incidence optics and simplify mode matching in the Mach-Zehnder interferometer. To determine the optimal cavity geometry under the constraint that MC1 have a 45°angle of incidence,

we simulated the higher order transverse electromagnetic (TEM) mode spectrum of the ring cavity in Finesse 2. We minimized coresonance of higher order TEM modes and RF sidebands due to PDH modulation at 33.6 MHz. The simulated transmission spectrum for the optimal cavity geometry is in Fig. 8.6.

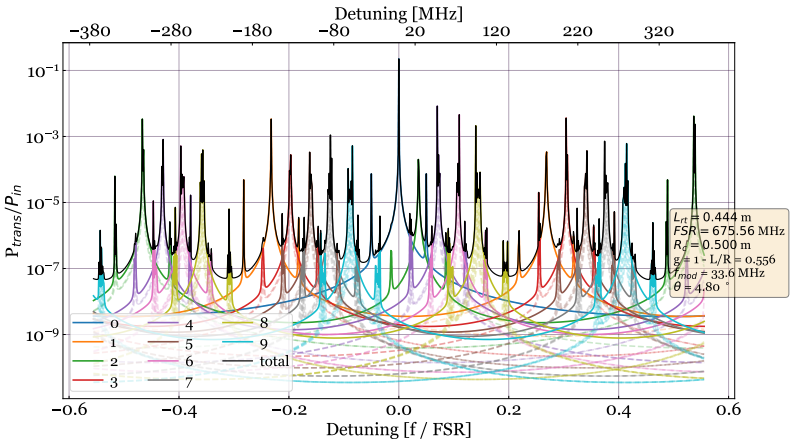

Figure 8.6: Transmissivity of low order Hermite-Gaussian cavity modes from Finesse 2 calculation.

8.5 Mode Matching

We measured the transverse beam profile of the pump and probe lasers from the fiber-to-free space collimators using a Data Ray Beam'R2 profiler.

Then, we used the open source mode matching and beam profiling software "a la mode" to select a pair of lenses to match the beam waist and position to the cavity's fundamental mode that minimizes mode mismatch error due to lens position error.

Experimental methods for optimizing mode matching are discussed in [165].

8.6 Electronics

Photodiodes

All photodiodes had InGaAs sensors with about 1 A/W responsivity at 1550 nm.

Where we only needed to measure signals at acoustic or lower frequencies, we used the gain-adjustable PDA20CS from Thorlabs. For higher frequencies, we used a Newport 1611 or 1811 receiver.

All photodiodes are mounted on electrically insulating Teflon bases to prevent ground loops and coupling of noise between the optical table and low noise transimpedance amplifiers of the photodiodes.

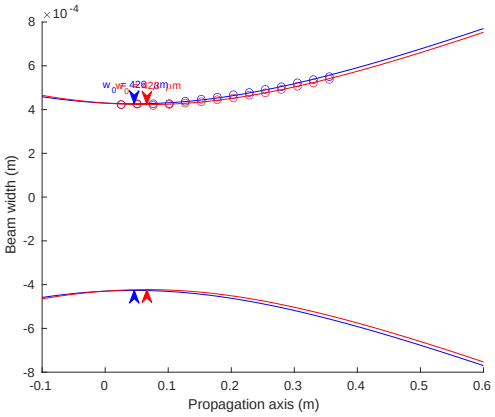

Figure 8.7: Beam profile of probe laser showing good agreement (ellipticity close to 1) along two transverse axes.

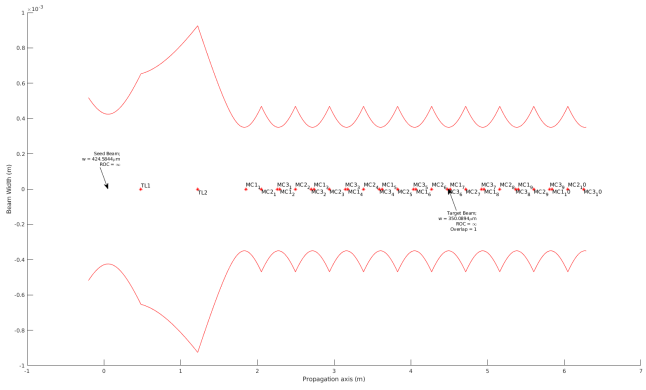

Figure 8.8: Mode matching lens placement solution for the pump laser generated by geometrical optics calculation in a la mode.

Note that fiber and free space photodiodes can have slight different responsivities, as shown in Fig. 8.9.

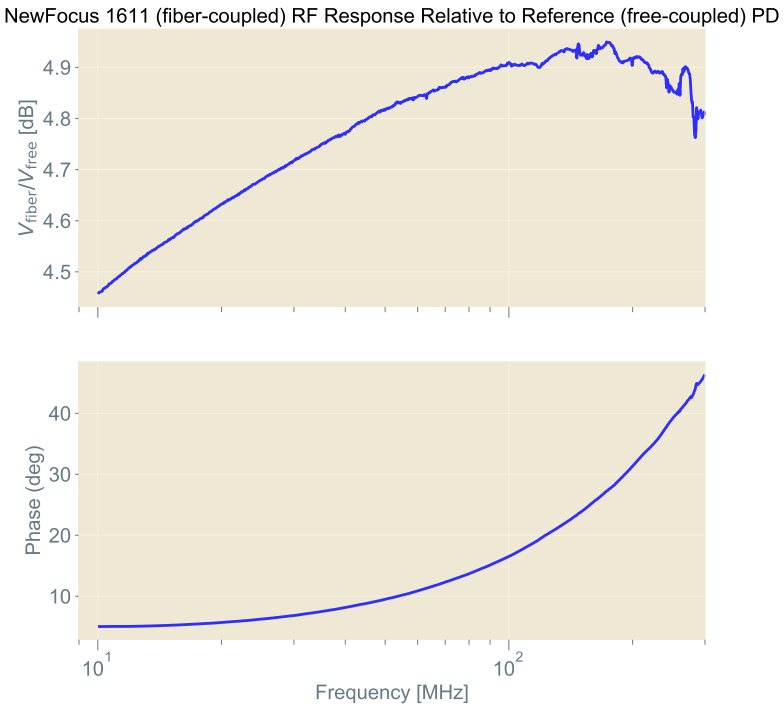

Figure 8.9: Relative responsivity of fiber coupled and free space NewFocus 1611 photodiodes. The time delay is due to an optical path length difference in the experimental setup, so the magnitude is the main result of interest.

Moku

We used the FPGA-based Moku:Pro from Liquid Instruments in a variety of test applications, for example as a network analyzer, spectrum analyzer, digital synthesizer, or RF phase sensor.

We also used Moku:Pro as the controller for our fast (up to 150 kHz bandwidth) feedback loops, including for demodulation and filtering.

Laser Drivers

The temperature and current of the TeraXion laser are controlled by a proprietary laser driver.

The Rio laser temperature is controlled by a commercial controller from Thorlabs, such as ITC502. Rio laser current is controlled by a low noise current driver described in [166].

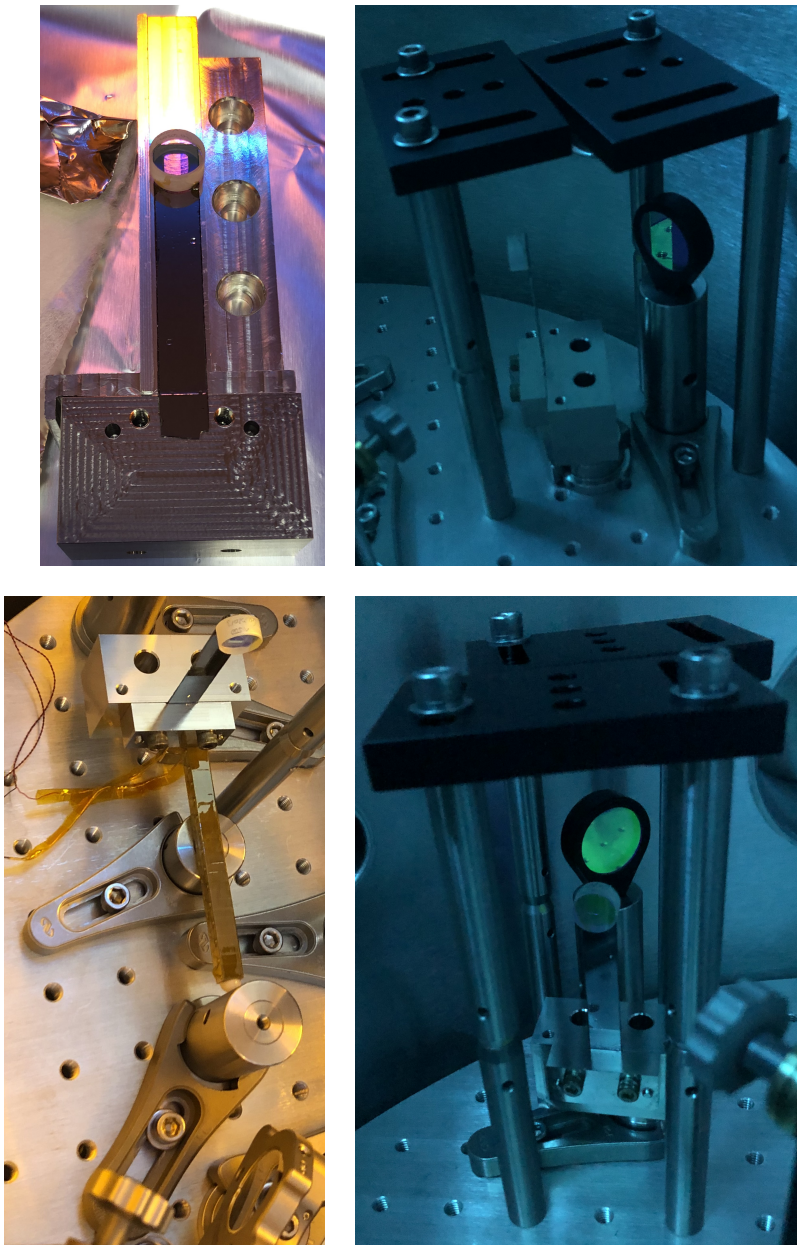

Figure 8.10: Photos of PSOMA cantilever. From top left clockwise: Cantilever in jig before being clamped; cantilever mounted at MC2 viewed from side; cantilever mounted at MC2 viewed from front (HR surface); piezoelectric actuator clamped against cantilever mount.

Chapter 9

CONTROL SYSTEM

Figure 9.6 shows the conceptual optical layout of our amplifier demonstration, and the control system discussed in the text. This chapter describes the critical sensors, actuators, and controllers for operating the amplifier in its current configuration. We also discuss a scheme for reducing input-referred pump frequency noise by controlling Mach-Zehnder length.

9.1 Sensors

Photodiodes for Relative Intensity Sensing

The DC-coupled port of a photodiode monitors intensity fluctuations of the total field incident on the diode. Though we can get a rough sense of pump and probe laser powers with photodiodes, to reduce calibration error we typically compare relative intensity fluctuations on these monitors.

For example, the cavity transmission photodiode (TRANS) is a good sensor for relative intensity fluctuations of the cavity's circulating field. The photodiode monitoring pump pickoff (PMON) just before the vacuum chamber senses relative intensity fluctuations of the pump laser. The cavity reflection photodiode (REFL) monitors the sum of pump and probe fields reflected from the cavity.

Higher order transverse (spatial) modes can influence intensity measurements. For example, both 00 and higher order Hermite-Gaussian modes can coresonate in the cavity and transmit to TRANS PD. Any scatter or clipping on the transmission beam path will cause these orthogonal modes to interfere on TRANS PD, leading to intensity fluctuations that do not correspond to amplitude fluctuations of the cavity's resonating 00 mode. This effect is even more pronounced on REFL PD, which can see significant power from higher order Laguierre-Gaussian modes due to mode mismatch of either pump or probe beams relative to the cavity.

Pound-Drever-Hall Error Signal

Pound-Drever-Hall locking, the technique of dithering a laser frequency far outside the cavity bandwidth to derive an error signal linear in the laser-cavity frequency difference, is widely used in laser stabilization including LIGO's arm length stabi-

lization [167]. A good, pedagogical explanation of PDH is from Black [168], who shows that the PDH frequency discriminant on-resonance is

$$D \equiv -\frac{8\sqrt{P_c P_s}}{\delta\nu} \tag{9.1}$$

where P_c is the carrier field power, P_s is the sideband field power, and $\delta\nu \equiv \Delta\nu_{FSR}/\mathcal{F}$ is the cavity linewidth determined by the cavity's free spectral range ν_{FSR} and finesse $\mathcal{F}$.

For a given pump laser power setting the shot noise level of the PDH measurement, sensitivity of the PDH sensor is determined in part by the PDH sideband modulation depth. By beating the modulated pump with a second probe laser, we can read off the modulation depth from an RF spectrum analyzer as

$$\frac{P_{\text{carrier}-\text{probe}}}{P_{\text{sideband}-\text{probe}}} = \frac{J_0(m)^2}{J_1(m)^2}. \tag{9.2}$$

for $J_\nu(m)$ the ν order Bessel function of the 1st kind at modulation index m and $P_{\text{fieldA}-\text{fieldB}}$ the optical power in the beat note between field A and field B. The optimal SNR for the PDH error signal occurs at $m = 1.08$, but we choose a lower modulation depth around 0.15 to avoid unwanted polarization rotation at the fiber EOM.

We can directly measure the slope of the PDH error signal on-resonance (D) by sweeping the carrier laser frequency and both sidebands through resonance much faster than the cavity linewidth or any dominant frequency noises. The sideband fields are a known frequency away from the main carrier, so it is straightforward to plot the swept error signal against cavity frequency. The form of the total error signal can be found in [168], and is plotted in 9.1. Instead of fitting the full error signal, we can also use the analytic form of the PDH error signal near resonance to read off the PDH slope only from the peak-to-peak error signal voltage and frequency separation of the main carrier field as

$$\frac{\partial\epsilon}{\partial f} = 2\frac{\Delta V_{\text{pkpk}}}{\Delta t_{\text{pkpk}}}\frac{\Delta t_{\text{sideband}}}{\Delta f_{\text{sideband}}} \tag{9.3}$$

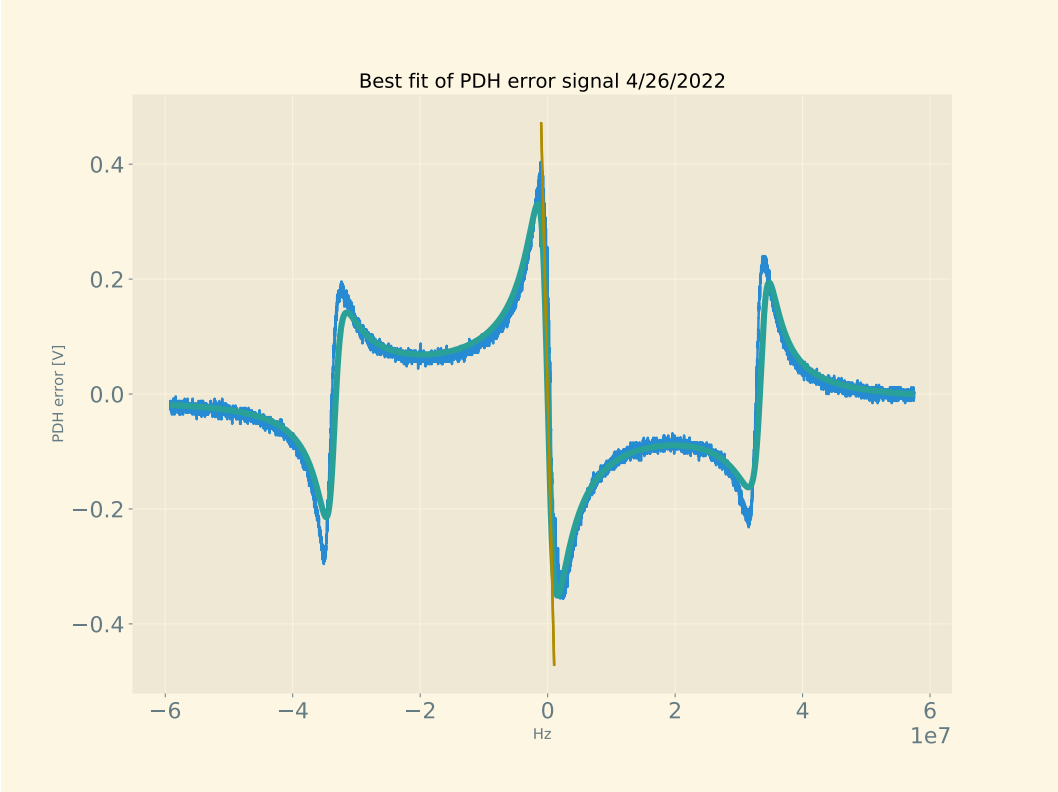

Figure 9.1: PDH error signal fitted to find a frequency discriminant of 2.2 MHz/V.

Delay-line Frequency Discriminator

Though we ultimately need to phaselock the pump and probe lasers, the experiment presents some challenges. With the pump laser PDH locked to the cavity, free-running pump-probe beat note frequency noise can exceed 200 MHz-pp at the high Q cantilever's resonance (typically 20-70 Hz, depending on choice of cantilever). Even with loop suppression, the resulting phase deviations can approach or exceed the linear range of our PLL sensor. We therefore require a beat note frequency sensor with a relatively wide dynamic range in order to linearize the phaselock response for large frequency deviations. A wide band frequency sensor can also prestabilize the beat note frequency in a low-bandwidth (100s Hz) loop to aid in PLL lock acquisition.

We use an RF delay-line frequency discriminator (DFD) to sense beat note frequency fluctuations. The DFD is based on an unbalanced Mach-Zehnder interferometer as in Fig. 9.2. The beat note is split into two paths (using ZFRSC-42-S+) then recombined at an RF mixer (ZFM-3-S+). To see how this works, consider the total electric field due to pump and probe carriers mixing on a photodiode, ignoring an overall phase:

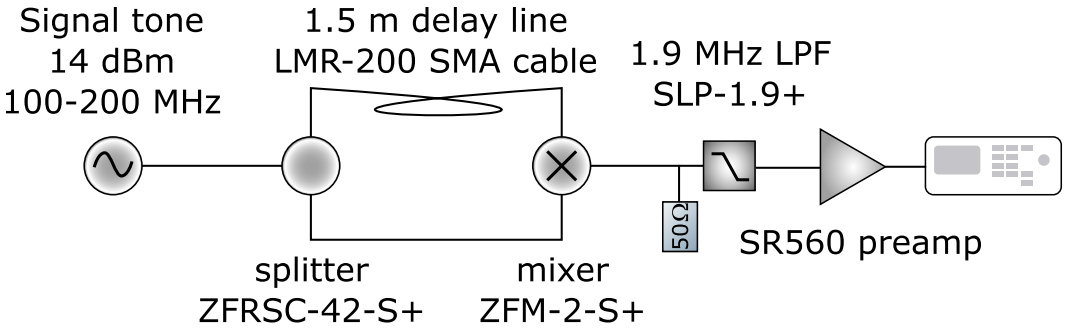

Figure 9.2: Electronics diagram for the delay line frequency discriminator. In our application, the signal is the beat note between pump and probe lasers measured at REFL PD.

$$E(t) = E_{\text{pump}} e^{i\omega_{\text{pump}} t} + E_{\text{pump}} e^{i\omega_{\text{probe}} t}. \tag{9.4}$$

Typical commercial InGaAs photodiodes have a sensitivity $\approx$ 1 A/W at 1550 nm. The current is transduced to a voltage by a low noise transimpedance amplifier such that the overall responsivity is $\mathcal{R}(\Omega)$ V/W. Let us assume for now the photodiode has a flat frequency response at its DC and AC coupled outputs, $\mathcal{R}(\Omega) \equiv \mathcal{R}_{\text{DC,AC}}$. The AC-coupled output voltage then highpasses $\mathcal{R}(\Omega)|E(t)|$:

$$V_{\text{PD}}(t) = 2\mathcal{R}_{\text{AC}} E_{\text{pump}} E_{\text{probe}} \cos((\omega_{\text{pump}} - \omega_{\text{probe}})t). \tag{9.5}$$

We want to stabilize the beat note frequency $\omega_{\text{beat}}(t) \equiv \omega_{\text{pump}}(t) - \omega_{\text{probe}}(t)$. After the RF splitter, the beat note propagates at velocity $c_{\text{cable}} \approx 2 \times 10^8 \text{m/s}$ in cables of length $L_{\text{L,R}}$ such that the signals entering the mixer's LO and RF ports are:

$$V_{\text{i}}(t) = \frac{1}{2}\mathcal{R}_{\text{AC}} E_{\text{pump}} E_{\text{probe}} \cos(\omega_{\text{beat}}(t - \frac{L_i}{c_{\text{cable}}})). \tag{9.6}$$

The mixer output is then lowpassed, such that the DFD output varies sinusoidally with $\Delta L \equiv L_{\text{R}} - L_{\text{L}}$ and $\omega_{\text{beat}}(t)$.

$$V_{\text{IF}} \propto V_{\text{L}}(t) V_{\text{R}}(t) V_{\text{out}} = V_0 \cos(\frac{\omega_{\text{beat}}(t)\Delta L}{c_{\text{cable}}}) \tag{9.7}$$

When the beat note frequency satisfies $\frac{\omega_{\text{beat}}(t)\Delta L}{c_{\text{cable}}} = (N + \frac{1}{2})\pi$ for $N \in \mathbb{Z}$,

$$V_{\text{out}} \approx V_0 \frac{\omega_{\text{beat}}(t)\Delta L}{c_{\text{cable}}}. \tag{9.8}$$

To operate the double-balanced mixer as a phase detector, we use a combination of RF amplifiers and attenuators to ensure the beat note saturates the mixer diodes. This reduces the coupling of beat note amplitude variations to the mixer IF port. In practice the proportionality factor in Eq. 9.8 for a level 7 mixer is $V_0 \approx 0.25\frac{\mathrm{V}}{\mathrm{rad}}$. If we read out the DFD output with an SR560 preamplifier with $\approx 4\mathrm{nV}/\sqrt{\mathrm{Hz}}$ voltage noise, the input referred noise of the DFD is inversely proportional to the path length difference along the two paths:

$$\hat{n}_{\mathrm{freq}} = \hat{n}_{\mathrm{V}} \frac{\mathrm{d}f_{\mathrm{beat}}}{V_{\mathrm{out}}} = \hat{n}_{\mathrm{V}} \frac{c_{\mathrm{cable}}}{2\pi V_0 \Delta L} \approx 1.3 (\frac{0.1\mathrm{m}}{\Delta L})(\frac{0.25\mathrm{V}}{V_0}) \frac{\mathrm{Hz}}{\sqrt{\mathrm{Hz}}}. \tag{9.9}$$

Phase Locked Loop Error Signals

We ultimately need a sensor for pump-probe phase error, not just frequency error. We can measure the phase of the pump-probe beat note relative to a reference oscillator (like a digital or analog voltage controlled oscillator (VCO)) by homodyne demodulation. As we will see later, we would like to consider contributions to the demodulated signal not just of the carrier fields and their frequency fluctuations, but of sidebands of the carriers.

Consider the electric field incident on a photodiode due to the combination of a pump laser at ω_{pump} and probe laser at ω_{probe}. The subscripted 0 or 1 indicates carrier or first order sideband, respectively. ϕ_{mod} controls whether the probe's modulation sideband is AM ($\phi_{\mathrm{mod}} = 0$) or PM ($\phi_{\mathrm{mod}} = \frac{\pi}{2}$).

$$\begin{aligned} E_{\mathrm{beat}} =& E_{\mathrm{pump}} e^{i\omega_{\mathrm{pump},0}t} [1 + \frac{E_{\mathrm{pump},1}}{E_{\mathrm{pump},0}} \frac{e^{i\omega_{\mathrm{pump},1}t} - e^{-i\omega_{\mathrm{pump},1}t}}{2}] + \\ & e^{i\phi_{\mathrm{probe}}} E_{\mathrm{probe},0} e^{i\omega_{\mathrm{probe},0}t} [1 + \frac{E_{\mathrm{probe},1}}{E_{\mathrm{probe},0}} (\\ & \cos\phi_{\mathrm{mod}} \frac{e^{i\omega_{\mathrm{probe},1}t} + e^{-i\omega_{\mathrm{probe},1}t}}{2} + \\ & \sin\phi_{\mathrm{mod}} \frac{e^{i\omega_{\mathrm{probe},1}t} - e^{-i\omega_{\mathrm{probe},1}t}}{2})] \end{aligned} \tag{9.10}$$

The voltage from the photodiode will then be proportional to optical power. We can focus only on terms rotating at the beat frequency $\omega_{\mathrm{beat}} \equiv \omega_{\mathrm{pump}} - \omega_{\mathrm{probe}}$, but let us also allow $\omega_{\mathrm{probe},1} \approx \omega_{\mathrm{beat}} + \phi_{\mathrm{probe},1}(t)$ while $\omega_{\mathrm{pump},1}$ is far from 0 Hz and far from ω_{beat}

$$
\begin{aligned}
P_{\text{beat}} =& e^{i\phi_{\text{probe}}} E_{\text{probe},0} E_{\text{pump},0} e^{-i\omega_{\text{beat}} t} + \\
& E_{\text{probe},0} E_{\text{probe},1} \cos\phi_{\text{mod}} \frac{e^{-i\omega_{\text{probe},1} t} + e^{i\omega_{\text{probe},1} t}}{2} + \\
& E_{\text{probe},0} E_{\text{probe},1} \sin\phi_{\text{mod}} \frac{e^{-i\omega_{\text{probe},1} t} - e^{i\omega_{\text{probe},1} t}}{2} + \\
& c.c. \\
=& 2E_{\text{probe},0} E_{\text{pump},0} \cos(\omega_{\text{beat}} t + \phi_{\text{probe}}(t)) + \\
& 2E_{\text{probe},0} E_{\text{probe},0} \cos\phi_{\text{mod}} \cos(\omega_{\text{beat}} t + \phi_{\text{probe},1}(t)).
\end{aligned}
\tag{9.11}
$$

Due to the complex conjugation, terms involving $\sin\phi_{\text{mod}}$ ideally will be cancelled. However, if there is some sideband asymmetry the cancellation will be imperfect. Terms with $\cos\phi_{\text{mod}} \neq 0$ (probe amplitude modulation at ω_{beat}) are not cancelled.

We then demodulate P_{beat} by demodulating against a VCO at $\omega_{\text{VCO}} \equiv \omega_{\text{beat}}$, this time keeping only low frequency terms. The demodulated and lowpassed voltage is the PLL error signal, e_{PLL}.

$$
e_{\text{PLL}} = K_{\text{PLL},0} \sin(\phi_{\text{VCO}}(t) - \phi_{\text{probe},0}(t)) + K_{\text{PLL},1} \cos(\phi_{\text{mod}}) \sin(\phi_{\text{VCO}}(t) - \phi_{\text{probe},1}(t)) \tag{9.12}
$$

We have introduced K as overall gains combining the various field amplitudes above, as well as losses associated with electronics and photodetection. For small noises associated with the probe's modulation sidebands, e_{PLL} is an error signal $\propto \phi_{\text{VCO}}(t) - \phi_{\text{probe},0}(t)$, the phase of the pump-probe beat note relative to the VCO phase. A more detailed derivation and noise analysis of the PLL error signal without probe modulation sidebands is in the technical note from Gupta [169].

9.2 Actuators

We want to actuate on optical field frequencies and amplitude, as well as mechanical positions. We mostly use rigid optical mounts, so pitch and yaw alignment do not change significantly during a single measurement.

Acoustic-Optic Modulator

We use an acoustic-optic modulator (AOM) to amplitude modulate our pump's carrier field and its PDH sidebands. With the AOM's 0th order transmitted beam aligned to the cavity and its 1st order transmitted beam dumped, we set the AOM's

drive amplitude to reduce intensity on PMON by about 10%. Amplitude modulating the AOM's drive amplitude then imparts AM sidebands on the 0th order transmitted beam. Because the AOM acts as a diffraction grating, any unwanted phase modulation on the AOM drive does not significantly phase modulate the 0th order transmitted beam.

Laser current

Actuating laser current directly modulates laser frequency. For AlGaAS diode lasers, the frequency modulation is due to carrier modulation at high frequency and temperature modulation at low frequencies [170]. Laser current modulation also has a typically undesired coupling to laser amplitude.

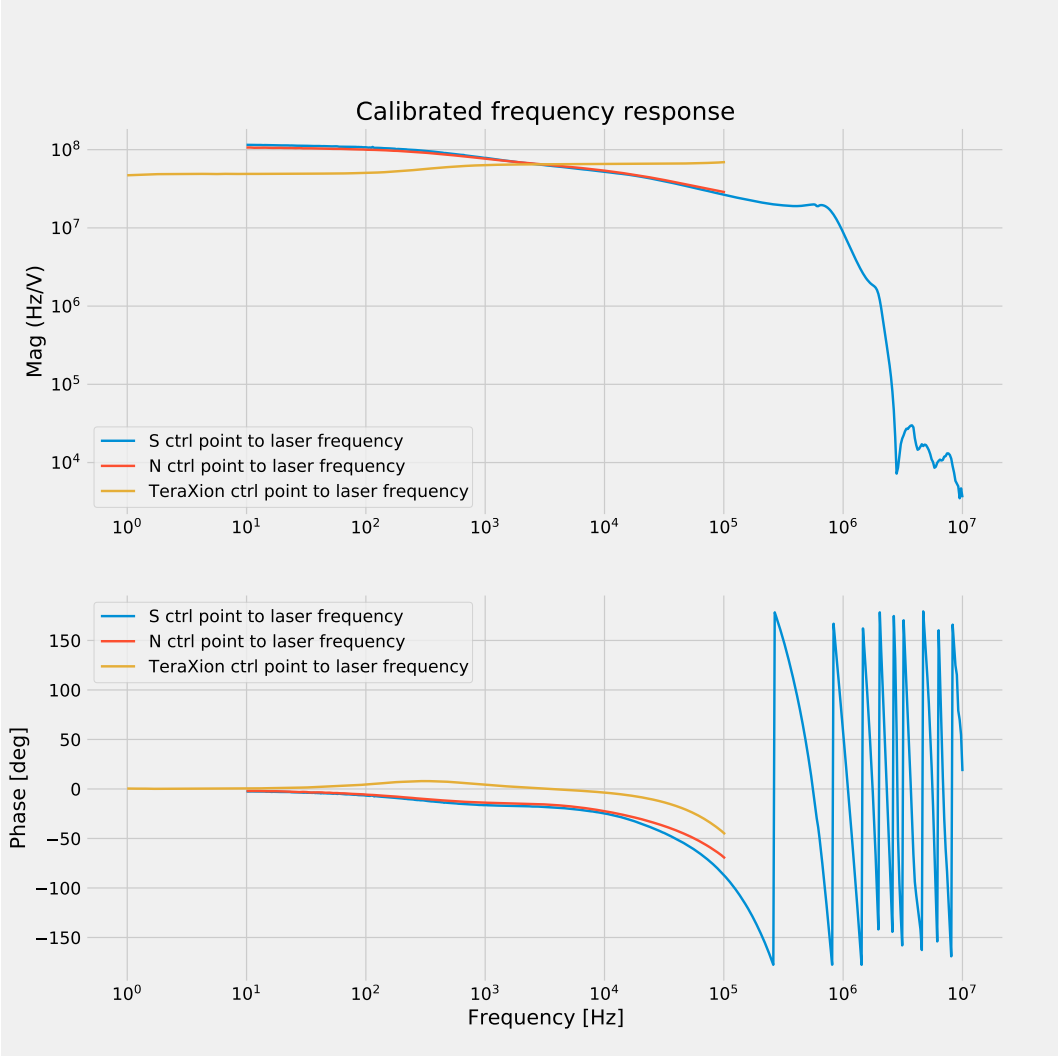

Figure 9.3: Frequency response of TeraXion and Rio (N and S) lasers to voltage modulations at the input of their respective current drivers.

Piezoelectric Actuator

We use a piezoelectric actuator, shown in Fig. 8.10, in vacuum to push on the base of the cantilever mount. The piezo drives MC2 relative to MC1 and MC3, filtered by the cantilever's mechanical response.

9.3 Controllers

Pound-Drever-Hall Loop

We lock the pump laser to the cavity resonant frequency with a PDH loop. The control filter has a zero at the cavity pole frequency to compensate phase delay introduced by the cavity. At low frequency, the pump current controller saturates. However, we feed back the integrated PDH control signal to pump diode temperature to stabilize the PDH loop on long (<1 Hz) timescales.

As shown in Fig. 9.6, we also feed back the PDH error signal to cantilever mirror position by piezoelectric actuator. We resonantly filter the piezo signal at the cantilever's fundamental resonance to damp the cantilever but minimally affect signals away from this eigenfrequency.

Ponderomotive rigidity

An optical cavity held close to resonance should not have a very rigid optical spring, because the cavity's circulating power has a maximum near resonance (the derivative of optical power with respect to frequency detuning is zero). However, by design PSOMA's light mirror has a low mechanical resonance, such that pump intensity fluctuations dominate the cantilever's motion. To understand the effect of the optical spring on mirror motion in PSOMA, consider the optical rigidity $K(\Omega)$ given by [29]

$$K(\Omega) = K_0 \frac{1 + (\delta/\gamma)^2}{(1 + i\Omega\gamma)^2 + (\delta/\gamma)^2} K_0 = \frac{128\pi I_0(\delta/\gamma)}{T_I^2 c\lambda_0} \left(\frac{1}{1 + (\delta/\gamma)^2}\right)^2 \tag{9.13}$$

where δ is the cavity detuning, Ω is signal frequency, γ is cavity linewidth, I_0 is the power incident on the cavity, T_I is input mirror power transmissivity, c is the speed of light in the cavity, and λ_0 is the laser wavelength. The condition for ponderomotive rigidity to dominate the mechanical restoring force is $K >> \mu\Omega_0^2$, where our mechanical mass is $\mu \approx 1g$ and cantilever resonance is $\Omega_0 \approx 25$Hz. For $I_0 \approx 15$ mW, $T_I \approx 330$ ppm, and $\gamma \approx 100$ kHz, the optical spring starts to dominate mechanical restoring force when $\delta > 23Hz$, or about 0.02% of the full range of the PDH error signal for the unlocked cavity sweeping across resonance.

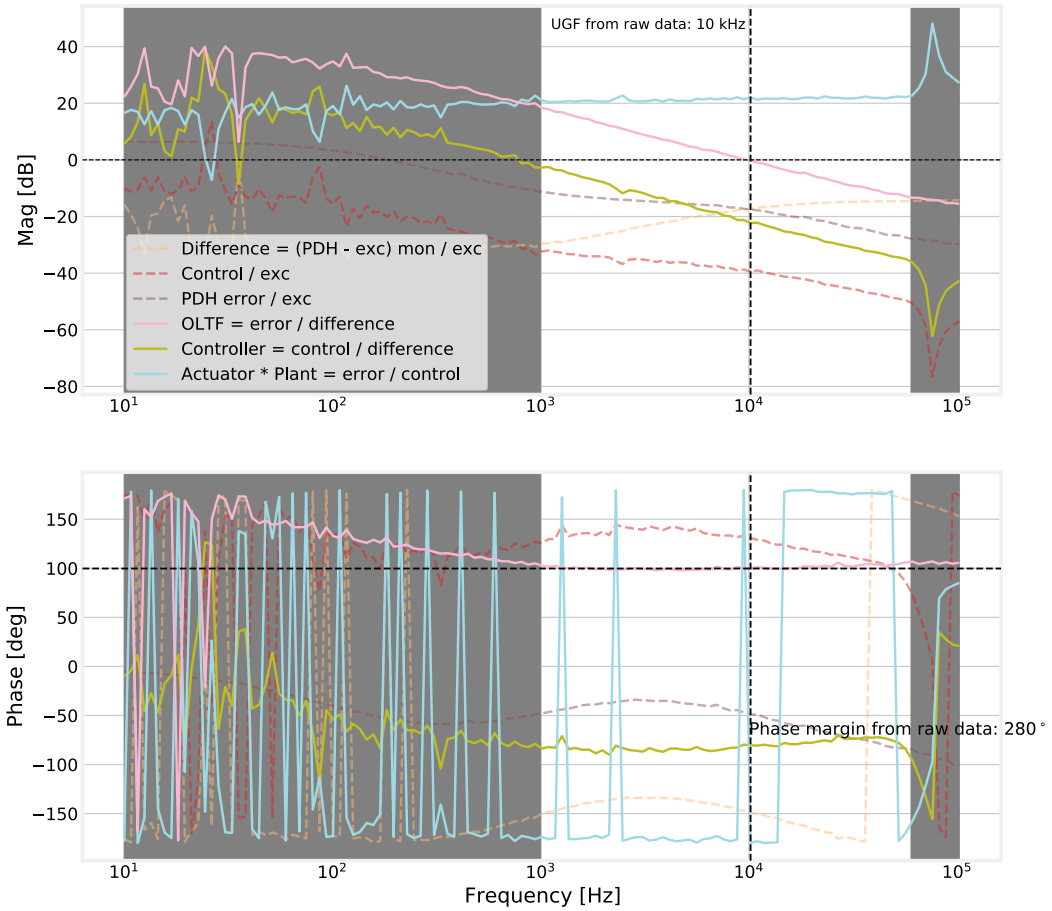

Figure 9.4: Transfer functions of the Pound-Drever-Hall loop. The gray regions are where the measurement had low coherence. The excitation was summed into the loop at the the PDH error point, where the residual noise has a mostly flat spectral density. The yellow controller transfer function derived from the measurement agrees well with the digital controller set in Moku. We cannot see the cavity pole in the plant transfer function magnitude because the cavity is pumped with p-polarized light (low cavity finesse) for this measurement. The unity gain frequency of the open loop transfer function is about 10 kHz.

Marquardt et al have studied analytically the dynamical behavior of a resonant, high-finesse optical cavity with one compliant mirror, which suggests an interesting direction for future experimental work [171].

Pump-Probe Phaselock

We can feed back the DFD error signal to the probe laser to stabilize the pump-probe beat frequency, as in Fig. 9.6. The frequency locked loop (FLL) alone (PLL gain of 0) stabilizes the beat note with ≈ 356Hz unity gain frequency.

To further stabilize the beat note phase, we also lock the FLL-stabilized pump-probe

beat note to a digital oscillator generated by a Moku:Pro via phase-locked loop (PLL). We choose the digital LO frequency to be close to the DFD null frequency, but higher than the PDH sideband frequency to avoid contaminating the cavity lock. Because the PLL mixer is driven by an independent LO, its demodulated output is proportional to beat note phase rather than frequency. The phase is related to frequency by a single pole at 0 Hz in the Laplace domain, and the PLL sensor has the transfer function

$$P_{\mathrm{PLL}}(s) = \frac{P_{\mathrm{PLL},0}}{s}. \tag{9.14}$$

We sum the pump-probe PLL and FLL control signals to simplify control filter design. The overall loop has up to $\approx$ 200 kHz UGF, though with the cavity locked we usually operate with closer to 75 kHz UGF. The loop's response is dominated by the PLL sensor throughout the control band. The FLL only prevents the loop from losing lock during phase deviations that exceed the linear range of the PLL plant. The open loop transfer function is

$$G_{\mathrm{beat}} = A(H_{\mathrm{FLL}}P_{\mathrm{FLL}} + \frac{H_{\mathrm{PLL}}P_{\mathrm{PLL}}}{s}). \tag{9.15}$$

9.4 Quadrature Sensing

To fully characterize the cavity's 2-quadrature transfer function, we need to independently sense the pump's AM and PM sidebands both before and after the cavity. The pump-probe beat note provides an independent measure of pump frequency modulations, so stabilizing the beat note by PLL lets us sense pump PM as long as we record the beat note either immediately before or immediately after the cavity. In particular, we cannot use the beat note on BEAT PD to sense pump PM entering the cavity in conjunction with the probe laser-based signal injection scheme described in Section 9.5, since BEAT PD mixes pump and probe with a different phase than that set on BS1. On the other hand, for PM signals injected by directly modulating pump laser current, BEAT PD is a good sensor of pump PM entering the cavity, since the phase relation of the pump with the probe's resonant sideband is irrelevant to the injected signal.

9.5 Coherent Signal Injection

PSOMA is designed to amplify quantum noise limited signals on squeezed vacuum fields by taking advantage of the Mach-Zehnder interferometer's common mode

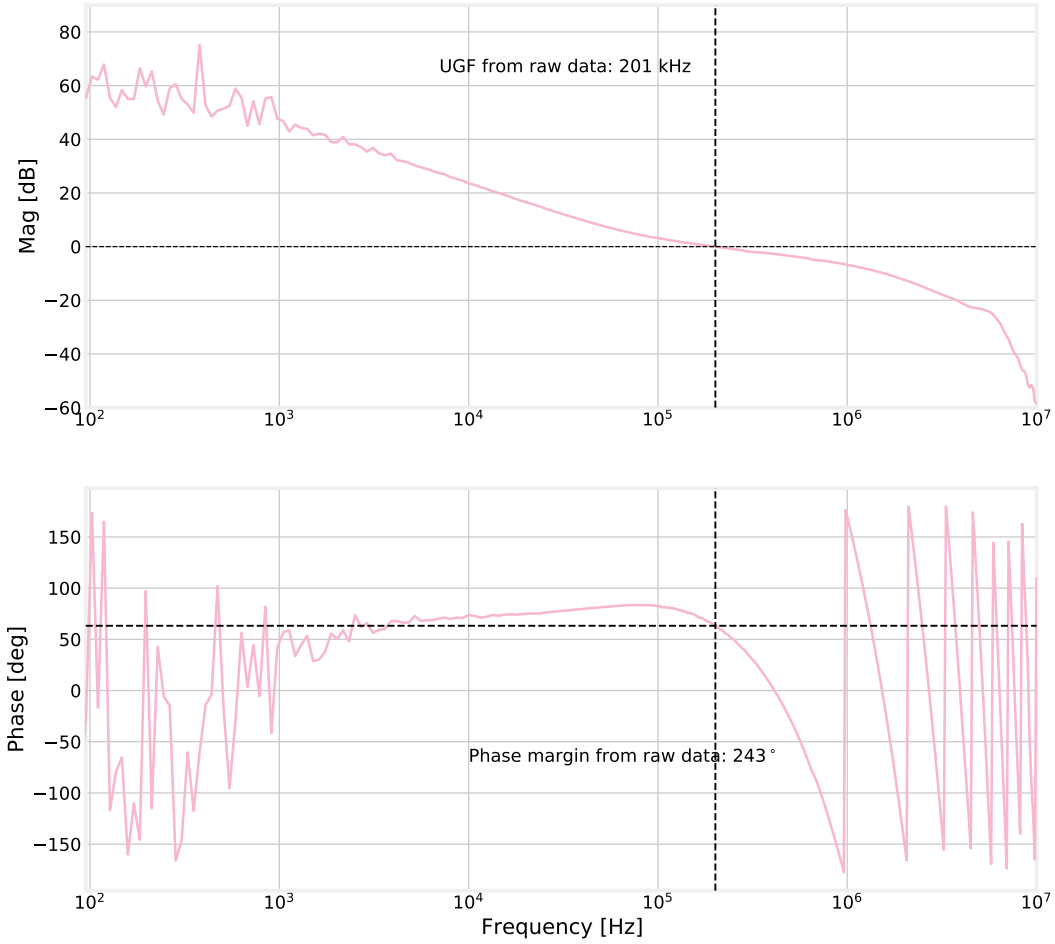

Figure 9.5: Open loop transfer function (OLTF) of the pump-probe PLL, with cavity unlocked and no FLL engaged ($H_{\mathrm{FLL}} = 0$).

rejection of fields entering PSOMA's pump port. We therefore need a strategy for phaselocking the probe field entering PSOMA's input port to the PSOMA pump, and generating signal sidebands around that probe field. The basic problem is analogous in many ways to the control of LIGO's squeezed injection field [172] [173] [174] [175] and filter cavity for frequency-depending squeezing [176]. We use a coherent locking field (CLF) copropagating with the pump but outside PSOMA's amplified band as a surrogate for the amplified quadrature angle (the phase of signal sidebands around the probe carrier relative to the pump). For design flexibility, we use an auxiliary laser to generate a CLF. Future work should consider generating the CLF with two AOMs, to eliminate noise associated with the PLL.

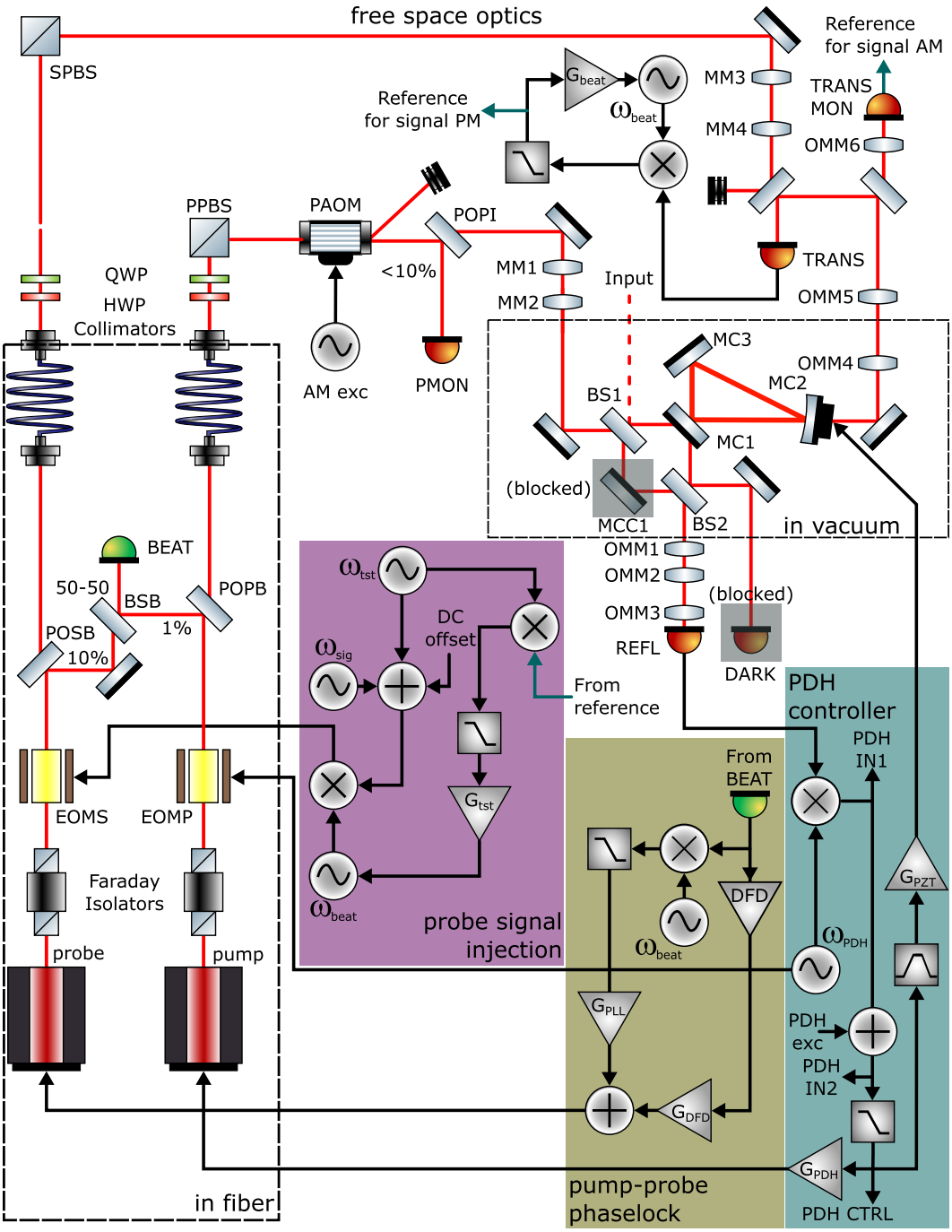

Figure 9.6: Control System Diagram

9.6 Closed System Model

In order to understand our measurements of the multiple-input multiple-output transfer functions, we made a Finesse3 model of our experiment as it exists on the tabletop.

The model implements all core optics, including ring cavity, Mach-Zehnder input

and output beamsplitters, pickoffs, fiber beat note monitor, and REFL/TRANS/PMON photodiodes. The key parameters are realistic, including all transmissivities, cavity and Mach-Zehnder arm lengths, and cavity losses. We implement realistic and dimensionful control filters for the PDH and PLL control loops and manually "lock" the model by maximizing signals that indicate lock (such as cavity transmission and beat note demodulation Q-quadrature). We use the model the calculate the closed loop transfer functions that are sufficient to estimate open loop transfer function of the cavity (including both amplitude and phase quadratures).

The model does not contemplate several auxiliary control loops, including slow laser temperature control and mechanical damping of the cantilever. Cantilever damping should be considered in future versions of the numerical model. We also leave to future work modeling of the coherent signal injection scheme described above.

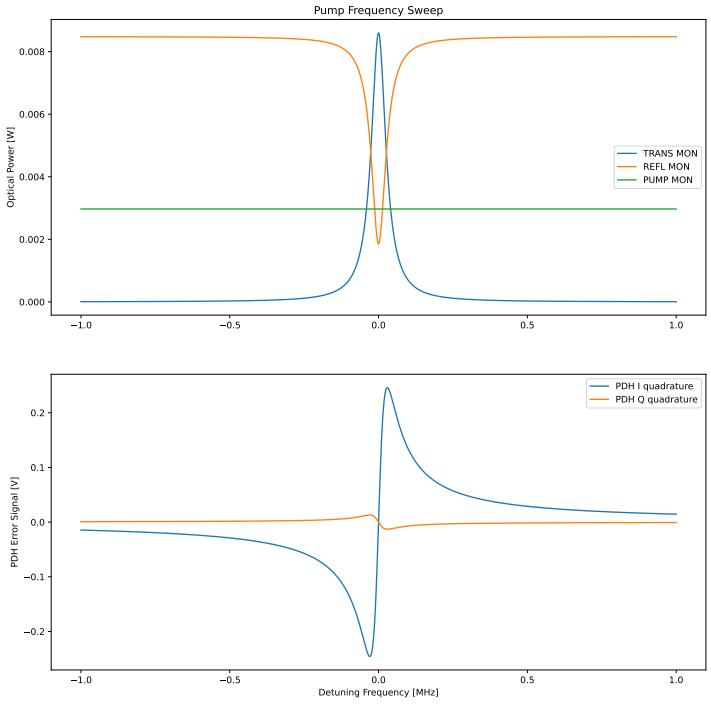

Figure 9.7: PDH sweep simulated in Finesse 3. Top: DC signals on transmission, reflection, and pump monitor photodiodes while sweeping pump frequency relative to cavity resonance. Bottom: PDH error signal in I and Q quadratures while sweeping pump frequency relative to cavity resonance.

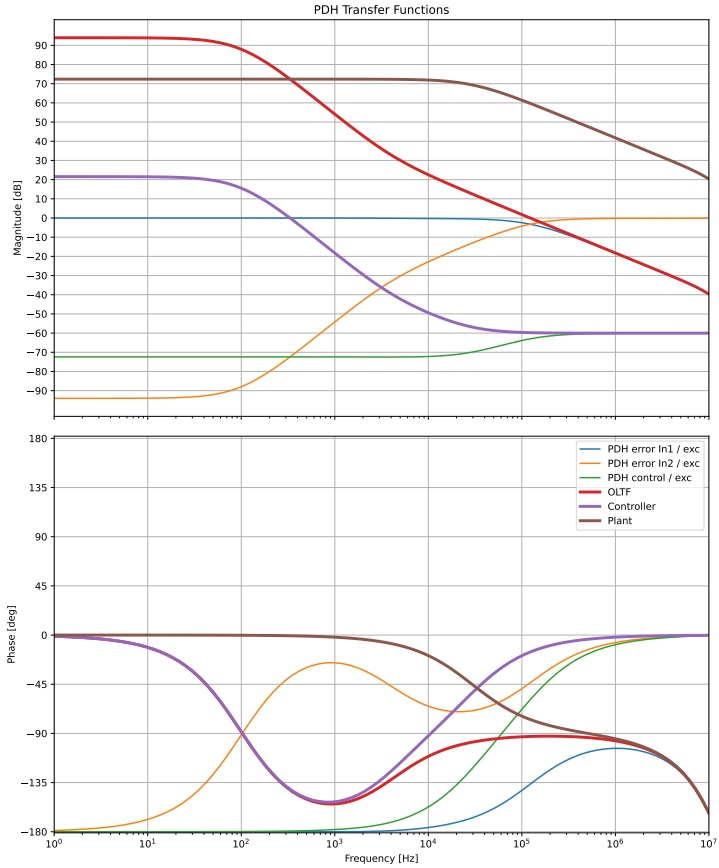

Figure 9.8: Bode plots of PDH loop in Finesse3 model. Excitation is summed at the PDH error point, with In1 just before and In2 just after the summation point. OLTF, Controller, and Plant are the open loop transfer functions.

Improving model fidelity

The model is currently sufficient to validate the amplitude- and phase- cavity transfer functions to lowest order. However, it could be improved in several ways.

Finesse3 defaults to using single-sided mirrors, rather than mirrors with both HR and AR surfaces. Implementing two-sided mirrors would be useful especially as the model is used for studying scatter and the effects of higher order modes.

We should also implement realistic path lengths, mode matching optics, and optical losses outside of the cavity. The numerical model should be useful for understanding how higher order modes affect our measurements, for example by biasing the PDH

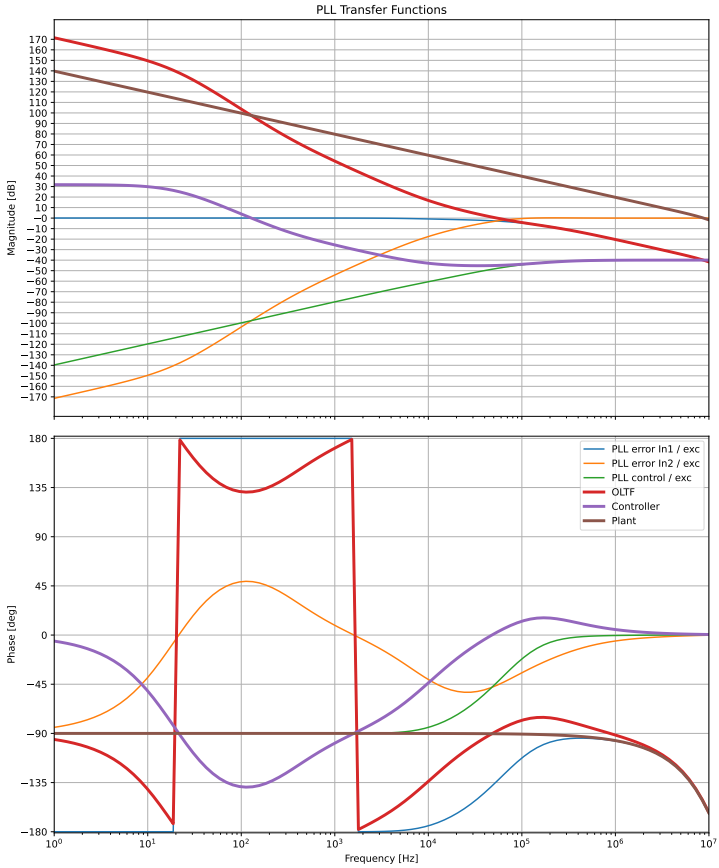

Figure 9.9: Bode plots of the phase-locked loop stabilizing pump-probe beat frequency on REFL photodiode. Excitation is summed at the PLL error point, with In1 just before and In2 just after the summation point. OLTF, Controller, and Plant are open loop transfer function.

error point offset.

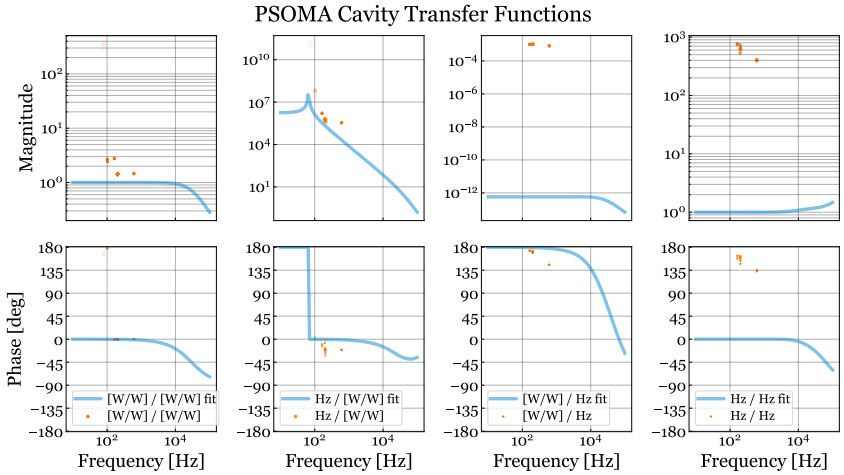

Figure 9.10: Finesse3 model and measured tansfer functions of optical amplitude and frequency across the cavity, derived from the PDH and PLL transfer functions in 9.9 and 9.8. Note that there is some disagreement due to unmodeled FM-to-AM coupling, and possibly due to lack of measurement coherence (transparent points have less coherence) especially near the mechanical resonance. FM input is taken as the pump-probe PLL at BEAT PD; FM output is taken as the PDH control signal referred to frequency; AM input is measured at Pump MON PD; AM output is measured at TRANS MON. Note, too, that the VCO frequency on TRANS independently monitors FM out, and after correcting for PLL-suppression would not turn upwards as in the rightmost plot.

Chapter 10

OPTOMECHANICAL AMPLIFIER CHARACTERIZATION

We characterized the current status of the PSOMA demonstration by estimating the frequency noise budget of the PDH sensor, and by making a first pass at measuring the two-quadrature transfer functions of the cavity.

10.1 System Identification

The system parameters derived from measurements in this section are used to construct the amplifier noise budget in Section 10.2, and summarized in 10.1. A good reference on frequency domain system identification is [177].

Cavity Parameters

We measured the FSR of the PSOMA cavity to be $\Delta\nu_{FSR} \approx 675MHz$ by observing peaks in the cavity transmission profile while sweeping a p-polarized pump through resonance. We used p-polarized light to increase cavity transmission (the cavity mirrors are coated for s-polarized light to reduce their sensitivity to angle of incidence) during FSR measurements.

Most recent cavity transfer functions

The latest measurements towards the cavity transfer function are in Fig. 9.10. The data are noise dominated except in a few cases. We also note that the observed amplitude-to-frequency transfer function has good coherence but is not consistent with ponderomotive amplification (which would have a $1/\Omega^2$ response as in 9.9). We have previously noted some at least $0.03\%/MHz$ coupling of PDH control frequency to relative intensity noise on PMON, but there could be electronic or other crosstalk responsible.

We use the coherence γ^2 at each frequency Ω_k of the swept sine to estimate the variance of the transfer functions as [177]

$$\sigma^2(\Omega_k) = |G(i\Omega_k)|^2 \frac{1-\gamma^2(\Omega_k)}{\gamma^2(\Omega_k)}. \tag{10.1}$$

Ultimately we would like to use our transfer function measurements to refine the parameters of a physical model like that in Section 9.6. We leave this to a future

Figure 10.1: Transmission profile (blue) while driving the laser current (red) with a triangle wave to sweep laser frequency across cavity resonances. The PDH error signal (green) and known sideband modulation frequency lets us convert the x-axis to MHz. The yellow trace is the DC monitor on REFL PD.

with a quieter cavity and more accurate model.

10.2 Noise Budget

The noise budget compares various noises due to PSOMA and measured at its output as if they could all be attributed to sources at input of a noiseless amplifier with gain $G(\Omega)$. PSOMA's input-output relation in Eq 3.1 can be reduced to a single gain $G(\Omega)$ for signals $h(\Omega)$ entering along $\hat{b}_{in,1}$ and transmitted along $\hat{b}_{\mathrm{out},2}$, along with total noises $n_i(\Omega)$.

$$b_{\mathrm{out},2}(\Omega) = G(\Omega)(h(\Omega) + n_i(\Omega)) \tag{10.2}$$

Any noise appearing at the output $\hat{b}_{\mathrm{out},2}$ with spectral density $S_{\mathrm{out,i}}(\Omega)$, even those coupled in from $\hat{b}_{\mathrm{in},2}$, can be input-referred and contribute to the total measured input-referred noise S_{in}.

Symbol	Description	Measured Value	Future Value
$\Delta\nu_{FSR}$	Ring Free Spectral Range	675 MHz	675 MHz
$P_{\text{pump,launch}}$	Pump Power from Collimator	33 mW	–
P_{circ}	Cavity Circulating Power	$\approx$ 1 W	560 W
$\mathcal{F}$	Cavity Finesse	$\approx$ 9,000	19,000
L_{cav}	Cavity Length	44.4 cm	37 cm
r_{beam}	Beam waist radius	$\approx$ 350 μm	215 μm
f_{mech}	Cantilever Frequency	66 Hz	43 Hz
Q_{mech}	Cantilever Q	$\approx 3e5$	1e6
m_{mech}	Cantilever mirror mass	$\approx$ 1 g	0.5 g
$S_{\text{RIN,0}}$	Pump RIN floor	–	$10^{-8}/\sqrt{\text{Hz}}$
f_{corner}	RIN corner frequency	–	100 Hz
S_{f}	Pump frequency noise	–	$10^{-10}\text{Hz}/\sqrt{\text{Hz}}$

Table 10.1: Table of amplifier parameters. Measured values are characterized in 10.1 and used to derive the noise budget in Sec. 10.2. Future values are those used to project the performance of future upgrades in Fig. 10.7.

$$S_{\text{in}} = \sum_i \frac{S_{\text{out}}(\Omega)}{G(\Omega)} \tag{10.3}$$

Quantum

An optical vacuum field $\hat{v}$ with unit amplitude replaces the circulating field everywhere there is optical loss, as described in Eqs. 2.3 or 2.11. Quadrature detection of $\hat{v}$, for example by balanced homodyne detection with a local oscillator field intensity I_{LO} at ω_{LO}, would find a flat noise spectral density due to shot noise of

$$S_{\text{shot}} = \frac{\hbar c^2}{I_{\text{LO}}\omega_{\text{LO}}}. \tag{10.4}$$

The mirrors of the optomechanical system also experience a force noise due to shot noise from $\hat{v}$, and their dynamics are affected according to 2.15.

We include quantum noise in the projected future noise budget (10.7), but do not expect it to limit amplifier performance. Instead, quantum noise excluding vacuum fluctuations carried with the probe field is relevant as a figure of merit for PSOMA's utility to photodetection loss limited measurement devices. When we use an unsqueezed probe to characterize PSOMA, we can write the input-referred noise attributable to the amplifier as

$$S_{\text{amp}} = S_{\text{in}} - S_{\text{shot}}. \tag{10.5}$$

At frequencies where $S_{\text{in}} < S_{\text{shot}}$, we would expect sub-SQL signals to benefit from PSOMA's preamplification assuming sufficient amplifier gain.

Suspension Thermal

Suspension thermal noise is due to mechanical loss in the cantilever mirror suspension. Note that increasing mirror mass decreases suspension thermal noise, which can sometimes offer a favorable tradeoff with ponderomotive gain. For the calculation in 10.7, the displacement noise spectral density on the ith cantilever mirror $x_{ST,i}(\Omega)$ can be derived from the fluctuation-dissipation theorem for a mechanical oscillator with loss $\phi_{\text{mech}}(\Omega)$, resonant frequency ω_{mech}, and mass m held at temperature T [178].

$$x_{ST,i}(\Omega) = \sqrt{\frac{4k_BT}{m\Omega}\left(\frac{\omega_{\text{mech}}^2\phi_{\text{mech}}(\Omega)}{\omega_{\text{mech}}^4\phi_{\text{mech}}^2(\Omega) + (\omega_{\text{mech}}^2 - \Omega^2)^2}\right)} \tag{10.6}$$

Coating Brownian

Coating Brownian noise is another force noise arising from the fluctuation-dissipation theorem, this time applied to multiple stacked layers in a dielectric mirror coating. We can treat each unit area of the stacked coating somewhat independently, such that the phase imparted on a width w Gaussian beam profile reflected from the mirror surface falls off like $1/w^2$. In Fig. 10.7, we use the expression from Eq. 21 in [179] for the Brownian noise contribution just due to coatings. The ith mirror experiences displacement noise $x_{CBN,i}$ due to a mirror coating of thickness d, mechanical loss angle ϕ_c, Young's modulus Y_c, and Poisson ratio ν_c on a substrate with Young's modulus Y_s and Poisson ratio ν_s.

$$x_{CBN,i}^2 = \frac{2k_BT}{\pi^2\Omega}\frac{\phi_c d}{w_B^2 Y_s^2 Y_c(1-\nu_c)^2}\left(Y_c^2(1+\nu_s)^2(1-2\nu_s)^2 + Y_s^2(1+\nu_c)^2(1-2\nu_c)^2\right) \tag{10.7}$$

Laser Frequency Noise

It is possible to prestabilize PSOMA's pump laser to reduce its amplitude and frequency noise to at or near its shot noise level. However, in our tabletop demonstration

we simply stabilize the pump's frequency to the PSOMA cavity. For the single-cavity experiment, the pump's frequency noise sums with any amplified signal at the output of the amplifier.

At low frequency, the laser's shot noise is overcome by 1/f noise due to a combination of effects including Brownian thermal noise inside the fiber cavity substrate [180] and carrier density fluctuation at the diode interfaces [181].

For the projection in Fig. 10.7, we assume a flat pump frequency noise $S_f = 10^{-10}$ Hz/$\sqrt{\text{Hz}}$.

Noise in semiconductor lasers is further discussed in [182], [183], [184], [185], [186], [187], [188]. Some other frequency noise measurements are discussed in [189], [190].

To estimate the pump laser's frequency noise, we use a three corner hat measurement as described in Section A.1. The inferred laser frequency noise is represented in Fig. 10.2. It should be noted that because the TeraXion laser is much quieter than the two Rio lasers used as reference clocks in the three corner hat, uncertainty on the inferred TeraXion frequency is skewed to lower amplitude spectral density.

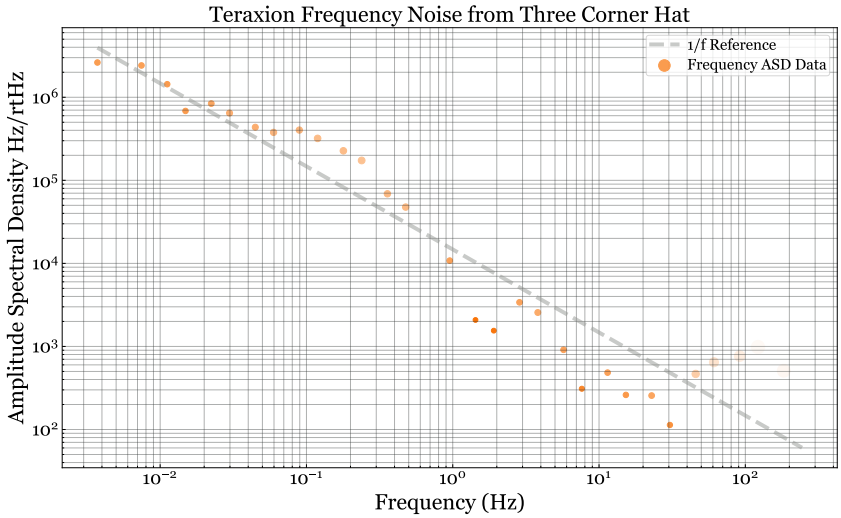

Figure 10.2: Frequency noise of the TeraXion (pump) laser inferred from three corner hat measurement. Scatter point opacity is inversely proportional to relative uncertainty in the ASD estimate.

Laser Amplitude Noise

The current configuration uses only one ring cavity rather than a balanced Mach-Zehnder with two ring cavities. We do not yet subtract amplified pump relative

intensity noise (RIN), which means pump RIN contributes directly to the input referred noise of the amplifier.

For the projection in Fig. 10.7, we assume pump RIN has the values in Table 10.7 and the form

$$S_{\mathrm{RIN}}(f) = \frac{f + f_{\mathrm{corner}}}{f} S_{\mathrm{RIN},0}. \tag{10.8}$$

Current Noise

The frequency of light emitted by the laser depends on the drive current applied across the diode, as described in Sec. 9.2. Therefore, current noise across the laser diode directly sources frequency noise of the laser frequency.

Seismic Noise

We characterized the seismic noise with a Wilcoxon accelerometer. The accelerometer contains a built-in current preamplifier, which we power using a low noise DC supply driving a JFET operated as a constant current source. We estimate the contribution of seismic noise to cavity frequency noise by using the nominal accelerometer calibration to put the accelerometer signal into m/rtHz at the cantilever mirror, which is then filtered by the cantilever mechanical response with two zeros at 0 Hz.

We observe a seismic noise peak between 20-30 Hz, which creates significant noise when the cantilever resonance falls in that range. For example, when operated with a 25 Hz cantilever, the cavity exhibits 100 nm/rtHz frequency noise at the cantilever resonance. For cantilevers with 25 Hz resonances, we found that seismic noise saturates our fast pump current actuation. We can still lock the cavity by damping this seismic noise by feeding either the cavity error signal or an auxiliary sensor of cantilever motion back to a piezo driving the cantilever base. We also switched to a cantilever with higher resonant frequency (66 Hz) in part to reduce seismic noise coupling.

Electronics

To diagnose the noise in Fig. 10.5, we observed the noise at the PDH error monitor point with PDH modulation off, probe laser blocked, and cavity off-resonance. The noise measured at PDH error is then referred to frequency noise at the cavity input and shown in 10.5 as the “electronics noise” curve, which agrees well with the total

observed noise. The demodulated voltage at the PDH error point is most directly attributable to a combination of (1) voltage noise below kHz between the PDH mixer output and the Moku ADC; (2) voltage noise around f_{PDH} = 33.59 MHz between REFL PD's transimpedance amplifier and the PDH mixer; (3) current noise around f_{PDH} = 33.59 MHz across the REFL photodiode; (4) pump intensity noise around f_{PDH} = 33.59 MHz.

There is no reason for pump intensity noise to peak around f_{PDH} when no PDH modulation is applied to the pump laser. Moreover, we do not observe such intensity noise using other photodiodes and a spectrum analyzer. But, we do observe that the noise is linearly related to pump power as shown in Fig. 10.3. This suggests the noise is sources before PDH demodulation.

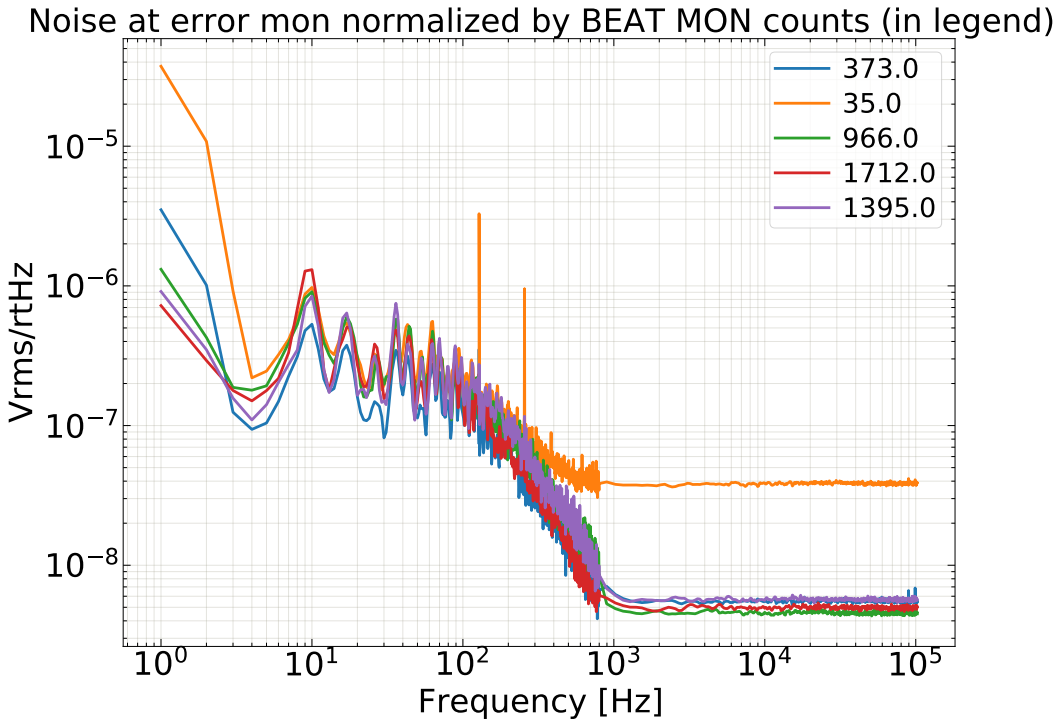

Figure 10.3: Noise at PDH error monitor point with no phase modulation applied to the pump laser is shown to be linearly proportional to pump power below 200 Hz.

Since measuring Fig. 10.5, we have electrically isolated TRANS and REFL PDs from the optics table to avoid potential ground loops affecting REFL PD. We also note that Fig. 10.5 is measured using p-polarized pump light, resulting in a relatively low cavity Finesse (under 1000). We expect measurements on the s-polarized cavity would see less electronics noise due to increased plant gain.

Pound-Drever-Hall Noise Budget

Though we ultimately anticipate using an independent sensor of frequency fluctuations at PSOMA's input, the PDH loop provides our most sensitive measurement of frequency noise at the cavity input.

The total noise in Fig. 10.5 is dominated at low frequency by likely electronics noise. We also observe total noise close to laser frequency noise at high frequency.

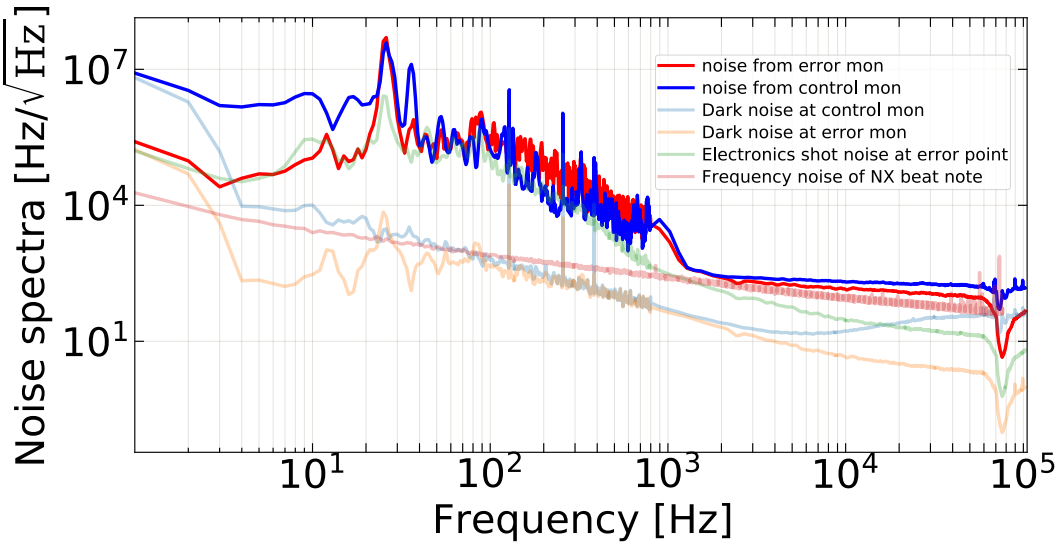

Figure 10.4: Frequency noise budget of the PSOMA cavity referred to frequency fluctuations at the cavity input. Measured with p-polarized pump, so the cavity gain is unusually low.

Quadrature Sensor Noise Budget

We can also estimate the noise referred to each of our quadrature sensors (see Sec. 9.4), rather than to the cavity input.

10.3 Outlook for Future Upgrades

Asymmetric Ring Cavity Mach-Zehnder

We already have optics for a Mach-Zehnder interferometer in place in the PSOMA vacuum chamber, but have not instrumented Mach-Zehnder length control or locked the interferometric degrees of freedom. The MZI can sense pump frequency fluctuations independent of cavity length fluctuations appearing in the PDH control signal. We anticipate installing length actuation on the MZ steering mirror opposite the existing ring cavity and locking the MZI would take 3 months.

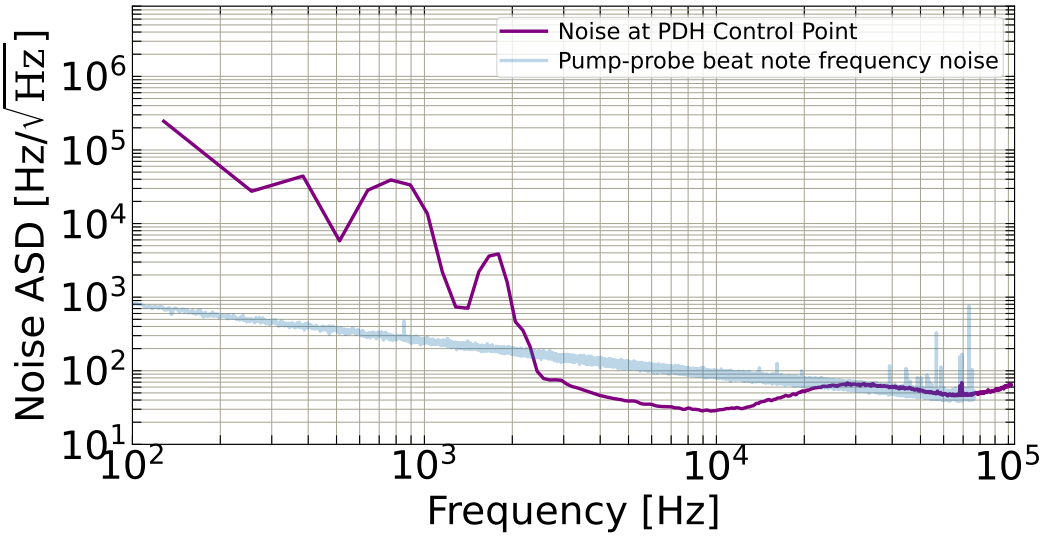

Figure 10.5: Frequency noise budget of the PSOMA cavity referred to frequency fluctuations at the cavity input. Measured with s-polarized pump. Note that the pump-probe beat note frequency noise curve contains both pump frequency noise (which contributes to total amplifier noise) and probe frequency noise (which does not contribute to total amplifier noise).

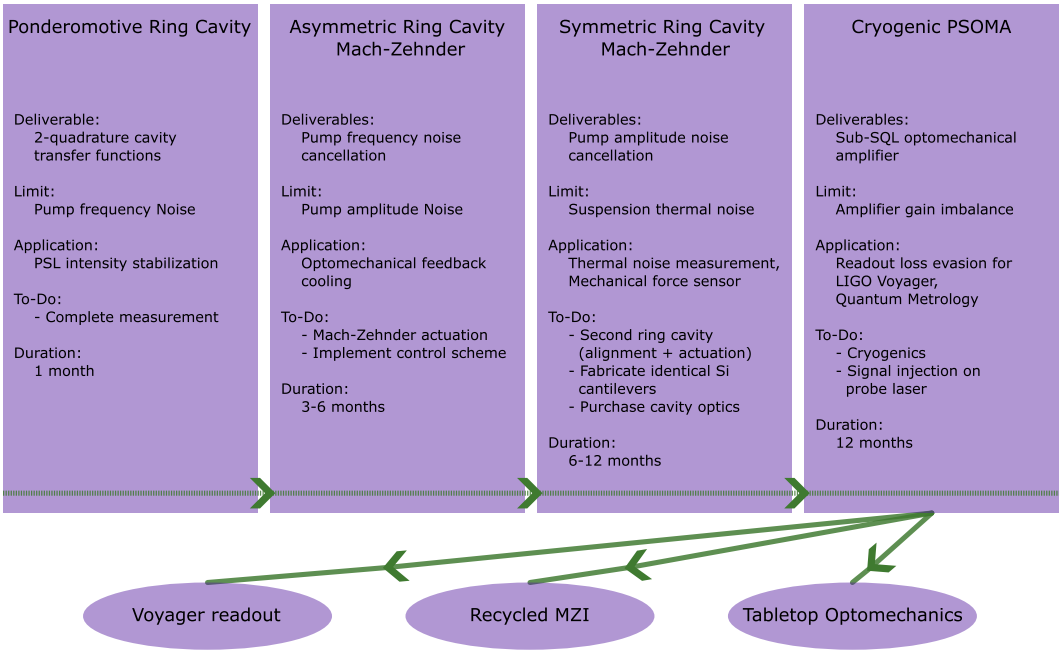

Figure 10.6: Outlook for the next several stages of the PSOMA experiment.

Symmetric Ring Cavity Mach-Zehnder

Because pump intensity noise is amplified in only one path of the asymmetric ring cavity MZI, we have no way to distinguish cantilever motion driven by signals carried with the probe field from motion driven by pump amplitude noise. Therefore, pump

RIN puts a floor in input-referred amplifier noise for the asymmetric configuration. By balancing the gain with identical ring cavities in each arm, amplified pump intensity noise is rejected out the bright port of the MZI.

Cryogenic PSOMA

With two balanced ring cavities, we expect the limiting noise differentially driving the two cavities to be thermal noise of the cavity mechanics. In particular, we expect suspension thermal noise due to the finite Q of the light cantilever mirrors to limit PSOMA's noise performance. By cooling the cantilevers to 123 K, we can take advantage of the low intrinsic mechanical loss of crystalline Si at this temperature, as well as a lower overall thermal bath temperature, to significantly increase the quality factor of PSOMA's ponderomotively active mirror suspensions.

To achieve sub-SQL input-referred noise, we must increase the Q of PSOMA's mechanically compliant optics. We can achieve this by cooling its Si cantilevers to 123 K, where we anticipate lower suspension thermal noise due to the reduced thermoelastic loss in Si at this temperature.

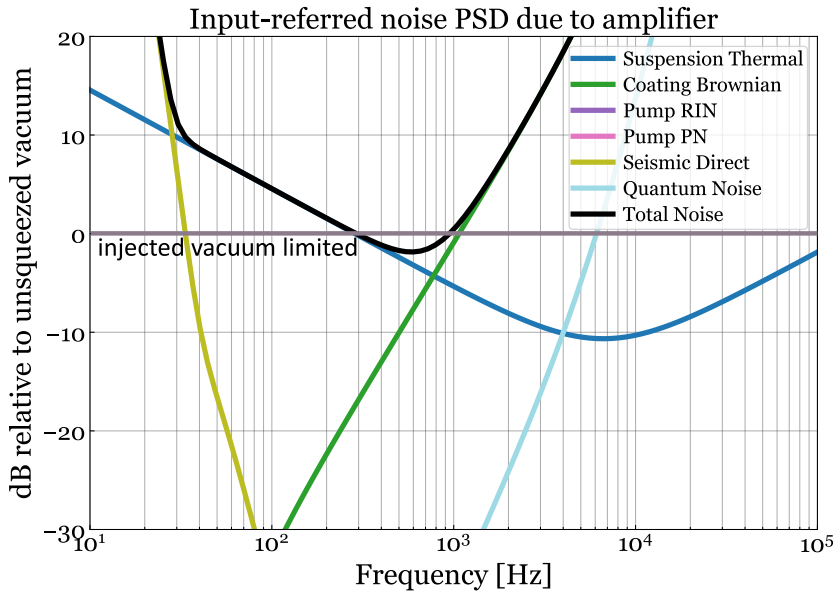

Figure 10.7: Projected noise budget of tabletop demonstration given upgrades to cryogenic PSOMA.

Future work

The successful cryogenic demonstration would allow PSOMA to directly benefit future GWIFO with high levels of readout loss limited squeezing. Future work on the tabletop could explore some of the modified optical configurations considered

in Chapter 4, or applications like mechanical feedback cooling or laser intensity stabilization.

Appendix A

CROSS-VARIANCE PHASE NOISE MEASUREMENT

Frequency noise measurement involves comparing the time elapsed on different clocks, be they lasers, cavities, atoms, or another kind of oscillator. With only two clocks, one cannot attribute observed relative frequency noise to either clock specifically. But, the pairwise comparisons among three or more clocks can be used to estimate the frequency noise contributed to the measurement by each clock independently.

A.1 Three Corner Hat

The "Three Corner Hat" (TCH) is a common approach to laser (or clock) frequency noise estimation first proposed by Gray and Allan [191]. The TCH compares the power spectral density of frequency noise on each of three beat notes between pairs of three independent lasers. If the three lasers are labelled a, b, c, and the power spectral density of frequency noise on each beat note between the ith and jth laser is X^2_{ij}, then the power spectral densities of frequency noise on the individual lasers (Y^2_k) take the form:

$$Y^2_a = \frac{X^2_{ab} + X^2_{ca} - X^2_{bc}}{2}. \tag{A.1}$$

A.2 Cross-Variance

There is a phase-coherent version of the TCH method called the cross-variance (or Allan Covariance, or Groslambert Variance). By simultaneously measuring the three beat note frequencies and computing their cross-variance, this method avoids the bias of the TCH measurement due to phase detector noise [192][193] [194].

Consider $\phi_i(t)$ the phase error (additional phase relative to the carrier frequency) on laser i of three. Then, the phase estimated for the beat note between lasers i and j is

$$\phi_{ij} = \phi_i - \phi_j + \theta_{ij} \tag{A.2}$$

where θ_{ij} is the frequency noise on our estimate of ϕ_{ij}. Instead of comparing the

auto-correlations of each beat note phase, compute the cross-correlation of each pair of beat notes.

$$\langle \phi_{ij}\phi_{kj}\rangle = \langle \phi_i\phi_m\rangle + \langle \phi_j^2\rangle - \langle \phi_i\phi_j\rangle - \langle \phi_k\phi_j\rangle + \langle \phi_i\theta_{kj}\rangle + \langle \phi_k\theta_{ij}\rangle - \langle \phi_j\theta_{ij}\rangle - \langle \phi_j\theta kj\rangle + \langle \theta_{ij}\theta_{kj}\rangle \tag{A.3}$$

Assuming the phase noise of each laser is independent of the other lasers, and the errors on each beat note estimate are independent of the laser noises and each other, most of the terms above approach 0 for sufficiently long measurement times. Thus after measurement time τ, the auto-correlation of each laser's phase approaches

$$\langle \phi_j^2\rangle_\tau \rightarrow \langle \phi_{ij}\phi_{kj}\rangle. \tag{A.4}$$

We can use the phase errors to define a corresponding frequency error at each timestep set by our sampling period.

BIBLIOGRAPHY

[1]B. C. Barish and R. Weiss, "LIGO and the detection of gravitational waves", Physics Today **52**, 44–50 (1999) 10.1063/1.882861.

[2]É. É. Flanagan and S. A. Hughes, "The basics of gravitational wave theory", New Journal of Physics **7**, 204 (2005) 10.1088/1367-2630/7/1/204, https://dx.doi.org/10.1088/1367-2630/7/1/204.

[3]B. P. Abbott et al., "Exploring the sensitivity of next generation gravitational wave detectors", Classical and Quantum Gravity **34**, 044001 (2017) 10.1088/1361-6382/aa51f4, https://dx.doi.org/10.1088/1361-6382/aa51f4.

[4]N. Aggarwal et al., "Challenges and opportunities of gravitational-wave searches at MHz to GHz frequencies", Living Reviews in Relativity **24**, 4 (2021) 10.1007/s41114-021-00032-5, https://doi.org/10.1007/s41114-021-00032-5.

[5]M. Goryachev et al., "Rare events detected with a bulk acoustic wave high frequency gravitational wave antenna", Physical Review Letters **127**, 071102 (2021) 10.1103/PhysRevLett.127.071102, https://link.aps.org/doi/10.1103/PhysRevLett.127.071102.

[6]B. Hensen et al., "Loophole-free bell inequality violation using electron spins separated by 1.3 kilometres", Nature **526**, 682–686 (2015) 10.1038/nature15759, https://doi.org/10.1038/nature15759.

[7]I. Marinkovi ć et al., "Optomechanical bell test", Physical Review Letters **121**, 220404 (2018) 10.1103/PhysRevLett.121.220404, https://link.aps.org/doi/10.1103/PhysRevLett.121.220404.

[8]Y. Chen, "Macroscopic quantum mechanics: theory and experimental concepts of optomechanics", Journal of Physics B: Atomic, Molecular and Optical Physics **46**, 104001 (2013) 10.1088/0953-4075/46/10/104001, https://dx.doi.org/10.1088/0953-4075/46/10/104001.

[9]H. Miao, *Exploring Macroscopic Quantum Mechanics in Optomechanical Devices* (2012), 10.1007/978-3-642-25640-0.

[10]V. B. Braginsky et al., "Systems with small dissipation", American Journal of Physics **55**, 1153–1154 (1987) 10.1119/1.15272.

[11]V. B. Braginskii and A. B. Manukin, *Measurement of weak forces in physics experiments* (1977).

[12]K. S. Thorne et al., "Quantum nondemolition measurements of harmonic oscillators", Physical Review Letters **40**, 667–671 (1978) 10.1103/PhysRevLett.40.667.

[13]D. Ganapathy et al. (LIGO O4 Detector Collaboration), "Broadband quantum enhancement of the LIGO detectors with frequency-dependent squeezing", Physical Review X **13**, 041021 (2023) 10.1103/PhysRevX.13.041021, https://link.aps.org/doi/10.1103/PhysRevX.13.041021.

[14]S. Zhou et al., "Achieving the Heisenberg limit in quantum metrology using quantum error correction", Nature Communications **9**, 78 (2018) 10.1038/s41467-017-02510-3, https://doi.org/10.1038/s41467-017-02510-3.

[15]R. X. Adhikari, "Gravitational radiation detection with laser interferometry", Review of Modern Physics **86**, 121–151 (2014) 10.1103/RevModPhys.86.121, https://link.aps.org/doi/10.1103/RevModPhys.86.121.

[16]S. L. Danilishin, F. Y. Khalili, and H. Miao, "Advanced quantum techniques for future gravitational-wave detectors", Living Reviews in Relativity **22**, 2, 2 (2019) 10.1007/s41114-019-0018-y, arXiv:1903.05223 [gr-qc].

[17]H. Sandberg, J.-C. Delvenne, and J. Doyle, "On lossless approximations, the fluctuation-dissipation theorem, and limitations of measurements", Automatic Control, IEEE Transactions on **56**, 293–308 (2011) 10.1109/TAC.2010.2056450.

[18]Y. Bai et al., "Phase-sensitive optomechanical amplifier for quantum noise reduction in laser interferometers", Physical Review A **102**, 023507 (2020) 10.1103/PhysRevA.102.023507, https://link.aps.org/doi/10.1103/PhysRevA.102.023507,

[19]N. D. Smith, "A technique for continuous measurement of the quality factor of mechanical oscillators", Review of Scientific Instruments **86**, 053907, 053907 (2015) 10.1063/1.4920922.

[20]T. Corbitt, Y. Chen, and N. Mavalvala, "Mathematical framework for simulation of quantum fields in complex interferometers using the two-photon formalism", Physical Review A **72**, 013818 (2005) 10.1103/PhysRevA.72.013818, https://link.aps.org/doi/10.1103/PhysRevA.72.013818.

[21]M. Aspelmeyer, T. J. Kippenberg, and F. Marquardt, "Cavity optomechanics", Review of Modern Physics **86**, 1391–1452 (2014) 10.1103/RevModPhys.86.1391, https://link.aps.org/doi/10.1103/RevModPhys.86.1391.

[22]C. M. Caves and B. L. Schumaker, "New formalism for two-photon quantum optics. I. Quadrature phases and squeezed states", Physical Review A **31**, 3068–3092 (1985) 10.1103/PhysRevA.31.3068, https://link.aps.org/doi/10.1103/PhysRevA.31.3068.

[23]B. L. Schumaker and C. M. Caves, "New formalism for two-photon quantum optics. II. Mathematical foundation and compact notation", Physical Review A **31**, 3093–3111 (1985) 10.1103/PhysRevA.31.3093, https://link.aps.org/doi/10.1103/PhysRevA.31.3093.

[24]F. A. E. Pirani, "Invariant formulation of gravitational radiation theory", Physical Review **105**, 1089–1099 (1957) 10.1103/PhysRev.105.1089, https://link.aps.org/doi/10.1103/PhysRev.105.1089.

[25]D. Sigg, *Strain calibration in LIGO*, tech. rep. T970101 (LIGO Laboratory, 2003), https://dcc.ligo.org/LIGO-T970101.

[26]J. M. Silver et al., "Nonlinear enhanced microresonator gyroscope", Optica **8**, 1219 (2021) 10.1364/OPTICA.426018, arXiv:2001.05479 [physics.optics].

[27]M. Evans, L. Barsotti, and P. Fritschel, "A general approach to optomechanical parametric instabilities", Physics Letters A **374**, 665–671 (2010) https://doi.org/10.1016/j.physleta.2009.11.023, https://www.sciencedirect.com/science/article/pii/S0375960109014558.

[28]C. Yang, L. Zhang, and W. Zhang, "Squeezed cooling of mechanical motion beyond the resolved-sideband limit", Europhysics Letters **122**, 14001 (2018) 10.1209/0295-5075/122/14001, https://dx.doi.org/10.1209/0295-5075/122/14001.

[29]T. Corbitt et al., "Squeezed-state source using radiation-pressure-induced rigidity", Physical Review A **73**, 023801 (2006) 10.1103/PhysRevA.73.023801, https://link.aps.org/doi/10.1103/PhysRevA.73.023801.

[30]J. Cripe et al., "Observation of a room-temperature oscillator's motion dominated by quantum fluctuations over a broad audio-frequency band", arXiv e-prints, arXiv:1802.10069, arXiv:1802.10069 (2018) 10.48550/arXiv.1802.10069, arXiv:1802.10069 [quant-ph].

[31]Y. Zhao et al., "Suppression of extraneous thermal noise in cavity optomechanics", in Conference on lasers and electro-optics 2012 (2012), JM1K.4, https://opg.optica.org/abstract.cfm?URI=CLEO_SI-2012-JM1K.4.

[32]Y. V. Stadnik and V. V. Flambaum, "Enhanced effects of variation of the fundamental constants in laser interferometers and application to dark-matter detection", Physical Review A **93**, 063630 (2016) 10.1103/PhysRevA.93.063630, https://link.aps.org/doi/10.1103/PhysRevA.93.063630.

[33]B. P. Abbott et al., "LIGO: The Laser Interferometer Gravitational-Wave Observatory", Reports on Progress in Physics **72**, 076901, 076901 (2009) 10.1088/0034-4885/72/7/076901, arXiv:0711.3041 [gr-qc].

[34]P. Saulson, *Fundamentals of interferometric gravitational wave detectors* (1994), https://api.semanticscholar.org/CorpusID:118208149.

[35]E. D. Hall, "Long-baseline laser interferometry for the detection of binary black-hole mergers", PhD thesis (California Institute of Technology, Division of Physics, Mathematics and Astronomy, Jan. 2017).

[36]M. Pitkin et al., "Gravitational wave detection by interferometry (ground and space)", Living Reviews in Relativity **14** (2000), https://api.semanticscholar.org/CorpusID:54515973.

[37]C. Bond et al., "Interferometer techniques for gravitational-wave detection", Living Reviews in Relativity **19**, 3 (2017) 10.1007/s41114-016-0002-8, https://doi.org/10.1007/s41114-016-0002-8.

[38]G. Cella and A. Giazotto, "Invited Review Article: Interferometric gravity wave detectors", Review of Scientific Instruments **82**, 101101 (2011) 10.1063/1.3652857, eprint: https://pubs.aip.org/aip/rsi/article-pdf/doi/10.1063/1.3652857/16055832/101101_1_online.pdf, https://doi.org/10.1063/1.3652857.

[39]D. V. Martynov et al., "Sensitivity of the Advanced LIGO detectors at the beginning of gravitational wave astronomy", Physical Review D **93**, 112004 (2016) 10.1103/PhysRevD.93.112004, https://link.aps.org/doi/10.1103/PhysRevD.93.112004.

[40]C. Whittle et al., "Unification of thermal and quantum noises in gravitational-wave detectors", Physical Review Letters **130**, 241401, 241401 (2023) 10.1103/PhysRevLett.130.241401, arXiv:2301.00338 [astro-ph.IM].

[41]Y. Levin, "Internal thermal noise in the LIGO test masses: a direct approach", Physical Review D **57**, 659–663 (1998) 10.1103/PhysRevD.57.659, https://link.aps.org/doi/10.1103/PhysRevD.57.659.

[42]G. González, "Suspensions thermal noise in the LIGO gravitational wave detector", Classical and Quantum Gravity **17**, 4409–4435 (2000) 10.1088/0264-9381/17/21/305, arXiv:gr-qc/0006053 [gr-qc].

[43]A. Buonanno and Y. Chen, "Quantum noise in second generation, signal recycled laser interferometric gravitational wave detectors", Physical Review D **64**, 042006 (2001), https://api.semanticscholar.org/CorpusID:9280888.

[44]A. Buonanno and Y. Chen, "Signal recycled laser-interferometer gravitational-wave detectors as optical springs", Physical Review D **65**, 042001 (2002) 10.1103/PhysRevD.65.042001, https://link.aps.org/doi/10.1103/PhysRevD.65.042001.

[45]S. L. Danilishin and F. Y. Khalili, "Quantum measurement theory in gravitational-wave detectors", Living Reviews in Relativity **15**, 5 (2012) 10.12942/lrr-2012-5, https://doi.org/10.12942/lrr-2012-5.

[46]A. H. Safavi-Naeini and O. Painter, "Proposal for an optomechanical traveling wave phonon-photon translator", New Journal of Physics **13**, 013017, 013017 (2011) 10.1088/1367-2630/13/1/013017, arXiv:1009.3529 [physics.optics].

[47]R. X. Adhikari et al., "A cryogenic silicon interferometer for gravitational-wave detection", Classical and Quantum Gravity **37**, 165003 (2020) 10.1088/1361-6382/ab9143, https://dx.doi.org/10.1088/1361-6382/ab9143,

[48]C. M. Caves, "Quantum-mechanical noise in an interferometer", Physical Review D **23**, 1693–1708 (1981) 10.1103/PhysRevD.23.1693, https://link.aps.org/doi/10.1103/PhysRevD.23.1693.

[49]E. Knyazev, F. Y. Khalili, and M. V. Chekhova, "Overcoming inefficient detection in sub-shot-noise absorption measurement and imaging", Optics Express **27**, 7868 (2019) 10.1364/OE.27.007868, arXiv:1810.08115 [quant-ph].

[50]E. Knyazev et al., "Quantum tomography enhanced through parametric amplification", New Journal of Physics **20**, 013005, 013005 (2018) 10.1088/1367-2630/aa99b4, arXiv:1708.03820 [quant-ph].

[51]C. M. Caves, "Quantum limits on noise in linear amplifiers", Physical Review D **26**, 1817–1839 (1982) 10.1103/PhysRevD.26.1817, https://link.aps.org/doi/10.1103/PhysRevD.26.1817.

[52]O. H. Schmitt, "High intensity X-ray monochromator", Review of Scientific Instruments **12**, 548–551 (1941) 10.1063/1.1769796.

[53]M. Takeoka et al., "Fundamental precision limit of a Mach-Zehnder interferometric sensor when one of the inputs is the vacuum", Physical Review A **96**, 052118 (2017) 10.1103/PhysRevA.96.052118, https://link.aps.org/doi/10.1103/PhysRevA.96.052118.

[54]M. Tsang and C. M. Caves, "Coherent quantum-noise cancellation for optomechanical sensors", Physical Review Letters **105**, 123601 (2010) 10.1103/PhysRevLett.105.123601, https://link.aps.org/doi/10.1103/PhysRevLett.105.123601.

[55]Y. Ma et al., "Narrowing the filter-cavity bandwidth in gravitational-wave detectors via optomechanical interaction", Physical Review Letters **113**, 151102 (2014) 10.1103/PhysRevLett.113.151102, https://link.aps.org/doi/10.1103/PhysRevLett.113.151102.

[56]H. J. Kimble et al., "Conversion of conventional gravitational-wave interferometers into quantum nondemolition interferometers by modifying their input and/or output optics", Physical Review D **65**, 022002 (2001) 10.1103/PhysRevD.65.022002, https://link.aps.org/doi/10.1103/PhysRevD.65.022002.

[57]H. Miao et al., "Enhancing the bandwidth of gravitational-wave detectors with unstable optomechanical filters", Physical Review Letters **115**, 211104 (2015) 10.1103/PhysRevLett.115.211104, https://link.aps.org/doi/10.1103/PhysRevLett.115.211104.

[58]X. Li et al., "Coherent coupling completing an unambiguous optomechanical classification framework", Physical Review A **100**, 053855 (2019) 10.1103/PhysRevA.100.053855, https://link.aps.org/doi/10.1103/PhysRevA.100.053855.

[59]X. Li et al., "Enhancing interferometer sensitivity without sacrificing bandwidth and stability: beyond single-mode and resolved-sideband approximation", Physical Review D **103**, 122001 (2021) 10.1103/PhysRevD.103.122001, https://link.aps.org/doi/10.1103/PhysRevD.103.122001.

[60]X. Li et al., *Broadband sensitivity improvement via coherent quantum feedback with PT symmetry*, 2020, arXiv:2012.00836 [quant-ph].

[61]C. Reimer et al., "Generation of multiphoton entangled quantum states by means of integrated frequency combs", Science **351**, 1176–1180 (2016) 10.1126/science.aad8532, eprint: https://www.science.org/doi/pdf/10.1126/science.aad8532, https://www.science.org/doi/abs/10.1126/science.aad8532.

[62]O. Pfister, "Continuous-variable quantum computing in the quantum optical frequency comb", Journal of Physics B: Atomic, Molecular and Optical Physics **53**, 012001 (2019) 10.1088/1361-6455/ab526f, https://dx.doi.org/10.1088/1361-6455/ab526f.

[63]Q. Zhuang, J. Preskill, and L. Jiang, "Distributed quantum sensing enhanced by continuous-variable error correction", New Journal of Physics **22**, 022001 (2020) 10.1088/1367-2630/ab7257, https://dx.doi.org/10.1088/1367-2630/ab7257.

[64]K. Noh, S. M. Girvin, and L. Jiang, "Encoding an oscillator into many oscillators", Physical Review Letters **125**, 080503 (2020) 10.1103/PhysRevLett.125.080503, https://link.aps.org/doi/10.1103/PhysRevLett.125.080503.

[65]Y. Shi, C. Chamberland, and A. Cross, "Fault-tolerant preparation of approximate GKP states", New Journal of Physics **21**, 093007 (2019) 10.1088/1367-2630/ab3a62, https://dx.doi.org/10.1088/1367-2630/ab3a62.

[66]Y. Cai et al., "Multimode entanglement in reconfigurable graph states using optical frequency combs", Nature Communications **8**, 15645 (2017) 10.1038/ncomms15645, https://doi.org/10.1038/ncomms15645.

[67]M. Pysher et al., "Parallel generation of quadripartite cluster entanglement in the optical frequency comb", Physical Review Letters **107**, 030505 (2011) 10.1103/PhysRevLett.107.030505, https://link.aps.org/doi/10.1103/PhysRevLett.107.030505.

[68]P. Campagne-Ibarcq et al., "Quantum error correction of a qubit encoded in grid states of an oscillator", Nature **584**, 368–372 (2020) 10.1038/s41586-020-2603-3, https://doi.org/10.1038/s41586-020-2603-3.

[69]K. Duivenvoorden, B. M. Terhal, and D. Weigand, "Single-mode displacement sensor", Physical Review A **95**, 012305 (2017) 10.1103/PhysRevA.95.012305, https://link.aps.org/doi/10.1103/PhysRevA.95.012305.

[70]M. Brunelli et al., "Stroboscopic quantum optomechanics", Physical Review Research **2**, 023241 (2020) 10.1103/PhysRevResearch.2.023241, https://link.aps.org/doi/10.1103/PhysRevResearch.2.023241.

[71]C. Weedbrook et al., "Gaussian quantum information", Rev. Mod. Phys. **84**, 621–669 (2012) 10.1103/RevModPhys.84.621, https://link.aps.org/doi/10.1103/RevModPhys.84.621.

[72]Y. Chen, "Sagnac interferometer as a speed-meter-type, quantum-nondemolition gravitational-wave detector", Physical Review D **67**, 122004, 122004 (2003) 10.1103/PhysRevD.67.122004, arXiv:gr-qc/0208051 [gr-qc].

[73]F. Y. Khalili, "A new double-pass type of the optical spring", (2024), https://dcc.ligo.org/LIGO-P2400002.

[74]H. Miao et al., "Towards the fundamental quantum limit of linear measurements of classical signals", Physical Review Letters **119**, 050801 (2017) 10.1103/PhysRevLett.119.050801, https://link.aps.org/doi/10.1103/PhysRevLett.119.050801.

[75]M. Korobko et al., "Quantum expander for gravitational-wave observatories", Light: Science & Applications **8**, 118, 118 (2019) 10.1038/s41377-019-0230-2, arXiv:1903.05930 [quant-ph].

[76]Y. Ma et al., *Application of optomechanical frequency conversion on gravitational wave detection*, 2019, arXiv:1912.01246 [quant-ph].

[77]M. A. Page et al., "Gravitational wave detectors with broadband high frequency sensitivity", Communications Physics **4**, 27, 27 (2021) 10.1038/s42005-021-00526-2, arXiv:2007.08766 [physics.optics].

[78]J. Smetana et al., "Design of a tabletop interferometer with quantum amplification", Physical Review A **107**, 043701 (2023) 10.1103/PhysRevA.107.043701, https://link.aps.org/doi/10.1103/PhysRevA.107.043701.

[79]F. Roccati et al., "Quantum correlations in PT-symmetric systems", Quantum Science & Technology **6** (2020), https://api.semanticscholar.org/CorpusID:211548204.

[80]C. M. Bender, "Introduction to PT-symmetric quantum theory", Contemporary Physics **46**, 277–292 (2005) 10.1080/00107500072632, eprint: https://doi.org/10.1080/00107500072632, https://doi.org/10.1080/00107500072632.

[81]B. Sütlüoğlu and C. Bulutay, "Static synthetic gauge field control of double optomechanically induced transparency in a closed-contour interaction scheme", Physical Review A **104**, 033504, 033504 (2021) 10.1103/PhysRevA.104.033504, arXiv:2104.04014 [quant-ph].

[82]X.-W. Luo, C. Zhang, and S. Du, "Quantum squeezing and sensing with pseudo-anti-parity-time symmetry", Physical Review Letters **128**, 173602 (2022) 10.1103/PhysRevLett.128.173602, https://link.aps.org/doi/10.1103/PhysRevLett.128.173602.

[83]Y. Ma et al., "Proposal for gravitational-wave detection beyond the standard quantum limit through EPR entanglement", Nature Physics **13**, 776–780 (2017) 10.1038/nphys4118, arXiv:1612.06934 [quant-ph].

[84]H.-K. Lau and A. A. Clerk, "Fundamental limits and non-reciprocal approaches in non-Hermitian quantum sensing", Nature Communications **9**, 4320 (2018) 10.1038/s41467-018-06477-7, https://doi.org/10.1038/s41467-018-06477-7.

[85]L. Bao et al., "Fundamental limits for reciprocal and nonreciprocal non-Hermitian quantum sensing", Physical Review A **103**, 042418 (2021) 10.1103/PhysRevA.103.042418, https://link.aps.org/doi/10.1103/PhysRevA.103.042418.

[86]F. Lecocq et al., "Efficient qubit measurement with a nonreciprocal microwave amplifier", Physical Review Letters **126**, 020502 (2021) 10.1103/PhysRevLett.126.020502, https://link.aps.org/doi/10.1103/PhysRevLett.126.020502.

[87]T. Li, Z. Gao, and K. Xia, "Nonlinear-dissipation-induced nonreciprocal exceptional points", Optics Express **29**, 17613 (2021) 10.1364/OE.426474.

[88]M. J. Grant and M. J. F. Digonnet, "Rotation sensitivity and shot-noise-limited detection in an exceptional-point coupled-ring gyroscope", Optics Letters **46**, 2936 (2021) 10.1364/OL.423700.

[89]A. Metelmann and A. A. Clerk, "Nonreciprocal photon transmission and amplification via reservoir engineering", Physical Review X **5**, 021025, 021025 (2015) 10.1103/PhysRevX.5.021025, arXiv:1502.07274 [quant-ph].

[90]C. M. Caves, "Reframing SU(1,1) interferometry", Advanced Quantum Technologies **3** (2019), https://api.semanticscholar.org/CorpusID:209515962.

[91]M. Liu, L. Zhang, and H. Miao, "Adaptive protocols for SU(1,1) interferometers to achieve ab initio phase estimation at the Heisenberg limit", New Journal of Physics **25**, 103051, 103051 (2023) 10.1088/1367-2630/ad042f, arXiv:2307.14606 [quant-ph].

[92]A. Dmitriev, H. Miao, and D. Martynov, "Enhancing the sensitivity of interferometers with stable phase-insensitive quantum filters", Physical Review D **106**, 022007, 022007 (2022) 10.1103/PhysRevD.106.022007, arXiv:2110.15354 [quant-ph].

[93]S. Otabe et al., "Kerr-enhanced optical spring", arXiv e-prints, arXiv:2310.18828, arXiv:2310.18828 (2023) 10.48550/arXiv.2310.18828, arXiv:2310.18828 [quant-ph].

[94]T. Zhang et al., "Gravitational-wave detector for postmerger neutron stars: beyond the quantum loss limit of the Fabry-Perot-Michelson interferometer", Physical Review X **13**, 021019 (2023) 10.1103/PhysRevX.13.021019, https://link.aps.org/doi/10.1103/PhysRevX.13.021019.

[95]X. Guo et al., "Sensing and control scheme for the inteferometer configuration with an L-shaped resonator", Classical and Quantum Gravity **40**, 235005, 235005 (2023) 10.1088/1361-6382/ad0454, arXiv:2306.00039 [astro-ph.IM].

[96]S. Sato et al., "Demonstration of displacement- and frequency-noise-free laser interferometry using bidirectional Mach-Zehnder interferometers", Physical Review Letters **98**, 141101 (2007) 10.1103/PhysRevLett.98.141101, https://link.aps.org/doi/10.1103/PhysRevLett.98.141101.

[97]S. Kawamura and Y. Chen, "Displacement-noise-free gravitational-wave detection", Physical Review Letters **93**, 211103, 211103 (2004) 10.1103/PhysRevLett.93.211103, arXiv:gr-qc/0405093 [gr-qc].

[98]W. Kern, "The evolution of silicon wafer cleaning technology", Journal of The Electrochemical Society **137**, 1887 (1990) 10.1149/1.2086825, https://dx.doi.org/10.1149/1.2086825.

[99]W. Z. Korth, "Mitigating noise in interferometric gravitational wave detectors", PhD thesis (California Institute of Technology, 2019), 10.7907/4H7V-W213, https://resolver.caltech.edu/CaltechTHESIS:05292019-020613259.

[100]S. Chao et al., "Progress of coating development at NTHU", Technical Report G1200849-v1 (2012), https://dcc.ligo.org/LIGO-G1200849/public.

[101]E. D. Palik et al., "Etching roughness for (100) silicon surfaces in aqueous KOH", Journal of Applied Physics **70**, 3291–3300 (1991) 10.1063/1.349263.

[102]K. Numata, A. Kemery, and J. Camp, "Thermal-noise limit in the frequency stabilization of lasers with rigid cavities", Physical Review Letters **93**, 250602 (2004) 10.1103/PhysRevLett.93.250602, https://link.aps.org/doi/10.1103/PhysRevLett.93.250602.

[103]N. M. Ravindra et al., "Emissivity measurements and modeling of silicon-related materials: an overview", International Journal of Thermophysics **22**, 1593–1611 (2001) 10.1023/A:1012869710173, https://doi.org/10.1023/A:1012869710173.

[104]M. Constancio Jr. et al., "Silicon emissivity as a function of temperature", International Journal of Heat and Mass Transfer **157**, 119863 (2020) 10.1016/j.ijheatmasstransfer.2020.119863, https://www.sciencedirect.com/science/article/pii/S0017931019361289,

[105]H. C. Jacks, "Identifying structures responsible for two-level systems in amorphous silicon", PhD thesis (University of California, Berkeley, Jan. 2018).

[106]S. Yoon et al., "Comparison of residual stress and optical properties in Ta2O5 thin films deposited by single and dual ion beam sputtering", Materials Science and Engineering: B **118**, EMRS 2004, Symposium D: Functional Oxides for Advanced Semiconductor Technologies, 234–237 (2005) https://doi.org/10.1016/j.mseb.2004.12.055, https://www.sciencedirect.com/science/article/pii/S0921510704006816.

[107]T. Okada et al., "Analysis of transient temperature profile during thermal plasma jet annealing of Si films on quartz substrate", Japanese Journal of Applied Physics **45**, 4355 (2006) 10.1143/JJAP.45.4355, https://dx.doi.org/10.1143/JJAP.45.4355.

[108]R. Nawrodt et al., "Investigation of mechanical losses of thin silicon flexures at low temperatures", Classical and Quantum Gravity **30**, 115008 (2013) 10.1088/0264-9381/30/11/115008, https://dx.doi.org/10.1088/0264-9381/30/11/115008.

[109]E. Cesarini et al., "A gentle nodal suspension for measurements of the acoustic attenuation in materials", in 2014 ieee metrology for aerospace (metroaerospace) (2014), pp. 528–532, 10.1109/MetroAeroSpace.2014.6865982.

[110]N. A. Didio, "AlGaAs coating studies for present and future gravitational wave detectors", PhD thesis (2023), https://surface.syr.edu/etd/1710.

[111]I. Martin et al., "Measurements of a low-temperature mechanical dissipation peak in a single layer of Ta2O5 doped with TiO2", Classical and Quantum Gravity **25**, 055005 (2008) 10.1088/0264-9381/25/5/055005, https://dx.doi.org/10.1088/0264-9381/25/5/055005.

[112]K. Haughian et al., "Mechanical loss of a hydroxide catalysis bond between sapphire substrates and its effect on the sensitivity of future gravitational wave detectors", Physical Review D **94**, 082003 (2016) 10.1103/PhysRevD.94.082003, https://link.aps.org/doi/10.1103/PhysRevD.94.082003.

[113]S. D. Penn et al., "Mechanical ringdown studies of large-area substrate-transferred GaAs/AlGaAs crystalline coatings", J. Opt. Soc. Am. B **36**, C15–C21 (2019) 10.1364/JOSAB.36.000C15, https://opg.optica.org/josab/abstract.cfm?URI=josab-36-4-C15.

[114]G. Hofmann et al., "Indium joints for cryogenic gravitational wave detectors", Classical and Quantum Gravity **32**, 245013 (2015) 10.1088/0264-9381/32/24/245013, https://dx.doi.org/10.1088/0264-9381/32/24/245013.

[115]M. R. Abernathy et al., "Measurement of mechanical loss in the Acktar Black coating of silicon wafers", Classical and Quantum Gravity **33**, 185002 (2016) 10.1088/0264-9381/33/18/185002, https://dx.doi.org/10.1088/0264-9381/33/18/185002.

[116]M. Granata et al., "Internal friction and Young's modulus measurements on SiO2 and Ta2O5 films done with an ultra-high Q silicon-wafer suspension", Archives of Metallurgy and Materials **60**, 10.1515/amm-2015-0060 (2015) 10.1515/amm-2015-0060.

[117]X. Liu et al., "Internal friction of amorphous and nanocrystalline silicon at low temperatures", Materials Science and Engineering: A **442**, Proceedings of the 14th International Conference on Internal Friction and Mechanical Spectroscopy, 307–313 (2006) https://doi.org/10.1016/j.msea.2006.01.146, https://www.sciencedirect.com/science/article/pii/S0921509306011518.

[118]L. G. Prokhorov et al., "Measurement of mechanical losses in the carbon nanotube black coating of silicon wafers", Classical and Quantum Gravity **37**, 015004 (2019) 10.1088/1361-6382/ab5357, https://dx.doi.org/10.1088/1361-6382/ab5357,

[119]E. M. Gretarsson et al., "Measured limits on amplitude dependence of mechanical loss in substrate-transferred GaAs/$Al_{0.92}Ga_{0.08}As$ coatings", Physical Review D **106**, 042001 (2022) 10.1103/PhysRevD.106.042001, https://link.aps.org/doi/10.1103/PhysRevD.106.042001.

[120]A. Dari et al., "Breaking strength tests on silicon and sapphire bondings for gravitational wave detectors", Classical and Quantum Gravity **27**, 045010 (2010) 10.1088/0264-9381/27/4/045010, https://dx.doi.org/10.1088/0264-9381/27/4/045010.

[121]A. M. Preston et al., "Stable materials and bonding techniques for space-based optical systems", (2007), https://api.semanticscholar.org/CorpusID:23147534.

[122]N. L. Beveridge et al., "Dependence of cryogenic strength of hydroxide catalysis bonded silicon on type of surface oxide", Classical and Quantum Gravity **30**, 025003 (2012) 10.1088/0264-9381/30/2/025003, https://dx.doi.org/10.1088/0264-9381/30/2/025003.

[123]M. Lorenzini et al., "Silicate bonding properties: Investigation through thermal conductivity measurements", in Journal of physics conference series, Vol. 228, Journal of Physics Conference Series (May 2010), p. 012019, 10.1088/1742-6596/228/1/012019.

[124]K. Haughian et al., "The effect of crystal orientation on the cryogenic strength of hydroxide catalysis bonded sapphire", Class. Quant. Grav. **32**, 075013 (2015) 10.1088/0264-9381/32/7/075013.

[125]J. Neyman, "Outline of a theory of statistical estimation based on the classical theory of probability", Philosophical Transactions of the Royal Society of London Series A **236**, 333–380 (1937) 10.1098/rsta.1937.0005.

[126]G. J. Feldman and R. D. Cousins, "Unified approach to the classical statistical analysis of small signals", Physical Review D **57**, 3873–3889 (1998) 10.1103/PhysRevD.57.3873, https://link.aps.org/doi/10.1103/PhysRevD.57.3873.

[127]T. Ohta et al., "Simultaneous measurement of substrate temperature and thin-film thickness on SiO_2/Si wafer using optical-fiber-type low-coherence interferometry", Journal of Applied Physics **105**, 013110-013110-7, 013110-013110–7 (2009) 10.1063/1.3058592.

[128]S. Dakshinamurthy, N. R. Quick, and A. Kar, "Temperature-dependent optical properties of silicon carbide for wireless temperature sensors", Journal of Physics D: Applied Physics **40**, 353 (2007) 10.1088/0022-3727/40/2/010, https://dx.doi.org/10.1088/0022-3727/40/2/010.

[129]C. Koshimizu et al., "Low-coherence interferometry-based non-contact temperature monitoring of a silicon wafer and chamber parts during plasma etching", Applied Physics Express **3**, 056201 (2010) 10.1143/APEX.3.056201, https://dx.doi.org/10.1143/APEX.3.056201.

[130]K. Takeda et al., "Temperature-measurement system using optical fiber-type low-coherence interferometry for multilayered substrate", Japanese Journal of Applied Physics **43**, 7737 (2004) 10.1143/JJAP.43.7737, https://dx.doi.org/10.1143/JJAP.43.7737.

[131]P. Lautenschlager et al., "Temperature dependence of the dielectric function and interband critical points in silicon", Physical Review B **36**, 4821–4830 (1987) 10.1103/PhysRevB.36.4821, https://link.aps.org/doi/10.1103/PhysRevB.36.4821.

[132]M. A. Hopcroft, W. D. Nix, and T. W. Kenny, "What is the Young's modulus of silicon?", Journal of Microelectromechanical Systems **19**, 229–238 (2010) 10.1109/JMEMS.2009.2039697.

[133]C.-H. Cho, "Characterization of Young's modulus of silicon versus temperature using a "beam deflection" method with a four-point bending fixture", Current Applied Physics **9**, 538–545 (2009) https://doi.org/10.1016/j.cap.2008.03.024, https://www.sciencedirect.com/science/article/pii/S1567173908000850.

[134]U. Gysin et al., "Temperature dependence of the force sensitivity of silicon cantilevers", Physical Review B **69**, 045403 (2004) 10.1103/PhysRevB.69.045403, https://link.aps.org/doi/10.1103/PhysRevB.69.045403.

[135]J. Beichler et al., "Capacitance studies on amorphous silicon Schottky barrier diodes", Journal of Non-Crystalline Solids **35-36**, 587–592 (1980) https://doi.org/10.1016/0022-3093(80)90658-4,https://www.sciencedirect.com/science/article/pii/0022309380906584.

[136]R. Nawrodt et al., "A new apparatus for mechanical Q-factor measurements between 5 and 300 K", Cryogenics **46**, 718–723 (2006) https://doi.org/10.1016/j.cryogenics.2006.06.001, https://www.sciencedirect.com/science/article/pii/S0011227506000993.

[137]G. K. White, *Experimental techniques in low-temperature physics* (1968), https://api.semanticscholar.org/CorpusID:138986484.

[138]J. P. Zendri et al., "Loss budget of a setup for measuring mechanical dissipations of silicon wafers between 300 and 4 K", The Review of Scientific Instruments **79 3**, 033901 (2008), https://api.semanticscholar.org/CorpusID:12453413.

[139]G. Sahasrabudhe and S. Lambade, "Temperature dependence of the collective phonon relaxation time and acoustic damping in Ge and Si", Journal of Physics and Chemistry of Solids **60**, 773–785 (1999) https://doi.org/10.1016/S0022-3697(98)00343-6, https://www.sciencedirect.com/science/article/pii/S0022369798003436.

[140]M. Abe, C. Wipf, and A. Markowitz, *Mechanical metamaterial applications for LIGO mirror noise evasion*, tech. rep. T1900386 (LIGO Laboratory, 2019), https://dcc.ligo.org/LIGO-T1900386.

[141]G. Vajente et al., "Method for the experimental measurement of bulk and shear loss angles in amorphous thin films", Physical Review D **101**, 042004, 042004 (2020) 10.1103/PhysRevD.101.042004, arXiv:1911.12277 [cond-mat.mtrl-sci].

[142]M. Abernathy et al., "Bulk and shear mechanical loss of titania-doped tantala", Physics Letters A **382**, 2282–2288 (2018) 10.1016/j.physleta.2017.08.007.

[143]D. W. Hogg, J. Bovy, and D. Lang, "Data analysis recipes: Fitting a model to data", arXiv e-prints, arXiv:1008.4686, arXiv:1008.4686 (2010) 10.48550/arXiv.1008.4686, arXiv:1008.4686 [astro-ph.IM].

[144]P. Gregory, *Bayesian logical data analysis for the physical sciences: a comparative approach with Mathematica® support* (Cambridge University Press, 2005), 10.1017/CBO9780511791277.

[145]D. S. Kim et al., "Nuclear quantum effect with pure anharmonicity and the anomalous thermal expansion of silicon", Proceedings of the National Academy of Sciences **115**, 1992–1997 (2018) 10.1073/pnas.1707745115, https://doi.org/10.1073%2Fpnas.1707745115.

[146]R. G. Christian, "The theory of oscillating-vane vacuum gauges", Vacuum **16**, 175–178 (1966) 10.1016/0042-207X(66)91162-6.

[147]Y. Tanaka et al., "Heat transfer characteristics under cryogenic, low pressure environments", Physica C: Superconductivity **469**, Proceedings of the 21st International Symposium on Superconductivity (ISS 2008), 1862–1865 (2009)

https://doi.org/10.1016/j.physc.2009.05.127, https://www.sciencedirect.com/science/article/pii/S0921453409004158.

[148]M. Saidi and R. Hosseini, "Air pressure dependence of natural-convection heat transfer", Lecture Notes in Engineering and Computer Science **2** (2010).

[149]M. Bao et al., "Energy transfer model for squeeze-film air damping in low vacuum", Journal of Micromechanics and Microengineering **12**, 341–346 (2002).

[150]Y.-H. Cho et al., "Slide film damping in laterally driven microstructures", Sensors and Actuators A: Physical **40**, 31–39 (1994) https://doi.org/10.1016/0924-4247(94)85027-5, https://www.sciencedirect.com/science/article/pii/0924424794850275.

[151]J. Atalaya et al., "Nonlinear damping and dephasing in nanomechanical systems", Physical Review B **94**, 195440, 195440 (2016) 10.1103/PhysRevB.94.195440, arXiv:1609.08714 [cond-mat.mes-hall].

[152]S. S. Iyer and R. N. Candler, "Mode- and direction-dependent mechanical energy dissipation in single-crystal resonators due to anharmonic phonon-phonon scattering", Physical Review Applied **5**, 034002, 034002 (2016) 10.1103/PhysRevApplied.5.034002.

[153]A. Bachtold, J. Moser, and M. I. Dykman, "Mesoscopic physics of nanomechanical systems", Reviews of Modern Physics **94**, 045005, 045005 (2022) 10.1103/RevModPhys.94.045005, arXiv:2202.01819 [cond-mat.mes-hall].

[154]W. P. Mason, "Ultrasonic-wave propagation in pure silicon and germanium", Acoustical Society of America Journal **36**, 644 (1964) 10.1121/1.1919031.

[155]J. Rodriguez et al., "Direct detection of Akhiezer damping in a silicon MEMS resonator", Scientific Reports **9**, 2244 (2019) 10.1038/s41598-019-38847-6, https://doi.org/10.1038/s41598-019-38847-6.

[156]G. Vajente, *Notes on measuring coatings with a nodal suspension*, tech. rep. T1900276 (LIGO Laboratory, 2019), https://dcc.ligo.org/LIGO-T1900276.

[157]G. Vajente, *Pycrime*, https://git.ligo.org/gabriele-vajente/pycrime.

[158]G. Cagnoli, *Coating research and development at LMA*, tech. rep. G1601850 (2016), https://dcc.ligo.org/LIGO-G1601850.

[159]L. Stolpner et al., "Low noise planar external cavity laser for interferometric fiber optic sensors", in 19th international conference on optical fibre sensors, Vol. 7004, edited by D. Sampson et al., Society of Photo-Optical Instrumentation Engineers (SPIE) Conference Series (Apr. 2008), p. 700457, 10.1117/12.786226.

[160]*Modulator MPX and MPZ series*, Rev. 01_2023_ED, exail (2023), https://www.ixblue.com/wp-content/uploads/2022/01/MPX+MPZ%20SERIES_4.pdf.

[161]F. Du-Burck et al., "Effects of polarization modulation induced by electro-optic modulators in fiber-based setups", IEEE Photonics Technology Letters **34**, 185–188 (2022) 10.1109/LPT.2022.3142944, arXiv:2201.07470 [physics.ins-det].

[162]P. Grüning et al., "All-fiber ring-cavity for frequency stability transfer at 1.55 μm", Applied Optics **58**, 1502–1507 (2019) 10.1364/AO.58.001502, https://opg.optica.org/ao/abstract.cfm?URI=ao-58-6-1502.

[163]Z. Li et al., "Investigation and cancellation of residual amplitude modulation in fiber electro-optic modulator based frequency modulation gas sensing technique", Sensors and Actuators B: Chemical **196**, 23–30 (2014) https://doi.org/10.1016/j.snb.2014.01.111, https://www.sciencedirect.com/science/article/pii/S0925400514001361.

[164]Z. Li et al., "Investigation and cancellation of residual amplitude modulation in fiber electro-optic modulator based frequency modulation gas sensing technique", Sensors and Actuators B: Chemical **196**, 23–30 (2014) https://doi.org/10.1016/j.snb.2014.01.111, https://www.sciencedirect.com/science/article/pii/S0925400514001361.

[165]G. Mueller et al., "Determination and optimization of mode matching into optical cavities by heterodyne detection", Opt. Lett. **25**, 266–268 (2000) 10.1364/OL.25.000266, https://opg.optica.org/ol/abstract.cfm?URI=ol-25-4-266.

[166]R. Abbott, *High stability low noise laser current driver PCB*, tech. rep. D1200719 (LIGO Laboratory, 2016), https://dcc.ligo.org/LIGO-D1200719-v6.

[167]A. Staley, "Locking the advanced LIGO gravitational wave detector: with a focus on the arm length stabilization technique", PhD thesis (Columbia University, New York, Nov. 2015).

[168]E. D. Black, "An introduction to Pound-Drever-Hall laser frequency stabilization", American Journal of Physics **69**, 79–87 (2001) 10.1119/1.1286663.

[169]A. Gupta, *Using PLL for Frequency Noise Measurement*, tech. rep. T1900263 (LIGO Laboratory, 2019), https://dcc.ligo.org/LIGO-T1900263.

[170]S. Kobayashi et al., "Direct frequency modulation in AlGaAs semiconductor lasers", IEEE Transactions on Microwave Theory and Techniques **30**, 428–441 (1982) 10.1109/TMTT.1982.1131084.

[171]F. Marquardt, J. G. E. Harris, and S. M. Girvin, "Dynamical multistability induced by radiation pressure in high-finesse micromechanical optical cavities", Physical Review Letters **96**, 103901 (2006) 10.1103/PhysRevLett.96.103901, https://link.aps.org/doi/10.1103/PhysRevLett.96.103901.

[172]M. Tse et al., "Quantum-enhanced Advanced LIGO detectors in the era of gravitational-wave astronomy", Physical Review Letters **123**, 231107 (2019) 10.1103/PhysRevLett.123.231107, https://link.aps.org/doi/10.1103/PhysRevLett.123.231107.

[173]E. Oelker et al., "Ultra-low phase noise squeezed vacuum source for gravitational wave detectors", Optica **3**, 682–685 (2016) 10.1364/OPTICA.3.000682, https://opg.optica.org/optica/abstract.cfm?URI=optica-3-7-682.

[174]S. Chelkowski et al., "Coherent control of broadband vacuum squeezing", Physical Review A **75**, 043814 (2007) 10.1103/PhysRevA.75.043814, https://link.aps.org/doi/10.1103/PhysRevA.75.043814.

[175]H. Vahlbruch et al., "Coherent control of vacuum squeezing in the gravitational-wave detection band", Physical Review Letters **97**, 011101 (2006) 10.1103/PhysRevLett.97.011101, https://link.aps.org/doi/10.1103/PhysRevLett.97.011101.

[176]L. McCuller et al., "Frequency-dependent squeezing for Advanced LIGO", Physical Review Letters **124**, 171102 (2020) 10.1103/PhysRevLett.124.171102, https://link.aps.org/doi/10.1103/PhysRevLett.124.171102.

[177]R. Pintelon and J. Schoukens, *System identification: a frequency domain approach* (2012), https://api.semanticscholar.org/CorpusID:58784535.

[178]H. B. Callen and T. A. Welton, "Irreversibility and generalized noise", Physical Review **83**, 34–40 (1951) 10.1103/PhysRev.83.34, https://link.aps.org/doi/10.1103/PhysRev.83.34.

[179]G. M. Harry et al., "Thermal noise in interferometric gravitational wave detectors due to dielectric optical coatings", Classical and Quantum Gravity **19**, 897–917 (2002) 10.1088/0264-9381/19/5/305, arXiv:gr-qc/0109073 [gr-qc].

[180]K. Numata and J. B. Camp, *Fundamental limit of 1/f frequency noise in semiconductor lasers due to mechanical thermal noise*, 2011, https://api.semanticscholar.org/CorpusID:53003541.

[181]K. Kikuchi, "Effect of 1/f-type FM noise on semiconductor-laser linewidth residual in high-power limit", IEEE Journal of Quantum Electronics **25**, 684–688 (1989) 10.1109/3.17331.

[182]C. Henry, "Phase noise in semiconductor lasers", Journal of Lightwave Technology **4**, 298–311 (1986) 10.1109/JLT.1986.1074721.

[183]C. Henry, "Theory of the linewidth of semiconductor lasers", IEEE Journal of Quantum Electronics **18**, 259–264 (1982) 10.1109/JQE.1982.1071522.

[184]A. Dandridge and H. Taylor, "Correlation of low-frequency intensity and frequency fluctuations in GaAlAs lasers", IEEE Journal of Quantum Electronics **18**, 1738–1750 (1982) 10.1109/JQE.1982.1071436.

[185]H. Loh et al., "Influence of grating parameters on the linewidths of external-cavity diode lasers", Applied Optics **45**, 9191–9197 (2006) 10.1364/AO.45.009191, https://opg.optica.org/ao/abstract.cfm?URI=ao-45-36-9191.

[186]G. Agrawal and N. Dutta, *Semiconductor lasers* (Springer US, 2013), https://books.google.com/books?id=bInTBwAAQBAJ.

[187]X. Baillard et al., "Interference-filter-stabilized external-cavity diode lasers", Optics Communications **266**, 609–613 (2006) https://doi.org/10.1016/j.optcom.2006.05.011, https://www.sciencedirect.com/science/article/pii/S0030401806004561.

[188]M. Fukuda et al., "1/f noise behavior in semiconductor laser degradation", IEEE Photonics Technology Letters **5**, 1165–1167 (1993) 10.1109/68.248415.

[189]L. Turner et al., "Frequency noise characterisation of narrow linewidth diode lasers", Optics Communications **201**, 391–397 (2002) https://doi.org/10.1016/S0030-4018(01)01689-3, https://www.sciencedirect.com/science/article/pii/S0030401801016893.

[190]L. Mercer, "1/f frequency noise effects on self-heterodyne linewidth measurements", Journal of Lightwave Technology **9**, 485–493 (1991) 10.1109/50.76663.

[191]J. Gray and D. Allan, "A method for estimating the frequency stability of an individual oscillator", in 28th annual symposium on frequency control (1974), pp. 243–246, 10.1109/FREQ.1974.200027.

[192]F. Vernotte, C. E. Calosso, and E. Rubiola, "Three-cornered hat versus Allan covariance", in 2016 ieee international frequency control symposium (ifcs) (2016), pp. 1–6, 10.1109/FCS.2016.7546784.

[193]F. Vernotte and É. Lantz, "Three-cornered hat and Groslambert covariance: a first attempt to assess the uncertainty domains", IEEE Transactions on Ultrasonics, Ferroelectrics, and Frequency Control **66**, 643–653 (2019) 10.1109/TUFFC.2018.2889703.

[194]F. Vernotte and É. Lantz, "Confidence intervals for three-cornered hat and Groslambert covariance estimates", in 2019 joint conference of the ieee international frequency control symposium and european frequency and time forum (eftf/ifc) (2019), pp. 1–3, 10.1109/FCS.2019.8856025.